EXPLORING THE ROLE OF SURFACE-ADSORBING MEDIA IN CUTTING OF CORROSION-RESISTANT METALS

by

Jason M. Davis

A Dissertation

Submitted to the Faculty of Purdue University

In Partial Fulfillment of the Requirements for the degree of

Doctor of Philosophy

School of Industrial Engineering

West Lafayette, Indiana

August 2020

THE PURDUE UNIVERSITY GRADUATE SCHOOL
STATEMENT OF COMMITTEE APPROVAL

Dr. Srinivasan Chandrasekar, Chair

School of Industrial Engineering

Dr. Ramses Martinez

School of Industrial Engineering

Dr. Kevin P. Trumble

School of Materials Engineering

Dr. Mark D. Thoreson

Naval Surface Warfare Center, Crane Division

Approved by:

Dr. Abhijit Deshmukh

I dedicate this dissertation to my loving wife Helen and our sons, Jasper and Jack. With a special feeling of gratitude, I also dedicate this work to my parents, Tommy and Reva Davis, who have always steadfastly supported me in all my pursuits.

ACKNOWLEDGMENTS

I would like to express my deep and sincere gratitude for my committee chair, Professor Srinivasan Chandrasekar for his expertise, guidance, and patience throughout the writing of this dissertation. I would also like to thank my advisory committee members, Professor Kevin Trumble, Professor Ramses Martinez, and Dr. Mark Thoreson, for their advice and support. My appreciation also extends to all my present and former laboratory colleagues in the Center for Materials Processing and Tribology, including Mojib Saei, Debapriya Pinaki Mohanty, Dr. Anirudh Udupa, Dr. Koushik Viswanathan, and Dr. James Mann, for their collaboration and discussions.

Lastly, I would like to express my appreciation to Naval Surface Warfare Center, Crane Division for its dedication to developing its workforce and affording me the tremendous opportunity to pursue a doctoral degree. I am particularly thankful for Mr. David Long and LCDR Michael Lemmons for their support and advocacy. In addition, I am grateful for the financial support of the Naval Innovative Science and Engineering (NISE) program and the Science, Mathematics, and Research for Transformation (SMART) Scholarship-for-Service Program. Without their assistance, this would not have been possible.

TABLE OF CONTENTS

LIST OF TABLES

LIST OF FIGURES

ABSTRACT

Tantalum, niobium, stainless steels, and nickel are corrosion-resistant metals that have become critical in many industrial sectors. Due to the demanding environments and temperatures in which they operate, few materials can serve as substitutes. The advantages of these materials are offset by the difficulties in their machining. Belonging to a group of metals and alloys often referred to as 'gummy', their poor machinability or gumminess is manifest as thick chip formation, large cutting forces, and poor finish on cut surface. Hence, machining costs can be prohibitive, and applications limited. The gumminess has been attributed broadly to their high strain-hardening capacity.

To examine why these metals are difficult to machine, we used direct *in situ* observations of the cutting process with a high-speed imaging system, complemented by force measurements. The observations showed that chip formation occurred by repeated large-amplitude folding of the material – sinuous flow – with vortex-like components and extensive redundant deformation. The folding was particularly severe in Ta and Nb. Although Ta and Nb displayed a higher rate of fold nucleation than the Ni and stainless steel, the flow dynamics underlying chip formation across the metals was the same – sinuous flow nucleated by a plastic (buckling-type) flow instability on the workpiece surface just ahead of the advancing tool. The large strains and energy dissipation associated with sinuous flow is the reason for the poor machinability of these metals.

Prior work with Cu and Al has shown that sinuous flow can be disrupted and replaced by an energetically more favorable (segmented) flow mode, characterized by quasi-periodic fracture, when suitable chemical media are applied to the initial workpiece surface – a mechanochemical effect. The segmented flow is beneficial for machining processes since it involves much smaller forces and plastic strains. It has been hypothesized that the chemical media influence the flow through their adsorption onto the workpiece surface, thereby altering the surface energy and/or surface stress, and effecting a local embrittlement (ductile-to-brittle transition).

We demonstrate similar media (mechanochemical) effects and segmented flow development in cutting of the corrosion-resistant metals, with significant benefits for their machining. These benefits include > 35 percent reduction in the cutting force/energy, and an order of magnitude improvement in cut surface quality (finish, tears and residual strain). Importantly, the experiments with the corrosion-resistant metals provide strong evidence that it is indeed

adsorption – not corrosion, as in case of hydrogen embrittlement – that underpins the mechanochemical effect. The experiments used chemical agents well-known for their strong adsorption to metal surfaces, namely green corrosion inhibitors (e.g., plant extracts, propolis) and other natural organic molecules (e.g., dyes, antibacterial drugs, cow's milk). Lastly, the suitability and application of the mechanochemical effect at industrial cutting speeds is explored in turning experiments with these corrosion-resistant metals. Collectively, our observations, measurements, and analysis show that the gumminess of metals in cutting is due to sinuous flow; the gumminess can be eliminated by use of chemical media; and adsorption is the key to engendering the mechanochemical effect. Implications of the results for industrial processes ranging from machining to particle comminution, and for sustainable manufacturing are discussed.

1. INTRODUCTION

Several soft metals and/or highly strain-hardening metals and alloys have become indispensable in the defense, energy, aerospace, automotive and medical sectors [1,2]. Tantalum, niobium, austenitic stainless steels, and nickel are four such materials. The importance of these metals and alloys can largely be found in the shared attributes of being highly corrosion resistant and having strength at elevated temperatures. The corrosion resistance is derived from oxide films that develop on their surface. Tantalum is inert with virtually all organic and inorganic compounds at temperatures below 150°C, with the exception of hydrofluoric acid and fuming sulfuric acids. Below 150°C, tantalum is inert to all concentrations of hydrochloric acid, all concentrations of nitric acid, concentrations of sulfuric acid less than 98%, and concentrations of phosphoric acid less than 85% [3,4]. In fact, tantalum is virtually as inert as glass below 150°C – so similar that laboratory-based chemical reactions conducted in glass equipment can be transferred to tantalum equipment in industrial plants without fear of corrosion, contamination, or side reactions [4]. Due to its resistance to a variety of organic and inorganic compounds at elevated temperatures, tantalum is used extensively in the chemical processing industry, particularly as linings for pipes and vessels. Additional applications for tantalum include electronics (constituting almost 60% of all tantalum consumption) and bioimplants [2,4]. Often referred to as its sister element (at half the density and cost), niobium has similar corrosion properties as tantalum, although it tends to be more dependent on temperature and acid purity. It is resistant to most mineral and organic acids at temperatures below 100°C, with the exception of hydrofluoric acid [4,5]. Uses for niobium include rocket and jet engine applications; sodium vapor lamps; cathodic protection devices for large steel structures; condensers and evaporators in chemical processing; and superconducting magnets used in magnetic resonance imaging (MRI), nuclear magnetic resonance instruments (NMRI), and particle accelerators [2,4–6]. Austenitic stainless steels are corrosion resistant due to their chromium and nickel content. They are the most commonly used grade of stainless steels. Austenitic stainless steels are inert to nitric acid at practically all concentrations and temperatures, making Type 304 the material of choice in the construction of nitric acid plants [3]. Due to the general level of corrosion resistance they provide, coupled with strength, austentic stainless steels are used in applications such as building and construction, consumer products, and food processing. Nickel

has excellent resistance to caustic alkalies, neutral and alkaline salt solutions, and dry fluorine. At modest temperatures and concentrations, it also has some resistance to hydrochloric and sulfuric acids. It is widely used in chemical processing and storage, food processing equipment, high-temperature and marine applications [7].

Another key structural characteristic of these metals besides their corrosion resistance is their high strain-hardening capacity, besides being relatively soft (lower strength). The importance of these corrosion resistant and highly-strain hardening metals cannot be understated. Tantalum, niobium, and chromium (a key alloy elements in austenitic stainless steels) are considered strategic metals in the United States, based on the potential risks to their supply; and significant effects that a restriction in supply would have on national security and the economy [1,2]. Due to the corrosive environments and extreme temperatures in which they often operate, there are few substitutes. Unfortunately, the corrosion advantages of these metals are offset by their difficulty to machine, requiring special techniques with particular attention to machining parameters and cutting fluid choice [8]. They belong to a group of metals and alloys often termed as being 'gummy,' i.e., difficult to machine, and characterized by a tendency to form a built-up edge and galling of the workpiece surface [9]. This gumminess or poor machinability has been broadly attributed to their high strain-hardening capacity (ductility), though the underlying mechanics has not been explained. Recent work with soft annealed Cu and Al, also falling under the class of gummy metals, has shown that their gummy behavior in cutting is caused by an unsteady, and highly redundant, mode of plastic deformation – sinuous flow – that dominates the chip formation process [10–13]. This sinuous flow mode is characterized by large-amplitude folding, and large rotational components in material flow, with the chip composed of a series of folded layers stacked on top of one another. This sinuous flow results in large cutting forces and energy dissipation, 5-15 fold thickening of the material during chip formation indicating large strains, poor machined surface quality, e.g., rough surfaces with tears and crack-like defects, and large residual plastic strains on the surface [11,14].

Due to the essential role the corrosion-resistant metals fulfill, alternative methods are continually being sought to ease the difficulty in machining, such as cryogenically enhanced machining and use of tools with physical vapor deposition (PVD) hard coatings [8,15,16]. Recent research suggests there may be yet another alternative – the use of mechanochemical effects – changes in deformation response of a material induced by the application of a surface-adsorbing (SA) chemical medium to the initial workpiece surface. It has been shown in experiments, mostly

with Cu and Al, that through the application of such media to the workpiece surface prior to cutting, the large-strain deformation of a metal can be limited (disrupted), thereby reducing cutting forces and specific energy [11,17], and enhancing machinability. This inhibition of the deformation appears to be affected by a local ductile-to-brittle transition in the chip-formation zone, with the thick "folded chips" of the sinuous flow giving way to segmented chips characterized by fracture in the presence of suitable media. The use of mechanochemical effects offers a promising means to improve the machinability of these critical, corrosion resistant metals and alloys.

1.1 Problem Statement

It is now established that in metals with high strain-hardening capacity, those difficult to cut despite being relatively soft, a highly unsteady mode of plastic deformation termed sinuous flow [10–13] dominates the chip formation process. Furthermore, preliminary experiments with Cu and Al have shown that sinuous flow can be suppressed or modified via a mechanochemical effect by the application of a SA medium [17]. Three types of SA media have been identified in regard to effectiveness: those that are relatively material agnostic (working across metals), those that are material specific (specific to a metal), and those that have no effect [18]. Until now, experiments into the sinuous flow phenomenon have largely focused on copper and aluminum [17].

The present study seeks to expand the exploration of flow modes in cutting, and utilization of mechanochemical effects, to the critical technology metals and alloys of tantalum, niobium, austenitic stainless steels, and nickel. Since these metals are also considered gummy, based on their machining and deformation processing response, it is hypothesized that the gumminess here too is due to sinuous flow. And equally importantly, the sinuous deformation mode should be influenced by SA media akin to the Cu and Al model systems studied to date. It is of course possible that since these metals are so corrosion resistant, the SA media may not act in the same way as they do with Cu and Al if a corrosion-based mechanism was the underlying characteristic of the mechanochemical effect. Thus cutting experiments with these metals should also refine our hypothesis about the origins of the mechanochemical effect – is it due to corrosion or adsorption or something else? If a mechanochemical effect could be realized with these metals, then it should be possible to disrupt the sinuous flow in these metals too via the SA media effect, with attendant important benefits to industrial applications of these corrosion resistant metals.

The study is thus focused on the following closely coupled topics – analysis of the flow modes in these corrosion resistant (and highly strain-hardening) systems, understanding the coupling between flow and energy dissipation, how chemical media can be utilized to change the flow dynamics and stability of surface flow modes, and the underlying role of adsorption vis-a-vis corrosion in triggering the mechanochemical effect. The last exploration is particularly feasible since the metals selected are highly corrosion resistant, enabling further discrimination of the mechanism of the mechanochemical effect. In addition, prior research into the mechanochemical effect has largely consisted of the use of common, function-specific media intended for marking and adhesion, e.g., inks and glues. The present study expands the choice of media to a variety of organic media having well-documented adsorption properties but not traditionally considered for such applications. By investigating these other organic molecules – many actually suitable as corrosion inhibitors (e.g., plant extracts, antibacterial drugs), the role of adsorption in the mechanochemical effect is likely to be more fully understood and established. Lastly, chip formation at higher cutting speeds and temperatures is examined to determine if there are any changes in the flow mode arising from strain rate influences, and the characteristics, the media must possess to disrupt the flow mode effectively even at higher speeds.

Collectively, the results of the study will be used to support or refute the following proposed hypothesis for the mechanochemical effect suggested by work with Al and Cu – the medium action results from the formation of a thin, strongly adsorbed layer on the workpiece surface which influences the flow via the layer's effect on surface energy of the workpiece material and/or surface stress. The coupling of the effect to the flow mode is likely due to the fact the sinuous flow promotes formation of notch-like features in the deformation region due to the folding. The adsorbed layer likely triggers a crack at the notch tip causing the local ductile-to-brittle transition and "embrittlement".

1.2 Structure of the Thesis

To address elements of the hypothesis, the remainder of the thesis has been structured into four distinct chapters. Chapter 2 provides a comprehensive investigation into chip formation in tantalum (known for its severe gumminess) during low speed, orthogonal plane-strain cutting. Material flow is characterized using *in situ* high-speed imaging and digital image correlation when cutting dry and with a SA medium. Force measurements, hardness testing, surface characterization,

and microstructure analysis provide further support as to the nature of material flow during plastic deformation. This comprehensive approach permits comparison of tantalum deformation behavior to that of Al and Cu and an assessment as to whether the behavior supports or refutes tenets of the hypothesis concerning the micromechanics for the ductile-to-brittle transition brought about by the mechanochemical (MC) effect. Chapter 3 extends investigation into chip formation for stainless steel and niobium and explores the role of adsorption in the MC effect through the use of a wide variety of media – natural organic extracts, dyes, amoxicillin and cows' milk – many of which are eco-friendly. All media used represent multilayer adsorption, as no controls are imposed to influence layer formation. The impact of media concentration and oxide layer thickness are also studied. Chapter 4 probes the efficacy of the mechanochemical effect at industrial cutting speeds (hence, with thermal effects) by turning of copper, nickel, niobium, and stainless steel. In the process, SA media properties are further examined and suitability for industrial application are explored. Lastly, Chapter 5 provides a discussion of the findings of the work and how they collectively support and/or refute the proposed hypothesis, followed by potential avenues of future work.

2. CUTTING OF TANTALUM: WHY IT IS SO DIFFICULT AND WHAT CAN BE DONE ABOUT IT

(This chapter has been submitted to the *International Journal of Machine Tools and Manufacture* for consideration for publication. Co-authors: Mojib Saei, Debapriya Pinaki Mohanty, Anirudh Udupa, Tatsuya Sugihara and Srinivasan Chandrasekar.)

2.1 Abstract

Tantalum has long drawn the ire of machinist, being particularly difficult to cut. Often referred to as being 'gummy,' cutting of tantalum is characterized by very thick chips, large cutting forces, and a poor surface finish on the machined surface. These unfavorable attributes of the cutting have usually been attributed to bcc tantalum's high strain-hardening capacity, relative softness, and low thermal conductivity; and occurrence of a small shear plane angle. Here we show using *in situ* high-speed imaging that the gummy nature of Ta in cutting, including the large forces and thick chips, is actually due to the prevalence of a highly unsteady plastic flow – sinuous flow – characterized by large-amplitude folding and extensive redundant deformation. While sinuous flow was first uncovered in cutting of pure metals like copper and aluminum, both fcc, this flow and the associated folding is shown to be much more amplified and extreme in tantalum. Furthermore, sinuous flow is now demonstrated also in a model bcc system. *In situ* observations of the sinuous flow and gumminess are reinforced by force measurements, and chip morphology and cut-surface characterization. By application of a surface-adsorbing (SA) medium, e.g., permanent marker ink, to the initial workpiece surface, we show that sinuous flow can be disrupted and replaced by a more energetically favorable flow mode – segmented flow – with thin chips and > 70% reduction in the cutting force. This flow disruption is mediated by a local ductile-to-brittle transition in the deformation zone, due to the action of the SA medium – a mechanochemical (MC) effect in large-strain deformation of metals. Equally importantly, the MC effect and underlying segmented flow are beneficial also for machined surface quality – producing nearly an order of magnitude improvement in the surface finish, creating a surface with minimal residual plastic strain, and greatly reducing level of material pull-out. Thus, by use of the SA medium and triggering the MC effect, a promising new opportunity is demonstrated for improving the machinability of Ta by ameliorating its gumminess. As a result, Ta may now become viable for

use in a greater number of applications (e.g., gun barrel liners) – applications for which it has been hitherto considered but discarded due to its poor machining characteristics.

2.2 Introduction

Upon its discovery in 1802, Anders Ekeberg named his new element *tantalium* (now tantalum) after the mischievous Greek demigod Tantalus [19,20]. According to mythology, Tantalus was punished by Zeus for his mischief-making by being forced to stand eternally in a pool of water beneath a fruit tree, with the water always receding before being able to drink and the wind blowing the fruit-bearing branches out of reach [21]. Ekeberg felt the new element had the same tantalizing allure, finding its oxide unreactive with most acids and therefore, making it difficult to separate from tantalite ore [19,20]. For the design engineer and machinist, Ta continues to live up to its name: a metal with some highly desirable properties but notoriously difficult to machine, often attributed to its high strain-hardening capacity. Bcc Ta, like its sister element Nb that lies immediately above it in the periodic table, even though relatively soft (~ 200 HV) is often described as 'gummy' to cut – i.e., with notoriously poor machinability. Chip formation with Ta is characterized by significant side flow, very thick chips indicative of large strains, large forces, and poor surface finish due to seizing, tearing, and unclean chip separation [3,15,22–24]. These characteristics have been attributed to a small shear plane angle and occurrence of unsteady flow [22,23].

While Ta is extraordinarily difficult to machine, there are many important applications for which it is well-suited over other metals, due to its high corrosion resistance (similar to that of glass) and refractory nature (melting point ~ 3000°C) [4]. Some of its uses, and potential uses, include jet engine and missile components, penetrator projectiles, nuclear reactor components, chemical processing equipment, and biomedical implants (hip and knee replacement parts, skull plates, dental implants) [2,4]. The poor machinability of Ta has, however, precluded its wider use. For example, an application for which Ta has been considered but not implemented, due to its poor machinability, is in explosively-bonded, gun-tube liners in small arms. Over a decade ago, the United States Army Research Laboratory (ARL) partnered with industry and national laboratories to research and develop such a liner to improve gun barrel life. In 2008, an industry partner began work on implementing crown broach cutters to rifle prototype Ta-lined gun barrel tubes. A crown broach set was used that consisted of 60 individual cutter heads, each containing 9 pairs of teeth.

Each pass of the broach was used to cut 18 grooves and increase the depth of the grooves by 10 μm. Two barrel sections were broached; but each time, a tooth on the broach broke. Failure analysis revealed galling and metal build-up on the teeth as the cause of tool breakage. The galling was attributed to any number of different issues: dull or chipped tooth, insufficient cooling at the tooth, chip interference during the cutting process, and/or misalignment of the broach. Conventional rifling of the barrels was subsequently abandoned in search of other machining processes [25]. Unfortunately, little research has been done to understand and address the poor machinability of Ta, in the past two decades, beyond the earlier parametric studies of cutting conditions (e.g., speeds/feeds, tool rake angle/ material and cutting fluids) on tool life [26,27].

The difficulty of machining Ta has been ascribed to various factors. First, Ta although soft and quite ductile, work-hardens extensively, albeit, at a slow rate [15,28]. This results in extensive deformation in chip formation and, often, also in a built-up edge near the tool tip [24,26]. Second, the low thermal conductivity and diffusivity of Ta, causes the heat from the shear zone to disperse slowly [15]. To prevent excess heat generation, low cutting speeds are recommended, typically in the range of 0.5 to 1.5 m/s for finishing cuts in turning [26,27]. Lastly, friction at the tool-chip interface is often blamed for the thick chip, arising as it were from a small shear angle [23,24]. Friction also amplifies the built-up edge and heat generation. While these factors serve as signatures of the poor machinability, their underlying causes require a basic understanding of the mechanics of large strain deformation in Ta.

Tantalum is certainly not the only metal described as being gummy to cut – various commercially pure (CP) metals such as Cu, Al and Nb in the annealed or partially worked state; and stainless steels and Ni alloys, also share that moniker, consistent with their large strain-hardening. In machining, these materials too form thick chips, and exhibit large cutting forces and poor surface finish for a range of cutting parameters – typically low to moderate speed and undeformed chip thickness. It has been shown, recently, using high-speed *in situ* imaging of the cutting, that the gummy behavior of CP Cu and Al, both fcc metals, is due to chip-formation occurring by a large-amplitude folding process, that is fundamentally different from chip-formation by conventional simple-shear with a well-demarcated shear zone/plane [10,12]. In the light of this finding, it is prudent to ask if a similar (folding) type of chip formation mechanism is responsible for the extraordinarily poor machinability and gummy nature of Ta.

In this study, we examine the plastic flow dynamics behind why Ta is so difficult to cut, and how its machinability could be improved by control of these flow dynamics. The flow dynamics are examined using high-speed *in situ* imaging of the cutting, complemented by force and surface quality measurements. We capture various details of the chip-formation deformation at high resolution and decipher the reason(s) as to why Ta is gummy to cut. We go further and show that, by exploiting a recently uncovered mechanochemical (MC) effect with common media such as inks and glues [17,18,29], the cutting of Ta is greatly improved, with > 70% reduction in cutting force, and an order of magnitude improvement in surface finish. Equally importantly, the mechanochemically machined surface is much less deformed – a state that may be called "minimally strained". The results offer a means for solving not only the Ta machining problem, but also that prevalent with other similar bcc metals like Nb. In the process, a highly unsteady flow mode – sinuous flow with large-amplitude folding – uncovered earlier in cutting of CP Cu and Al (fcc metals), is also shown to be present in cutting of Ta, a model bcc system.

2.3 Experimental

To examine plastic flow modes in machining of Ta, experiments were carried out with a linear, plane-strain (2D) cutting system (**Fig. 2.1a**). In this system, the metal workpiece in the form of a rectangular plate is moved at constant velocity V_0 relative to a tool of rake angle α; the tool cutting edge is normal to V_0 and the set depth h_0 is the undeformed chip thickness. The cutting results in a chip of nominal thickness h_c, which moves up the rake face with velocity V_c.

The cutting was observed *in situ* and recorded using a high-speed CMOS camera (PCO pco.dimax) coupled to an optical microscope (Nikon Optiphot), see **Fig. 2.1b**. The chip-formation zone – the region of interest – was illuminated by a 120-W halogen lamp. A glass block was clamped against the workpiece along its cutting length. This constraint ensured that there was no side-flow of the workpiece material during cutting, thus ensuring plane-strain; and that the tool and workpiece were in the same focal plane for the imaging. The imaging configuration provided a spatial resolution of 1.4 μm per pixel and a recording area as large as 1296 × 1296 pixels; the images were recorded at 500 fps. The high-speed image sequences were post-processed using a digital image correlation (DIC) technique, enabling quantitative analysis of the deformation in terms of displacements, velocities, flow lines, and strain rate and strain fields [10,30]. Refer to Appendix A for more information concerning DIC. The three components of the resultant force,

viz., cutting, thrust, and lateral, were measured using a three-axis piezoelectric dynamometer (Kistler 9254, natural frequency ~ 2 kHz). Quality of the cut surface was characterized in terms of topography using a large-area 3D optical profilometer (Zygo NewView 8300), and mechanical state by residual plastic strain and indentation hardness.

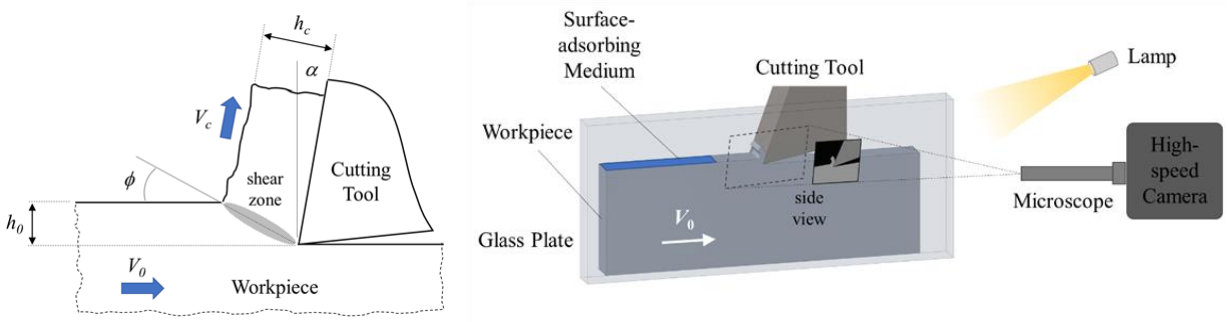

(a) (b)

Figure 2.1. Plane-strain cutting configuration used in experiments. (a) Schematic showing key parameters and classical shear zone model of deformation. (b) *In situ* imaging of material flow in the deformation zone using a high-speed camera coupled to an optical microscope. The side surface of the metal workpiece being imaged is constrained by a glass block to prevent transverse material flow and ensure a common focal plane.

The Ta was procured in an initially annealed state, with hardness of 200 HV. The elemental composition of the Ta, as determined by energy-dispersive X-ray spectroscopy (EDX) at multiple voltages (10, 15, 20 kV), was confirmed to be 94% Ta, falling under the category of commercially pure (CP) Ta. The material was annealed by heating in vacuum to 1100°C and holding for 90 min; under vacuum, the sample was furnace-cooled to room temperature in 24 hrs. An optical micrograph of the annealed microstructure is shown in **Fig. 2.2**. The metallographic procedure for the sample consisted of first being mounted on top of a cold mount acrylic resin (Lecoset 100) cast using super glue. Polishing was performed using sandpaper with progressively finer grit (600-, 1200-, and then 2000-grit), followed by 3-μm and 1-μm diamond paste. The sample was then polished using a GIGA900 Vibratory Polisher for 6 hours using colloidal silica solution. Etching was carried out with a mixture of sulfuric acid : nitric acid : hydrofluoric acid = 30:10:10 by volume. The sample was swabbed with cotton soaked in the acid mixture. After swabbing the sample 10 times, residual acid on the sample was washed quickly with tap water, and the sample surface was dried with compressed air. The process was repeated three times for a total of 30 swabbings. The microstructure is clean and even at higher magnifications there are no precipitates or second phase

particles visible. The grain size, as determined by the lineal intercept method, was 40 μm in the shorter direction, and with aspect ratio of 2.8. Samples for the linear cutting experiments were prepared in plate form, approximately 80 mm length × 25 mm height × 6 mm width, by milling. The surface on which the cutting was done was left untouched during the sample preparation as to ensure that it was still in the annealed condition. Cutting was done along the 80-mm length, using a high-speed steel (HSS) tool with $\alpha = 10°$, $V_0 = 2$ mm/s and nominal h_0 of 40 to 50 μm. The exact value of h_0 was measured in every experiment. A few experiments were performed at h_0 of 30 and 90 μm to determine effect of undeformed chip thickness on flow dynamics. The cutting edge was wider than the workpiece width of 6 mm, ensuring plane-strain. A secondary set of experiments was done at higher V_0 of 625 mm/s, in a rotary plunge-turning configuration, with a 25.4-mm diameter bar of annealed Ta. This speed is typical of commercial machining of Ta. For this set, α was 0°, $h_0 \sim 50$ μm (feed/rev), and the tool/chip width was 3.8 mm ($> 10h_0$), again ensuring plane-strain. The edge radius of the tool in all cases was < 5 μm. All the cutting experiments were done dry without use of any fluid.

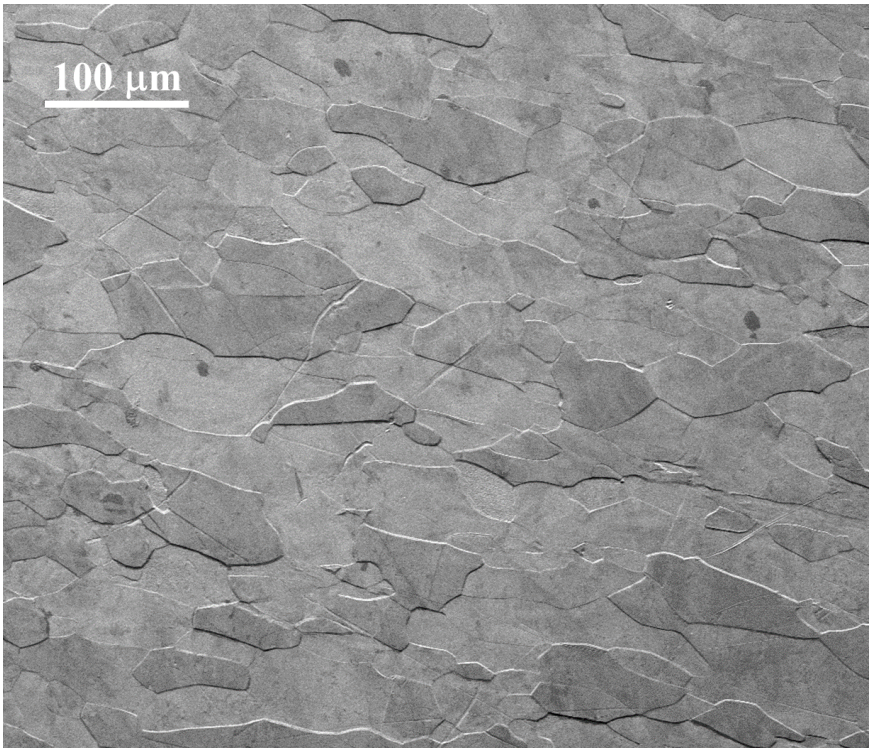

Figure 2.2. Ta workpiece microstructure.

2.4 Results

The high-speed *in situ* imaging of the chip formation, together with the force and surface quality characterization, have provided comprehensive characterization of plastic flow dynamics, and the role of the flow field in influencing energy dissipation and workpiece surface deformation.

2.4.1 Chip Morphology

An overview of the chip-formation flow in Ta is readily obtained from SEM observations of chip morphology. **Fig. 2.3a** shows a plan view of the chip for V_0 = 2 mm/s. The chip is very thick, with a chip thickness ratio ($\lambda = h_c/h_0$) at the base of the chip of ~ 47; this represents an extraordinary level of thickening. The free surface of the chip consists of a series of ridges, each spanning the width of the chip, see **Fig. 2.3b**. The width of the individual ridges, which appear to be folds, is on the order of 100 μm.

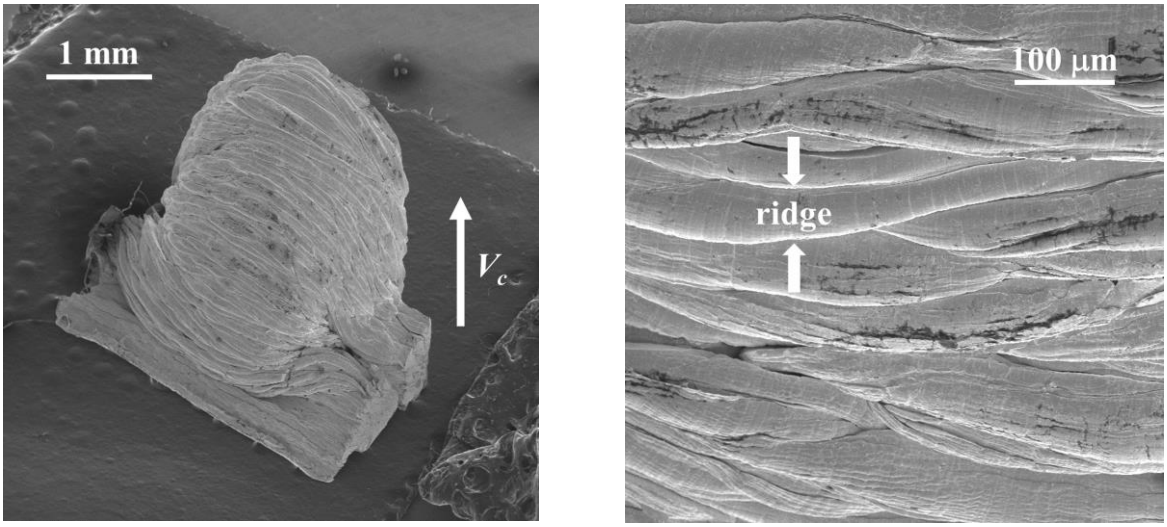

(a) (b)

Figure 2.3. Morphology of Ta chip by scanning electron microscopy (SEM). (a) Free (back) surface of the chip showing stack with ridges and severe thickening. (b) Close-up view of the ridges on the chip free-surface. The ridges run mostly straight across the chip width but with some interlacing. α = 10°, h_0 = 40 μm, V_0 = 2 mm/s.

The chip produced at the much higher V_0 of 625 mm/s (**Fig. 2.4**) has a very similar morphology. This chip is again very thick, with λ of ~ 40; and the chip free surface consists of ridges with a thickness of ~ 100 μm. In fact, multiple overlapping/interweaving ridges span the

width and length of the chip. These observations suggest that the chip formation mechanics is essentially unaltered in the speed range of 2 mm/s to 625 mm/s; the latter speed is quite typical of commercial cutting speeds for Ta [26]. In fact, this type of chip morphology has been reported elsewhere also: in turning of Ta at a cutting speed of 1,000 mm/s for rake angles of -5° to 25° with feed rate 0.0125 mm/rev [22,23]; and in machining of Nb at similar speeds [6].

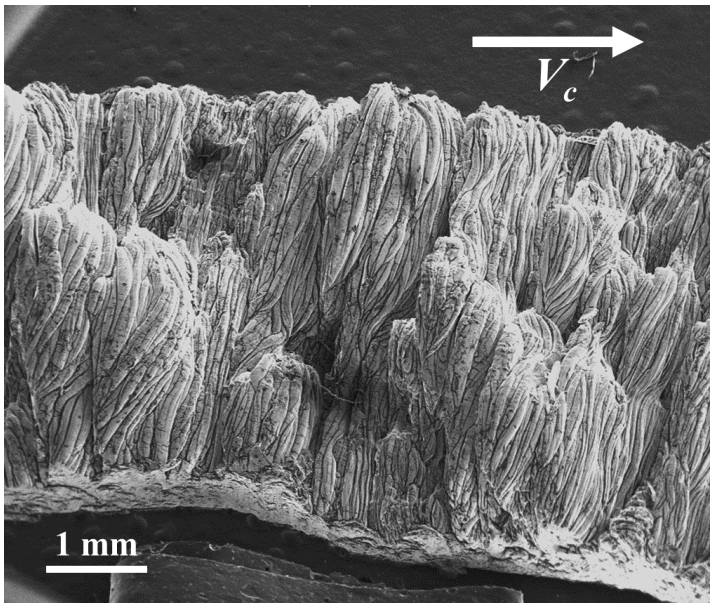

Figure 2.4. SEM image of free-surface of chip, obtained from turning of Ta, showing multiple stacks of ridges. $\alpha = 0°$, $h_0 = 50$ μm, $V_0 = 625$ mm/s.

2.4.2 Flow Characterization: Sinuous Flow and Folding

In order to understand the origin of the thick chip (equivalently, the gumminess) and the texture on the chip free-surface, we observed the dynamics of chip formation and underlying material flow, *in situ*, using a high-speed camera. **Figures 2.5a-f** show six frames selected from a high-speed image sequence of the cutting, with background color map highlighting the effective (von Mises) strain field. The development of the flow/deformation can be understood by following the motion of a series of surface points demarcated in the images, and the streaklines superimposed onto the images. (Note: A streakline is a line formed by the loci of all particles that have passed continuously through a fixed point; at some instant in time, the particles are marked and connected with a line [31].). At time t_0, (frame 1 – **Fig. 2.5a**) a bump begins to develop on the workpiece surface ahead of the advancing tool, between the surface points P_1 and P_2. These points appear to

serve as pinning points (extremities) between which the bump develops. Upon advance of the tool (frame 2 – **Fig. 2.5b**, Δt = 0.2 s), two additional bumps, denoted as $P_2 - P_3$ and $P_3 - P_4$, are nucleated behind the original bump ($P_1 - P_2$). The first bump ($P_1 - P_2$) meanwhile has grown in amplitude, with its axis (dotted line) rotating counterclockwise, and sheared into a fold. Similarly, after another 0.2 s (frame 3 – **Fig. 2.5c**) and as the tool advances further, bump $P_3 - P_4$ develops into a fold, by similar rotation and shearing, with significant growth in amplitude. This process of bump formation, and subsequent development of the bump, into a fold is a recurring event (quasi-periodic) as seen in frames 3-6 (**Figs. 2.5c-f**), where several other folds are highlighted along with their nucleating bumps and pinning points (P_4 through P_8). The bumps and folds vary in amplitude; for example, $P_5 - P_6$ shows a bump/fold that is much greater in amplitude than the others. A total of seven distinct folds have formed over a 1.0-s duration (**Figure 2.5**). Collectively, the folds, once fully developed, create a fan-like structure with the axes of the folds converging to a common location near the tip of the tool, see for example **Fig. 2.5c** and **Fig. 2.5e**. The strain within the chip is greatest at this point of convergence, with values in the range of 8-10 (background color map, **Fig. 2.5**). The repeated folding is the reason for the large chip thickness and ridge-shaped morphology of the chip free-surface. The chip is thus comprised of a series of folds that are "stacked" up on top of one another, albeit, with the fold-axes fanning out from the tool edge.

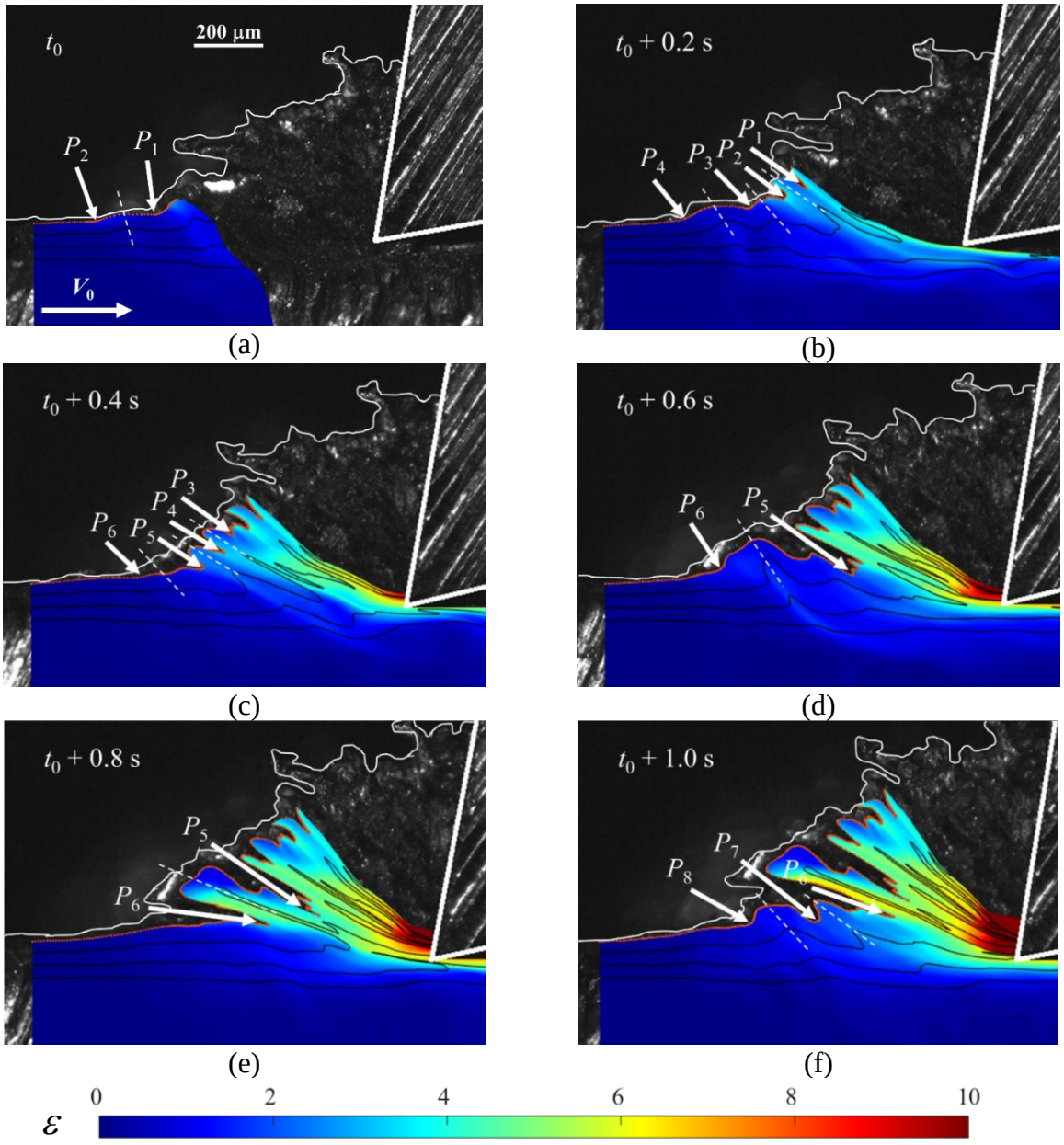

Figure 2.5. High-speed *in situ* image sequence of development and progression of sinuous flow with folding in Ta. Overlaid onto the image are the strain field (background color), which is quite heterogeneous; and a few, highly-sinewy streaklines which show significant vortex-like (rotation) components of flow. (a) At some time t_0, a small bump develops on the workpiece surface ahead of the tool between pinning points P_1 and P_2. This bump formation involves differential grain deformation, and resembles plastic-buckling of a thin surface layer. (b) After 0.2 s, the pinning points P_1 and P_2 move closer together, with the axis of the bump rotating counter-clockwise. During this period, multiple additional bumps nucleate on the surface between $P_2 – P_3$ and $P_3 – P_4$. (c) At 0.4 s, bumps $P_1 – P_2$, $P_2 – P_3$, and $P_3 – P_4$ have all increased in amplitude, and rotated/sheared to become folds. Another fold $P_4 – P_5$ has developed as well, along with a new bump forming between $P_5 – P_6$. (d) As the tool advances, bump $P_5 – P_6$ continues to grow in size. (e) At 0.8 s, bump $P_5 – P_6$ has progressed into a fold by the usual rotation/shearing. (f) After 1.0 s, bumps $P_6 – P_7$ and $P_7 – P_8$ have formed, for a total of seven distinct buckling events. The folds create a fan-like structure that spreads out from the tool tip. The strain field is highly heterogeneous with strains ranging from 10 (tool-tip) to 4 elsewhere in the chip body. $\alpha = 10°$, $h_0 = 40$ μm, $V_0 = 2$ mm/s.

The plastic flow process resulting in the folded chip has significant vortex-like components, as revealed by the wavy (sinewy) nature of the streaklines shown in **Fig. 2.5**. This is a direct consequence of the repeated bump and fold formation, and the folds which stack up together to form the chip. Furthermore, the strain field arising from this flow is highly heterogeneous, with the chip strains ranging from 4 to 10 (color in **Fig. 2.5**); the highest strains of 8-10 occur in the vicinity of the tool edge. This type of highly unsteady, vortex-like flow has been termed as sinuous flow [10,12]. If the chip formation is viewed as a material shape-change via a plastic deformation process, then it is clear this sinuous flow with folding is characterized by extensive redundant deformation. While similar sinuous flow has been observed earlier in cutting of annealed commercially pure fcc metals like Cu and Al [10,12,18], the Ta chip formation represents perhaps the most extreme case of folding observed to date, and, the first case, in a bcc system. And it is the folding that gives rise to the "ridge-like" structures observed on the chip free-surface in **Figs. 2.3 and 2.4**. The observations of sinuous flow in Ta attest to the generality of occurrence of this type of flow, especially with metals that show significant strain-hardening capacity. Indeed, sinuous flow has also been observed recently in machining of stainless steels and niobium. The sinuous flow chip-formation highlighted in **Fig. 2.5** is fundamentally different from the textbook (conventional) picture of chip formation, usually depicted as arising from smooth laminar flow due to a shear plane/zone.

Another consequence of the folding-induced redundant deformation is the high specific force and energy dissipation in the primary deformation zone (Note: Specific force is force divided by the product of chip width and undeformed chip thickness.). In fact, the measured specific force for machining of Ta in our cutting experiments reaches a maximum of 15,800 MPa (see Sec. 2.4.4). For reference, the specific force in finish turning of hard steels (~ 60 HRC, 700 HV) is ~ 8,150 MPa, for a 10° rake angle and 40 μm undeformed chip thickness [32,33]; note that the annealed Ta is only ~ 30% as hard as these steels. Such large forces also cause tool-life in Ta cutting to be low [24]. The gummy nature of Ta, typified by the thick folded chips and large forces, is thus a consequence of chip formation by sinuous flow.

It is instructive to compare and contrast the attributes of the folding and sinuous flow in bcc Ta with those observed in annealed or partially worked (fcc) Al and Cu. The folding and mushroom-like features on the chip free surface seen in the Ta cutting (**Fig. 2.5**) are broadly similar to those observed in Al and Cu, and characteristic of the sinuous flow mode. For Al and Cu, each

fold originates as a bump, bound by pinning points, on the workpiece free surface ahead of the cutting tool. This bump then develops then into a fold by a rotation and shearing process very much analogous to that in Ta shown in **Fig. 2.5** [10,12]. Note that in this type of unsteady flow, there is no shear plane that can be demarcated. Hence thick chip formation cannot be a consequence of a small shear plane angle as has been suggested [23,24]. Furthermore, the sinuous flow in Ta is much more extreme than in the Al and Cu, as seen from the chip thickness ratio. This ratio reaches values up to ~ 40 in Ta, whereas it is typically 10-20 for the Cu and Al.

2.4.3 Enhancing Cutting by Suppressing Sinuous Flow and Folding

The flow characterization has demonstrated that sinuous flow with folding is the principal reason for the poor machinability and gumminess of Ta. Furthermore, the nature of this flow is much more extreme in Ta than in the other gummy metals like Cu and Al. Consequently, attempts to facilitate or improve the machining of Ta must focus on disrupting the sinuous flow mode and replacing it with a more favorable mode that involves less energy dissipation in chip formation. Prior work suggests that this could potentially be accomplished to some degree by varying the initial state of the workpiece material or via changes in the deformation geometry. It has been found with other gummy metals like Cu and Al that pre-straining the workpiece material (to reduce its strain-hardening capacity) prior to the cutting, by a deformation process like rolling, can reduce the extent of the sinuous flow, and, sometimes, even fully replace it with a more favorable smooth laminar flow [34,35]. The forces with laminar flow are much smaller, and the surface finish is simultaneously much improved. Another strategy is to make the tool rake angle quite positive – a change in the deformation geometry – which also promotes laminar flow with its attendant benefits [8]. In fact, this has been recommended also for Ta machining, where relatively thin chips have been reported at large rake angles [22,23]. But positive rake angle tools often result in lower tool life, a problem also with Ta [24], because of geometrical weakening of the tool edge. Hence, these approaches to mitigate the effects of sinuous flow are not always viable options or even preferred. An alternate, more general method, to suppress sinuous flow and improve the cutting is therefore desirable.

A possible general method to suppress sinuous flow in Ta is suggested by recent work that has uncovered a new mechanochemical (MC) phenomenon (effect) in cutting of soft and/or highly strain-hardening metals [17,18,29]. The occurrence of (mechano) chemical effects in plasticity and

fracture has for long been known, see for example discussions of effects associated with the names of Roscoe, Joffe, Rehbinder and Bangham [36–41]. These effects pertain largely to changes in mechanical response of solids when their surface is exposed to action of chemical media. The recently uncovered MC effect is characterized by a ductile-to-brittle transition occurring in the cutting zone of metals undergoing sinuous flow – this transition being affected by chemical media that are adsorbed onto the metal surface. One dramatic manifestation of this phenomenon occurs when surface-adsorbing (SA) media, often household items such as inks, dyes and glues, are applied to the initial workpiece surface of gummy metals like Al and Cu prior to the cutting. The normally active sinuous flow mode is replaced by segmented flow that is dominated by fracture. This change in flow mode occurs via a local ductile-to-brittle transition in the deformation zone – the development of the sinuous flow being arrested by onset of quasi-periodic fracture. Importantly, the segmented flow results in much smaller cutting forces, lower chip strains, and improved quality of the cut surface [17,18,29]; hence, it is a much more favorable mode for chip formation, including chip management [42]. It is worth noting that this flow transition is not lubrication-induced, for the SA medium is not present anywhere near the tool-chip interface but only on the initial surface of the workpiece ahead of the chip formation zone and advancing tool (**Fig. 2.1b**).

Three general categories of SA media have been identified based on the efficacy of the MC effect, and compatibility with the metal surface [17,18]. The first type (Type-I) is media whose action is fairly material-agnostic, meaning they show the aforementioned MC effect with a variety of different gummy metals. Such media display strong physical adsorption to the metals. This type tends to be common, relatively benign media used in general adhesion applications or for marking metals. Examples of such media (used in prior experiments with Cu and Al) by trade name include Scotch restickable glue stick (a N-Vinylpyrrolidinone-based adhesive), Scotch super glue gel (a cyanoacrylate-based adhesive), Gorilla super glue (a polyurethane-based adhesive), Sharpie permanent marker, Dykem metal marking ink, and Paper Mate Liquid Paper correction fluid. Note that the inks in this category are essentially dyes, and not colloidal inks. The second type (Type-II) of SA media that exhibit the MC effect are those whose action is material-specific, meaning they have a chemical affinity for only a certain metal – likely undergoing a chemical reaction with the metal surface – and change the flow of media. An example of this type is isopropyl alcohol and its effect on aluminum [29]. The last type of media (Type-III) does not demonstrate the MC effect at all, for this type adsorbs poorly or not at all to the metal surface. Examples in this category

include distilled water, variously commonly used metal-cutting lubricants (e.g., Mobil 1), and paraffin wax.

Cutting with an ink-film (SA medium)

Since Ta during cutting displays sinuous flow and extreme folding, even more so than Cu and Al, we hypothesized that it would respond to SA media much the same as these gummy metals do – that is a mechanochemical effect would be manifest. To test this hypothesis, we decided to carry out cutting experiments with ultrathin films (~ 200 nm thick) of Sharpie permanent marker ink as the SA medium. This ink had been identified as an effective Type-I medium in previous studies and, furthermore, it is easily applied to the workpiece surface. More information concerning the physical and chemical properties of this ink, its capacity to develop a film, and characterization of ink-film thickness is provided in Appendix B.

The experiments with the ink were conducted in the linear cutting configuration (**Fig. 2.1b**), with the nominal cutting conditions being $\alpha = 10°$, $V_0 = 2$ mm/s and $h_0 = 40$ μm, unless otherwise specified. This configuration permits for the probing of both the sinuous flow and its response to an SA medium, concurrently, in the same experiment (cutting pass), by applying the SA medium to only one half of the workpiece surface along its cutting length (**Fig. 2.1b**). In the present case, the ink film, ~ 200 nm thick (see Appendix B), was applied to the latter half of the cutting length. Thus in a single pass, the tool is cutting the uncoated surface of the workpiece first followed by the ink-coated surface.

Flow dynamics and chip morphology

Figure 2.6 is a SEM image showing a cross-sectional (length × thickness) side view of the chip from one of the experiments ($h_0 = 50$ μm) in which the ink was applied to one half of the length. The cutting of the initial (uncoated) half of the workpiece produces the familiar folded, fan-like chip arising from sinuous flow, akin to that described earlier (**Fig. 2.5**). The thickness of the chip is ~ 1.7 mm at the base, which represents a nearly 34-fold (very large) thickening of the material during the deformation process. The folding causes the chip to have large variations in its thickness, as well as in the free surface of the chip having an irregular mushroom-like morphology

when viewed from the side (**Fig. 2.6**). The mushroom structures correspond to the ridges noted earlier.

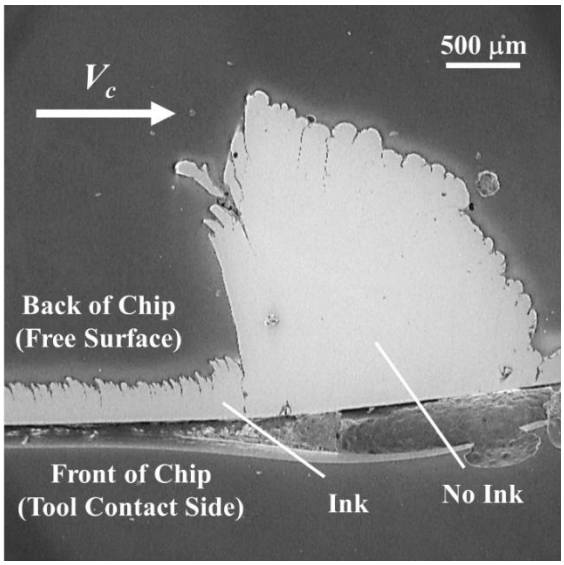

Figure 2.6. SEM image of chip (length × thickness, cross-section) produced by cutting Ta workpiece that is coated with an ink medium only along part of its cutting length. The initial part of the cutting length is uncoated. The non-inked region shows a very thick chip (~ 34-fold thickening), with mushroom-like free-surface morphology, formed by sinuous flow and folding. In contrast, the chip from the inked-region is quite thin (~ 5-fold thickening) and forms by segmentation flow. A sharp change in the chip morphology and underlying flow from sinuous-folding from $\alpha = 10°$, $h_0 = 50$ μm, $V_0 = 2$ mm/s.

In direct contrast, the morphology and structure of the chip from the latter part of the cut, the ink-coated region, is fundamentally different (**Fig. 2.6**). Firstly, the chip now is much thinner (~ 250 μm) corresponding to $\lambda \sim 5$. Secondly, the chip shows a segmented morphology, with cracks running across a significant fraction of the chip thickness; this morphology is very reminiscent of the well-known, saw-tooth chip. Furthermore, the segments are fairly regularly spaced (quasi-periodic), running continuously (straight) across the width of the chip. This may be seen from **Figs. 2.7a and b** which are SEM images of the chip free surface. Closer examination of the saw-teeth reveals that each of them is made up of smaller segments (**Fig. 2.7b**). **Figure 2.7c** is an optical microscope image of the chip surface in contact with the tool rake surface. Cracks are apparent on this surface all along the chip width, with the crack spacing (~ 270 μm) coinciding with the spacing of the segments. This shows that the segments are a consequence of a fracture process, wherein the cracks appear to have initiated on the chip free-surface (see ensuing *in situ* observations) and propagated towards the tool edge and at least partially through the chip thickness. The cross-

sectional view of the chip in **Fig. 2.6** does not clearly show this aspect of the crack feature, most likely due to the discontinuous nature of the cracks; that is, it is difficult to discern the actual beginning and end of the large saw-tooth segments from the cross-sectional view.

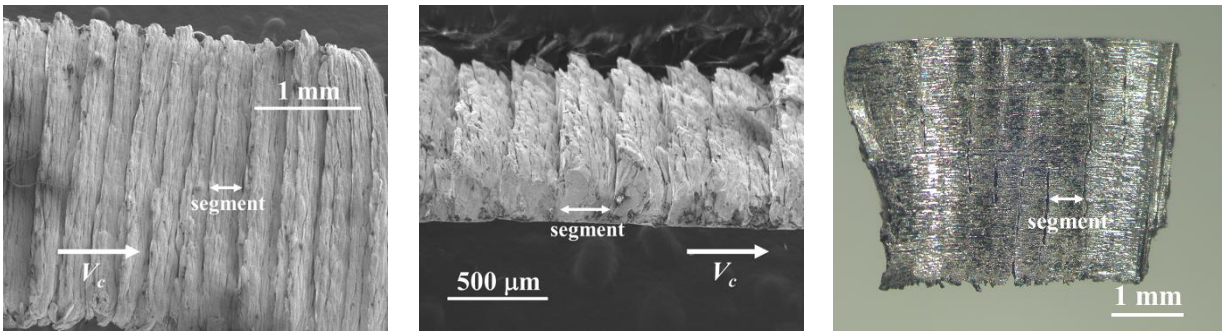

(a) (b) (c)

Figure 2.7. SEM images of morphology of segmented chip in cutting of Ta with ink applied to the workpiece surface. (a) Free (back) surface of the chip showing segments, that are somewhat regularly spaced, running straight across the chip width without any meandering. (b) Higher magnification, perspective view of the chip free-surface (same as in (a)) showing straight segments, and saw-tooth chip. (c) Chip surface in contact with the tool rake surface showing cracks. $\alpha = 10°$, $h_0 = 40$ μm, $V_0 = 2$ mm/s.

High-speed imaging was successful in unraveling the mechanics of segmented chip formation and in showing the segmentation (fracture) to in fact originate on the chip free-surface (**Fig. 2.8**). The frames in the figure show crack initiation and growth over a 0.41 s cutting duration, with the motion of points P_1 and P_2 describing the segmentation. At time t_0 (**Fig. 2.8a**), P_1 and P_2 are very close in proximity and on opposite sides of the nucleating crack. After 0.17 s (**Fig. 2.8b**), the crack has grown in length (distance between P_1 and P_2 has increased) with P_2 becoming the crack tip. After an additional 0.24 s (**Fig. 2.8c**), the crack substantially elongates and widens. This fracture process repeats periodically leading to the segmented chip.

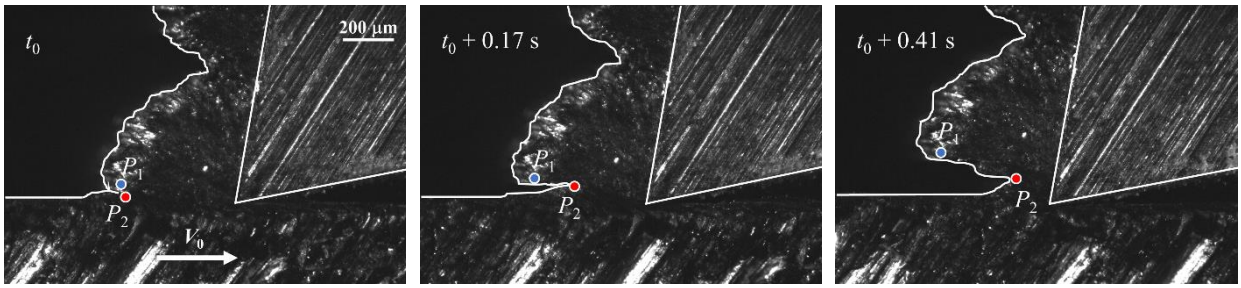

(a) (b) (c)

Figure 2.8. Frames from a high-speed image sequence showing development of segmentation flow in Ta cutting with the ink-medium applied. (a) A crack initiates on the chip free surface ahead of the advancing tool at time t_0. P_1 and P_2 are close together on opposite sides of the incipient crack. (b) The crack grows after 0.17 s with the distance between P_1 and P_2 increasing, and P_2 becoming the crack tip. (c) With further advance of the tool (0.41 s), the crack rapidly opens up and propagates towards the tool tip. This crack nucleation repeats periodically creating a segmented chip. $\alpha = 10°$, $h_0 = 30$ μm, $V_0 = 2$ mm/s.

Figures 2.9a and b are SEM images that show effect of h_0 on chip formation and segmentation. For h_0 of 50 μm and 90 μm, the corresponding deformed chip thickness (h_c) values are ~ 230 μm and 380 μm, respectively. Sometimes, the actual segmentation lengths are somewhat difficult to discern from these cross-sections due to the preponderance of smaller segments within larger ones. However, for h_0 of 50 μm and 90 μm, features of similar appearance and size are separated by a distance of 60 μm and 100 μm, respectively. Thus, an 80% increase in h_0 translates into a roughly 65% increase in h_c and segment spacing, suggesting a self-similar scaling of the segmentation. **Figures 2.9a and b** also reveal that at the larger h_0, the cracks that initiate on the free surface of the chip do not propagate all the way to the chip under-surface, as with $h_0 = 40$ μm, but are arrested part way into the chip thickness. This aspect of the segmentation is also very similar to what has been observed in segmented chip formation in conventional (no ink application) cutting of materials such as copper, brass and magnesium [43]. The much thinner segmented chip, which is indicative of reduced deformation levels, and the key role of fracture in effecting the segmentation (**Figs. 2.7, 2.8**), together suggest that the deformation energy and forces should be much smaller when cutting with the ink-medium applied.

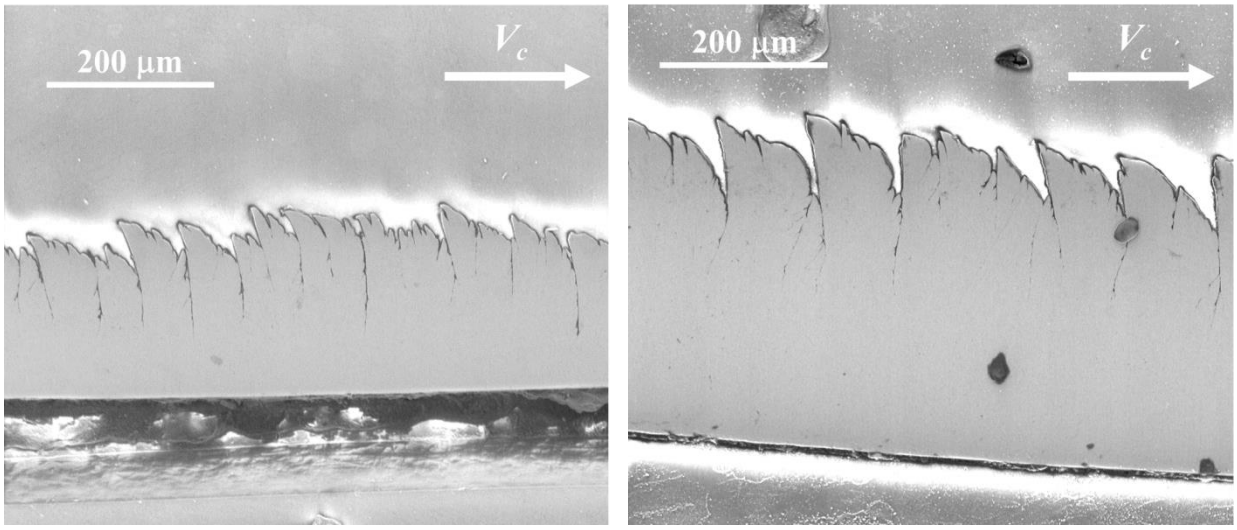

(a) (b)

Figure 2.9. Scaling of the segmentation with h_0 when cutting Ta in presence of SA (ink) medium. (a) An undeformed chip thickness h_0 of 50 μm results in a deformed (segmented) chip with mean thickness 230 μm. The mean spacing between the segments is ~ 60 μm. (b) An undeformed chip thickness h_0 of 90 μm results in deformed (segmented) chip with thickness 380 μm, and segment spacing ~ 100 μm. Note that both the thickening of the chip and the segment spacing scale linearly with h_0. α = 10°, V_0 = 2 mm/s.

2.4.4 Forces

One of the distinguishing quantitative attributes of the mechanochemical effect, observed in prior work with Cu and Al, is a large decrease in the cutting and thrust forces [10,17,29]. As an aside, this aspect has also been confirmed by others [44] using the same ink media as us [10]. A dramatic reduction in forces was also observed in the cutting of Ta (ink). **Fig. 2.10** is a plot of forces showing this major reduction in specific cutting (F_c, power) and thrust (F_t) force components (Note: Specific force is force divided by the product of chip width and undeformed chip thickness.). In the uncoated region, the first part of the cut, F_c climbs steadily to a maximum value of approximately 15,800 N/mm^2; for reference, the corresponding F_c for finish turning of a hardened steel (hardness ~ 60 HRC > 3× Ta hardness) is nearly 50% smaller, ~ 8,150 N/mm^2, for the same rake angle and undeformed chip thickness [32,33]. These large forces are an important contributor to high tool wear in Ta cutting [24]. Upon encountering the coated region, the latter part of the cut, F_c abruptly and steeply drops to an approximate average value of 3,740 N/mm^2, a reduction of ~ 75 %. This major reduction in F_c is undoubtedly due to the local ductile-to-brittle

transition in flow, from sinuous to segmented, that is induced by the SA medium (Sharpie ink). Furthermore, the F_c in the coated region oscillates with time, with oscillation (half) amplitude that is 15% of the average. Using a periodogram, the dominant frequency in the F_c oscillation was determined to be 0.59 Hz. This matches well with the segmentation frequency of the chip (~ 0.6 Hz) determined by metallography. The origin of the oscillation is as follows: as an individual segment is forming, F_c increases continuously until a fracture event occurs, leading to a sudden decrease in the force. This process of periodic segmentation with corresponding force drops was found to occur throughout the region in which the SA medium was applied. The force oscillations (**Fig. 2.10**) and chip morphology (**Fig. 2.7b**) observations also reinforce what we have reported earlier – that when segmentation occurs in cutting, with the segments running straight across the chip width, then this segmentation is also manifested as a force drop. The same is not always true if the segments meander across the chip width [43].

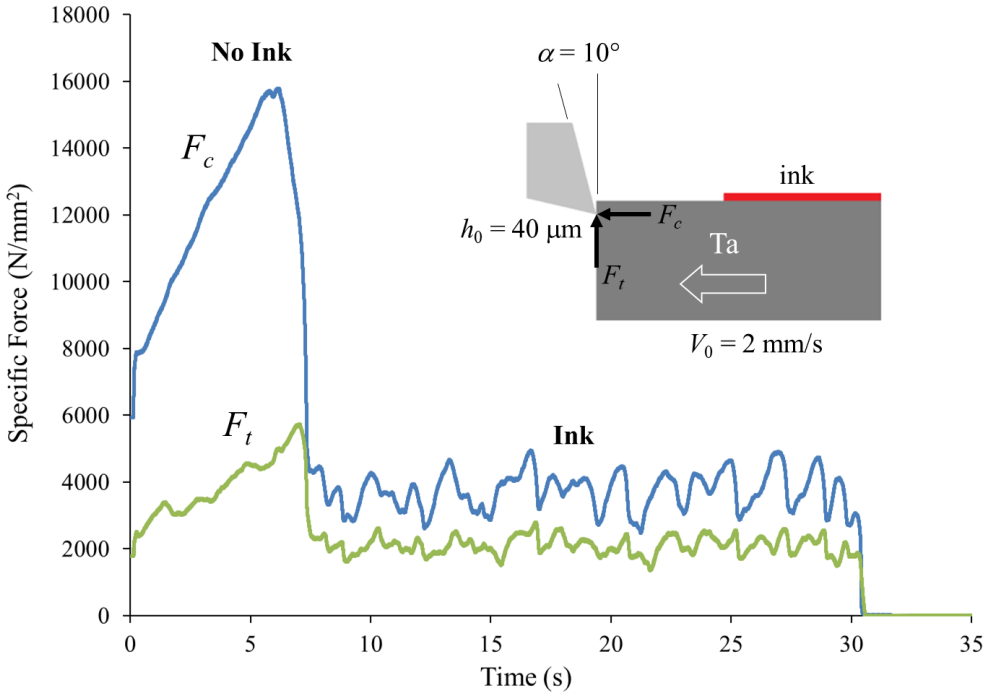

Figure 2.10. Specific cutting (F_c) and thrust (F_t) forces when cutting Ta workpiece coated with ink only along part of its cutting length (see inset). F_c in the uncoated region is very high due to the sinuous flow. A dramatic (~ 75%) decrease in this force is seen when cutting over the inked region with segmented flow. Also, in the uncoated region, F_c is rapidly increasing. In contrast, in the inked region, F_c is not only small but steady, with small periodic fluctuations that are a consequence of the segmentation; it is reflective of a more stable cutting process. $\alpha = 10°$, $h_0 = 40$ µm, $V_0 = 2$ mm/s.

The thrust force component F_t also decreases, and oscillates similarly as F_c, due to the Sharpie medium application. However, the F_t reduction is less pronounced, only ~ 65%. Since F_t has more to do with the contact conditions at the tool-chip interface, this observed reduction in F_t implies that the segmentation-type flow, a consequence of the MC effect, is also more favorable from a friction standpoint. However, in order to recognize this, it is important to examine the F_t magnitude and not the ratio F_t/F_c which is often taken as a measure of the cutting friction (coefficient). In the present case, this ratio for the sinuous flow (~ 0.35) is actually much smaller than for the segmentation case (~ 0.56), and would lead to an erroneous interpretation of how the tool-chip friction is influenced by the flow.

Another demonstration of the F_c reduction due to the MC effect can be found in **Fig. 2.11**. In this case, the forces were measured when cutting a Ta workpiece that had been only periodically marked with the Sharpie ink. The ink itself was applied as bands of width ~ 5 mm, alternating with non-inked regions also of 5 mm width (inset shows the bands on the chip free surface after deformation). Here, the F_c fluctuates between high (uncoated) and low (coated) values, with the force fluctuations matching the spatial frequency of the ink bands, confirming the characteristic force-reduction attribute of the MC effect.

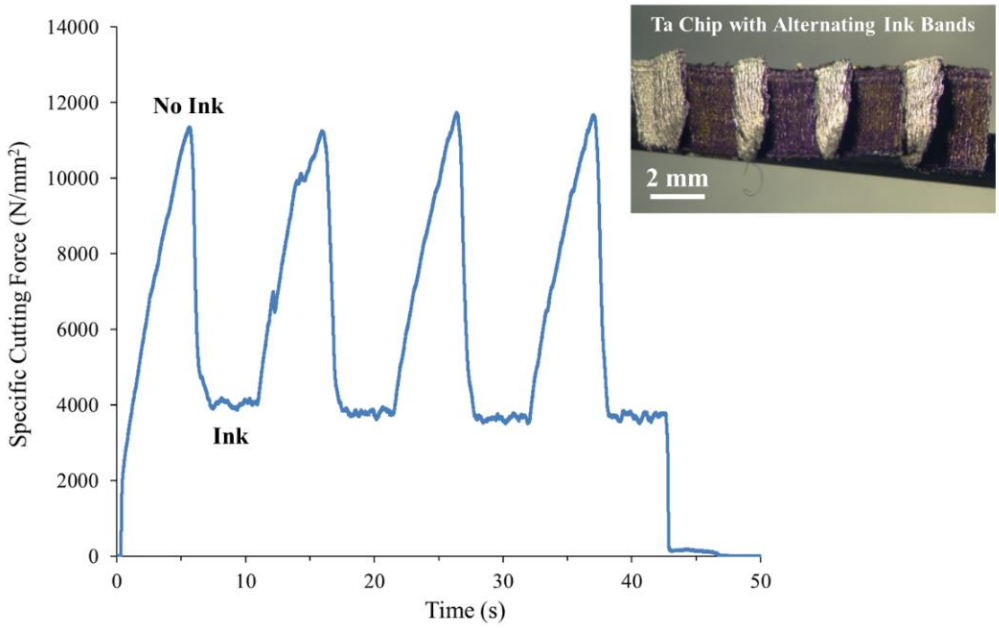

Figure 2.11. Specific cutting force trace when cutting Ta sample inked at regular intervals along the cutting length. See inset chip picture for how ink (dark) and non-ink regions alternate). The force is high in the non-inked region (sinuous), but quite small in the inked region (segmented) bands. $\alpha = 20°$, $h_0 = 40$ μm, $V_0 = 2$ mm/s.

2.4.5 Surface Quality

The quality of the machined surface was characterized in terms of surface topography (roughness, tears and material pull-out), hardness and residual plastic (deformation) strain, to determine whether there were any major benefits from the MC effect.

Surface topography

Accompanying the force reduction, due to the MC effect, is a pronounced, nearly order of magnitude, improvement in the surface topography of the newly (cut) created workpiece surface. **Figure 2.12** shows 3D surface profiles along the Ta workpiece length, obtained via optical profilometry, for the inked and non-inked regions; this profile was put together by stitching together a number of individual profiles. As is apparent, the surface corresponding to the non-inked region has a markedly rough texture – valleys with ridges. This suggests significant material pull-out during the cutting. Importantly, the arithmetical mean height roughness *Sa* of the surface corresponding to the inked region is ~ 2 μm, an approximately 9-fold improvement over that of the non-inked surface (*Sa* ~ 18 μm). It should be noted that this *Sa* value also includes contributions from material pull-out. The tool marks seen along the length of the surface in the inked region indicate active cutting, not plowing. Furthermore, this part of the cut surface is largely devoid of defects like tears and material pull-outs in contrast to the non-inked region. The topography improvement is also evident in the line profiles provided in **Fig. 2.12.**

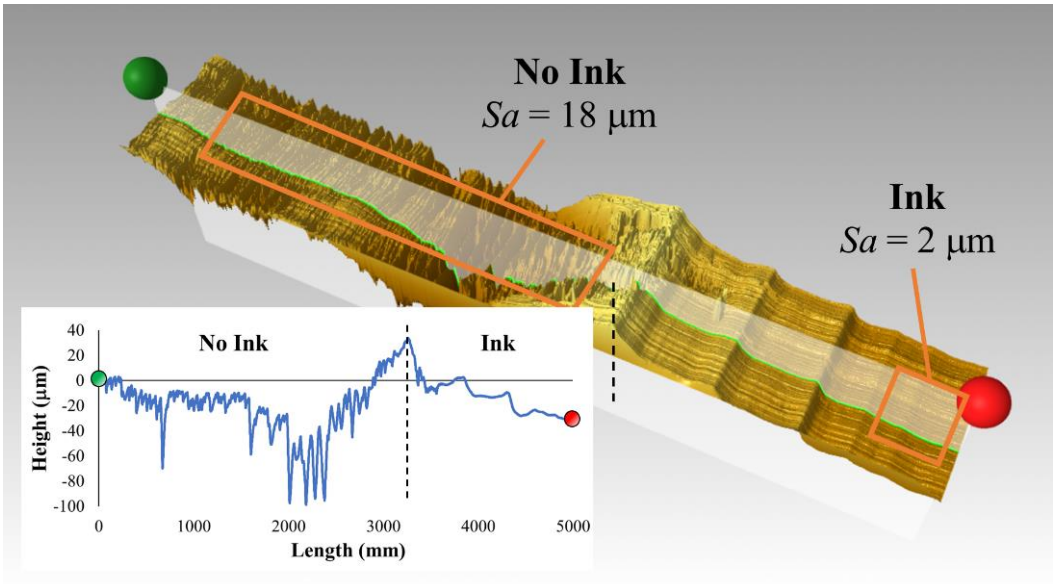

Figure 2.12. Optical profilometer image of Ta surface produced by cutting with and without application of an ink-medium. The transition in the surface topography between the inked and non-inked regions is quite striking, indicating almost an order of magnitude improvement in surface topography due the MC effect. Sinuous flow (no ink) results in noticeable surface grooves with ridges and material pull-out. The latter can also be inferred from lack of tool marks on the cut surface. The *Sa* value in the no-ink region is ~ 18 μm. Application of ink results in a largely defect-free surface produced by active-cutting with tool marks. The *Sa* value in the inked region is ~ 2 μm. $\alpha = 10°$, $h_0 = 40$ μm, $V_0 = 2$ mm/s.

Surface strain

The DIC analysis of high-speed image sequences was also used to map the residual plastic strain field on the workpiece surface in the wake of the tool [10,18], i.e., the cut surface. This was done by integrating the strain rate field along path lines that traverse the deformation zone and become part of the workpiece [10]. These strain values were then averaged to determine the strain at a given depth. **Figure 2.13** shows the variation of residual plastic strain with depth from the cut surface for the sinuous (no ink) and segmented (ink) flow cases. The surface produced under conditions of sinuous flow is intensely deformed, with a large surface strain, $\varepsilon \sim 5.5$. In contrast, the workpiece surface produced under conditions of segmented flow enabled by the MC effect shows a much smaller surface strain, $\varepsilon \sim 1.7$. Additionally, the depth of the deformed layer on the cut surface is also much reduced for the segmented flow case. If we use $\varepsilon = 0.5$ as the cut-off value to describe the extent of the deformed layer, then the depth of the strained layer is ~ 30 μm for the segmented flow and ~ 90 μm for the sinuous flow. Thus the MC effect is valuable also for

producing a cut surface with much less residual plastic strain, in fact a "minimally strained" surface. This should be beneficial for enhancing fatigue life of the surface, especially since fatigue crack nucleation is strongly influenced by the plastic strain state [45,46].

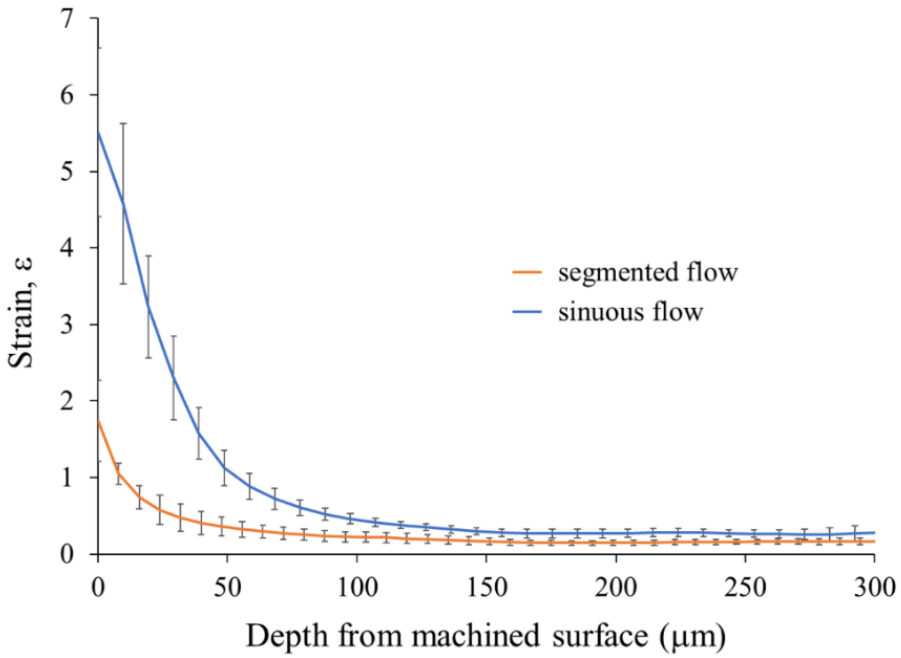

Figure 2.13. Variation of residual plastic strain with depth from the machined Ta surface for the different flow modes. For sinuous flow (no ink), the average ε is ~ 5.5 on the cut surface; while at a depth of ~ 90 μm from the cut surface, ε ~ 0.5. For segmented flow (ink medium), the average ε ~ 1.7 on the cut surface, while ε ~ 0.5 occurs at a depth of 30 μm from the cut surface. Thus, both the strain at the surface and the depth of the deformed surface layer are both much smaller for the segmented flow case. α = 10°, h_0 = 40 μm, V_0 = 2 mm/s.

Surface hardness

Nanoindentation using a Berkovich indenter was used to determine the hardness on the cut (machined) surface and subsurface. A 13 × 3 array of indentations was made on the surface/subsurface created from the sinuous flow region, while an 8 × 3 array was used in the segmented flow region. The indenter penetration used was 2000 nm, and the array spacing between rows and columns was 12.5 and 100 μm, respectively. **Figure 2.14** shows a plot of the hardness vs. depth, obtained from the measurements. It is readily apparent that the surface produced by the sinuous flow has a much greater hardness than the one produced by the segmented flow (ink).

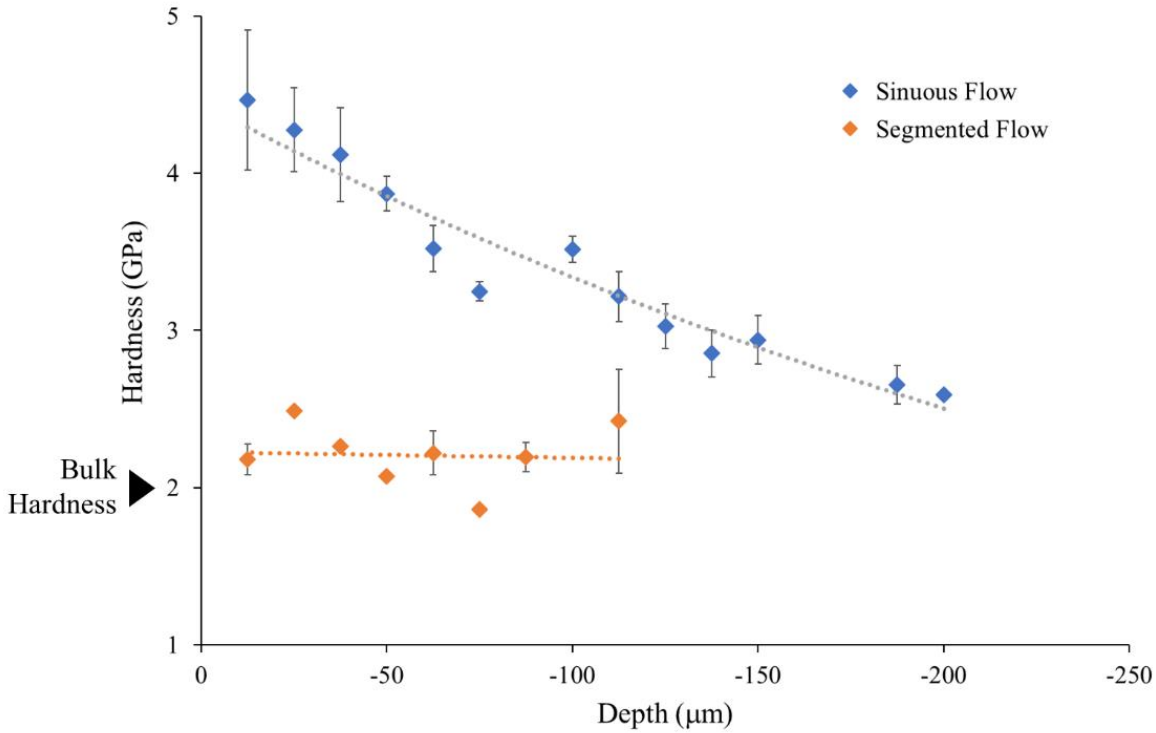

Figure 2.14. Variation of nano-hardness with depth from the machined surface for Ta surfaces produced by the two flow modes. Near the cut surface, the hardness is ~ 4 GPa for the surface produced by sinuous flow whereas it is only ~ 2 GPa for the surface produced by segmented flow. The latter hardness is approximately the same as the initial bulk Ta hardness. This suggests negligible straining of the surface when cutting with the ink applied, pointing also to a means for producing "strain-free" surfaces. $\alpha = 10°$, $h_0 = 40$ μm, $V_0 = 2$ mm/s.

For example, in the sinuous flow case, the hardness is ~ 4.3 GPa at a depth of 10 μm from the surface; this may be considered as the machined surface hardness. This is consistent with the very large plastic strains ($\varepsilon \sim 5.5$) measured on the cut surface in the sinuous flow case (**Fig. 2.13**). The hardness is seen to decrease gradually with depth from the machined surface, but even at a depth of ~ 200 μm it is greater than the bulk Ta hardness of ~ 2 GPa. In contrast, for the segmented flow, the hardness on the cut surface is ~ 2.2 GPa (**Fig. 2.14**), which is very close to the bulk Ta hardness; and the surface strain is $\varepsilon \sim 1.7$. Thus the MC effect causes very little strain hardening of the Ta workpiece surface during cutting, consistent with the reduced level of strain ($\varepsilon \sim 1.7$) measured on this surface (**Fig. 2.13**). The results point to a means of producing "strain-free" or "minimally strained (damaged)" surfaces utilizing the MC effect.

Chip hardness

To analyze chip hardness, nanoindentation with a Berkovich indenter was used. The chip was cold mounted using Lecoset 100. This acrylic resin-based mount constrained the chip at its periphery, preventing buckling and slippage. The sample 'puck' was also supported by a stainless steel base. The indentation penetration depth was ~ 2 μm. By ensuring that the chip dimensions in each direction were at least 8 times greater than the corresponding indent dimensions, any substrate/mount effect on chip hardness was eliminated. A total of 18 indentations were made in the sinuous flow portion of the chip: 7 indentations including the origin (200 μm apart) were made vertically (y-axis in **Fig. 2.15**), 5 indentations (200 μm apart) were made horizontally (x-axis) to the right of the origin, and 6 indentations (140 μm apart) were made along a 45° diagonal. For the segmented flow case, hardness was sampled at three locations along the chip, towards each end and in the middle. A vertical line consisting of 3 indentations, 50 μm apart, was made at each sampling site.

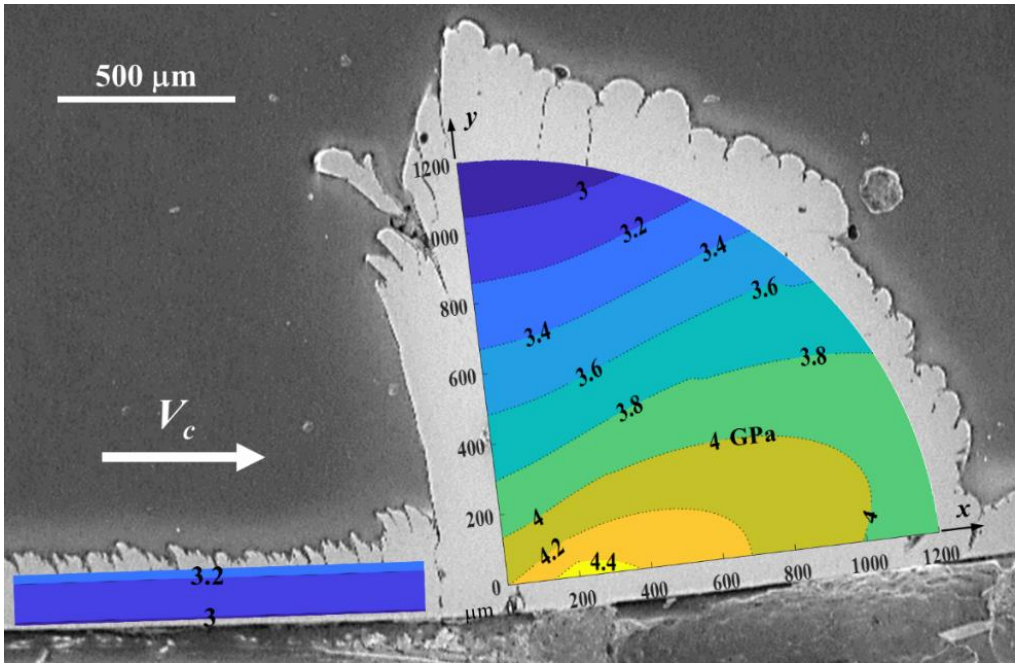

Figure 2.15. Contour map of nano-hardness of Ta chip. The workpiece was partially uncoated and partially inked along its cutting length. For the sinuous flow portion of the chip (right, uncoated), the hardness is greatest in the region in contact with the tool rake face. For the segmented flow case (left, inked), the hardness is uniform throughout the chip (~ 3 GPa) and much less than in the sinuous flow case. α = 10°, h_0 = 50 μm, V_0 = 2 mm/s.

Figure 2.15 is a nanohardness contour map for the chip that combines the data from the sinuous and segmented flow regions. The chip hardness values mirror the corresponding workpiece surface hardness. For the sinuous-flow chip, the highest hardness (~ 4.5 GPa) is measured in the region immediately adjoining the tool rake face. This value is close to that measured on the corresponding workpiece surface. The hardness is seen to steadily decrease with distance from the rake face into the chip. The hardness pattern is consistent with the folding behavior revealed by the *in situ* imaging. As the chip is being formed, folds are continually added to the developing fan-like structure. The addition of each fold compresses the material in contact with the rake face, resulting in higher hardness. In the segmented flow portion of the chip, the hardness is smaller (~ 3.2 GPa) and nearly uniform throughout.

2.5 Discussion

Our *in situ* high-speed imaging of chip formation, complemented by force measurements, has revealed key aspects of material flow in cutting of Ta and the reason why Ta, although soft, is very difficult to cut. Chip formation in Ta, as in annealed Cu and Al, occurs by large-amplitude folding with the chip made up of a stack of folds (**Figs. 2.3, 2.4**). The severity of the folding is not only much greater in the Ta than in the Cu and Al, but there are important differences in the fold morphology. In the case of Cu and Al, the deformed chip thickness is relatively constant, but the chip free surface has singular mushroom-like structures [10]. Each of these mushroom structures results from a fold and the folds themselves are stacked up one on top of the other to constitute the chip. However, in the Ta, the deformed chip progressively increases in thickness upon cutting due to a piling-up of folds in the form of a fan-like structure (**Fig. 2.5f**), as opposed to a vertical stacking of the folds in Cu and Al. This fan-like structure also results in a different type of strain distribution within the deformed Ta chip; the strain is concentrated near the tool tip which serves as the apex of the fan, as opposed to the more distributed and less heterogeneous straining in the Cu and Al. The streakline pattern in the Ta chip shows a highly sinewy flow with significant vortex-like components (**Fig. 2.5f**) – this flow is very much similar to the sinuous flow mode first uncovered in cutting of Cu and Al. The sinuous flow with folding is characterized by extensive redundant deformation and high strains (4-10) which explains the very large forces seen in cutting of Ta and the poor machinability of this material – explaining why Ta is so gummy. Also, since Ta is a bcc system, the observation of sinuous flow in this system provides further evidence for its generality.

Although the folding is more amplified in Ta, the folds nonetheless result in the same type of mushroom-shaped features on the chip free surface (**Fig. 2.6**) as observed in Cu and Al. The interface between successive mushroom features has the topography of a notch. When cutting in the presence of surface–adsorbing (SA) media, these notches give way for a crack to propagate, thereby transitioning sinuous flow into segmentation flow. The disruption of sinuous flow by segmented flow strongly resembles a local ductile-to-brittle transition that is affected by the SA media, with attendant large drop (> 75%) in the cutting forces (**Fig. 2.10**). These observations, together with the earlier work on Cu and Al [17,29,43], strongly suggest that the local ductile-to-brittle transition mediates the MC effect vis-à-vis deformation, and that the segmentation flow mode is efficient from an energy standpoint.

In Ta, the folds are relatively continuous and run straight across the width of the chip (**Figs. 2.3a,b**) in contrast to the meandering folds observed in Al and Cu. Even in some instances where they are interrupted, or interlaced, with other folds, there are no breaks that occur along the length of individual folds. This continuity of the folds largely explains the periodicity of the segmentation when cutting in presence of the SA media, and the relative consistency in segment shape across the width of the chip.

While various details of the micromechanics of the flow transition and the MC effect are still being worked out, we can highlight some of the necessary conditions needed for this effect to be manifest, based on the current observations and others made earlier with Cu and Al. Firstly, sinuous flow with large redundant deformation should mediate the chip formation (absent the medium). Secondly, the notches between incipient folds play an important role in triggering the fracture and segmentation. Thirdly, and most important, are the changes in surface properties of the metal that are caused by the medium. We address this last point in greater detail below.

It is tempting to attribute the ductile-to-brittle transition to some form of metal corrosion that is caused by the SA medium. However, the observance of the MC effect in Ta dispels this assertion, as Ta is one of the most corrosion-resistant metals known. Since Ta is immune to attack by most acids, any corrosive action by the Sharpie marker ink is highly improbable. Instead, strong adsorption of SA media to the metal surface is likely the requisite condition. It is well-known that adsorbates can change the surface energy of the "metal surface". This offers a route to explaining the observed brittle behavior by invoking a reduction in surface energy ahead of incipient crack tips, during the chip formation process, *a la* Griffith. While attractive again at first sight, this is

extremely unlikely given that one will have to invoke implausible permeation mechanisms to explain ink penetration into the metal. That leaves the only other thermodynamic parameter in solids – surface stress – that is affected by adsorption as the probable cause. Organic molecules such as those present in the ink when adsorbed onto metal surface are known to cause changes in the surface stress [47]. This stress, analogous to a residual stress, can be of sufficient magnitude, when amplified by the crack-like features such as seen here, so as to cause fracture (segmentation). We hope to address the mechanics of this phenomenon in future papers.

Since adsorption is believed to be critical to the MC effect, additional considerations (e.g., thermal effects on adsorbate) must be made when choosing SA media for higher cutting speeds. However, we have identified media (e.g., protein rich media, cow's milk) that suppress sinuous flow at higher cutting speeds for a range of 'gummy' metals and alloys. While this aspect is beyond the scope of this article, an in-depth treatment of the MC effect at high cutting speeds will be the topic of a future paper.

Our experiments point to many benefits that can be realized via use of the MC effect with highly strain-hardening metals. In no order of importance, they range from improved surface quality to improved cutting performance. With regard to quality, it has been demonstrated that the MC effect can significantly improve the poor surface finish that results from sinuous flow (absent the medium). Besides finish, other elements of machined surface quality are also positively impacted: major reduction in residual plastic strain (**Fig. 2.13**), suppression of tears and material pull-out, and minimal surface hardening. In fact, the machined surface hardness is practically the same as that of the bulk Ta, see **Fig. 2.14**. In terms of cutting performance, the substantial cutting (> 75% reduction) and thrust force reductions realized, should be beneficial for tool life and process quality. Lastly, a larger range of cutting parameters become available for the cutting, such as using smaller positive rake angles. More broadly, the MC effect provides a simple route for effecting extraordinary broad improvements in cutting of gummy metals.

2.6 Conclusions

Using high-speed *in situ* imaging, we show that the extreme 'gummy' behavior of the refractory metal, tantalum, in cutting is due to sinuous flow, with large-amplitude folding, driving chip formation. The chip produced by sinuous flow is composed of a series of folds that are stacked together, a morphology that is quite distinct from that of a conventional chip produced by laminar

flow with well-defined shear zone/plane. The folding in Ta is much more severe than in other gummy metals like annealed Al and Cu. Various key attributes of the sinuous flow such as large heterogeneous strains (4-10), extensive redundant deformation and large energy dissipation, have been quantified via the high-speed imaging and force measurements. The occurrence of the sinuous flow in a bcc system further attests to the generality of this deformation mode and to the close connection between this flow mode and the machinability attribute of "gumminess".

When the cutting is done in the presence of a surface-adsorbing (SA) medium, e.g., permanent marker ink, the sinuous flow is disrupted and replaced by a segmented flow mode, via a local ductile-to-brittle transition in the flow in the deformation zone – a mechanochemical (MC) effect. The segmented flow gives rise to a saw-tooth chip. The MC effect causes a fundamental change in flow dynamics and chip morphology. Importantly, there is a large (> 70%) drop in the cutting force and specific energy, another key defining attribute of the MC effect. The MC effect produces major improvements in the quality of the cut surface – smoother surface topography, reduced material pull-out, and minimal plastic straining on the surface. Thus, use of an appropriate SA medium and the MC effect offers a promising route for increasing the machinability of Ta by disrupting the sinuous flow. This approach is likely to be of value even for cutting other gummy metals like Nb and ferritic stainless steels (bcc), and Ni alloys and austenitic stainless steels (fcc).

The severity of the folding and extreme sinuous flow in Ta offer opportunities to better understand the coupling between flow dynamics and the MC effect, even more so than is feasible with other metals like Al or Cu. Wide-ranging application of mechanochemically-assisted machining in industrial practice will benefit from fundamental understanding of adsorbate-metal interactions, for this will help in selection of the right type of adsorbate molecules and in the means of their application. Ongoing work also seeks, among other things, to demarcate the parameter space (e.g., speed) wherein the MC effect is prevalent, and further elucidation of the flow micromechanics, especially the coupling between surface plasticity and thermodynamics of adsorbed films.

3. ROLE OF ADSORPTION IN THE CUTTING OF 'GUMMY' METALS VIA A MECHANOCHEMICAL EFFECT: SURVEY OF NATURAL EXTRACTS, ORGANIC DYES, AMOXICILLIN, AND COWS' MILK AS ADSORBATES ON STAINLESS STEEL AND NIOBIUM

(This chapter has been prepared for consideration for publication. Co-authors: Debapriya Pinaki Mohanty, Mojib Saei, Anirudh Udupa and Srinivasan Chandrasekar.)

3.1 Abstract

Soft and/or highly strain hardening metals are among the most difficult to cut. Often referred to as being 'gummy,' these metals exhibit sinuous flow – an unsteady, highly redundant mode of plastic deformation characterized by large amplitude folding that gives rise to thick chips, high cutting forces, and poor workpiece surface quality. Fortunately, it has been found that appropriate adsorbed chemical media can effectively create a ductile-to-brittle transition, shifting sinuous flow to a more favorable, segmented flow via a mechanochemical effect – a change in the deformation behavior of the metal due to the presence of the chemical media. Much of the work exploring the mechanochemical effect in the cutting of metals has used common, benign media for coating and adhesion, e.g., inks and glues. Using Type 304 Stainless Steel and Nb as test metals, it is revealed that a much larger selection of media exists that can engender a mechanochemical effect, many of which are readily available, environmentally friendly, and potentially more easily applied in an industrial setting. Experiments with these different media support the hypothesis that adsorption is key to the mechanochemical effect and ultimately, media that promote the mechanochemical effect have the same effectiveness – indicating selection of such media should be based solely on process parameters and other considerations.

3.2 Introduction

Soft and/or highly strain hardening metals have long frustrated machinists. When cut, they tend to generate thick chips, high cutting forces, and defects on the cut surface (e.g., cracks, tears) [10]. Examples include Al, Cu, Ta, Nb, pure Fe, Ni alloys, and stainless steels. These metals are aptly described as being 'gummy.' This 'gummy' behavior originates from sinuous flow – an

unsteady, highly redundant mode of plastic deformation characterized by large amplitude folding. Sinuous flow initiates from a plastic buckling instability on the workpiece surface [10,12].

To mitigate sinuous flow, work hardening and/or increased lubrication at the tool-chip interface are commonly employed [18]. Work hardening pre-strains the metal, reducing strain-hardening capacity and hence surface buckling. Friction at the tool-chip interface can exacerbate sinuous flow upon its initiation. However, work hardening is not always feasible and the extreme contact pressure and temperature at the tool-chip interface make lubricant penetration challenging [48]. Recent research provides yet another option – the suppression of sinuous flow via a mechanochemical effect [17,18]. A mechanochemical (MC) effect is a change in the deformation behavior of a material due to the presence of a chemical medium [38]. It has been revealed that application of an appropriate surface-adsorbing (SA) medium to the free surface of a metal can prompt a ductile-to-brittle transition during cutting, inhibiting sinuous flow in preference of one that is more favorable, namely segmented flow [17]. This results in lower cutting forces, more manageable chips, and markedly improved finish of the cut workpiece surface.

Until now, much of the investigation into the MC effect in the cutting of metals has been performed using readily available, common media for coating and adhesion, e.g., inks and glues [17,18]. Since adsorption is believed to be key to the MC effect, a literature review was conducted to determine other adsorption-dependent processes and identify additional adsorbate-metal pairings to explore the role of adsorption on the MC effect more fully. Some of the most common adsorption-dependent processes involving metals were corrosion inhibition, wastewater contaminant removal, and protein adsorption (fouling) to medical implants and food processing equipment [49–52], with most focused on the use of natural organic compounds. A brief review of those processes and the nature of the adsorbates follows.

3.3 Background

Within the past decade, there has been increasing interest in green corrosion inhibitors, those derived from natural products such as plant extracts [53,54]. The appeal is derived from them being eco-friendly, typically having low toxicity and being biodegradable. Most of the studies reviewed examined the effectiveness of a green corrosion inhibitor through the immersion of the metal in an electrolyte solution consisting of a corrosive agent (typically an acid, e.g., HCl, H_2SO_4) and a small concentration of the natural adsorbate. Electrochemistry reveals inhibition efficiency,

type of adsorption (physical vs. chemical), relative strength of adsorption, and rate of adsorption. Some of the common green corrosion inhibitors found in the literature included plant/seed extracts [55–61], organic dyes [62–67], and antibacterial drugs [68,69]. In general, some of the factors contributing to the inhibition efficiency of organic compounds include: carbon chain length, molecular size, aromaticity and/or conjugated bonding, bond strength to metal surface, type and number of bonding atoms in the molecule (either π or σ), and the ability of a layer to become compact or cross-linked [70,71]. The most effective green corrosion inhibitors often contain N, S, P, or O atoms in their structure, with inhibition efficiency following the sequence P > S > N > O [54,71].

Wastewater treatment is another area of interest in the use of metal adsorbents. Several industries (e.g., textile) expel wastewater that contains synthetic and natural dyes. Many of these dyes can be harmful to aquatic flora and fauna [72,73]. The most conventional wastewater purification treatments rely on biological oxidation and physicochemical processes (coagulation/flocculation and adsorption on activated carbon) [73]. However, these treatments have limited efficiency. For biological treatment processes, toxic and/or non-biodegradable organic substances are problematic. In the case of physicochemical processes, the dye contaminant is simply transformed into a different phase, yielding a new and different form of pollution that requires additional treatment [73]. Due to the inefficiencies of these processes, other methods of dye contaminant removal have been explored. One of the more promising classes of emerging technologies is photocatalytic oxidations – in particular, heterogeneous photocatalysis (photodegradation) using TiO_2 and Nb_2O_5 particles [73–75]. Adsorption of the dye to the surface of the oxide particles is necessary and critical. Dyes present an attractive opportunity in the study of the MC effect in metal cutting that is difficult to realize with the use of natural extracts/oils, inks, and glues. While adsorption of natural extracts and inks/glues can be attributed to multiple organic compounds, dyes tend to be purer. Dye purity permits consistent dilution enabling investigation of concentration on the MC effect.

Protein adsorption is of great concern in the biomedical industry and food processing. In the biomedical field, controlled protein adsorption is desirable for metallic implants [76–78]. Proteins are large complex macromolecules comprised of a three-dimensional structure of amino acids that exhibit a combination of hydrophobic, hydrophilic, polar, and apolar regions. These different regions within proteins permit adsorption to a wide range of surfaces [79], making them

extremely versatile adsorbates. Proteins can also unfold and form one or more spatial conformations through noncovalent interactions, typically hydrophobic and electrostatic with respect to a solid surface. Most proteins adsorb as monolayers, creating close-packed structures with surface mass density of 1-5 mg/m^2 [76].

In food processing, protein adsorption and subsequent fouling on equipment supports bacterial growth and can introduce contamination through the build-up and subsequent dislodging of deposits [80,81]. Fouling of heat exchangers used in pasteurization in the dairy industry is of great concern. Cows' milk is a complex biological fluid, consisting of numerous components. On average, the constituents by weight percent are: 87.5% water, 3.9% fat, 3.4% proteins, 4.8% lactose, and 0.8% minerals (ash). Of the proteins, casein represents 2.66% of the total 3.4% with whey proteins making up the rest, primarily 0.33% β-lactoglobulin (β-lg), 0.13% α-lactoglobulin (α-lg), and 0.04% serum albumin [82]. As alluded to previously, protein adsorption (including those in milk) can occur with coverage of less than 5 mg/m^2 below 70°C [80]. Milk fouling occurs at higher temperatures and can be grouped into two categories based on temperature. Protein-dominated fouling (Type A) occurs between 75 and 110°C, with mineral-dominated fouling (Type B) taking place above 110°C. Type A deposits are white in color, soft, and spongy (milk film) consisting of 50-70% proteins (mainly β-lg), 30-40% minerals, and 4-8% fat. Type B deposits are gray in color, hard, compact and granular (milk stone) consisting of 70-80% minerals (mainly calcium phosphate), 15-20% proteins, and 4-8% fat [81]. While exact mechanisms for milk fouling are still unclear, thermal denaturation of β-lg plays a crucial role. During denaturation, the β-lg protein unfolds by the reversible dissociation of the dimer into monomers and exposes the core containing reactive sulfhydrl groups. β-lg can then react with similar or other disulfide-bond-containing proteins (e.g., casein, α-lg) to form aggregates [83]. It remains unknown whether denatured proteins, aggregated proteins, or both are responsible for initial deposit formation [81]. β-lg and bovine serum albumin are often used in the study of protein adsorption on biomedical implants due to their availability and similar behavior to proteins found in human body fluids.

Through the use of these different organic media identified from the literature for their adsorptive affinity for Type 304 Stainless Steel and Nb, this study establishes that strong adsorption of the media to the metal surface is essential for the occurrence of a MC effect during the cutting of 'gummy' metals. This conclusion is supported by force measurements and chip

morphology. The objective of this study was not to provide an exhaustive investigation of each adsorbate-metal pairing under various cutting parameters, but it was to highlight the role and importance of adsorption in the MC effect and show a glimpse of the breadth of adsorbates available for exploitation, many of which are environmentally friendly.

3.4 Materials and Methods

3.4.1 Metals

For this study, the metals of interest were Type 304 Stainless Steel (SS304) and Nb. SS304 was chosen due to prior work showing it to possess sinuous flow [18] and its responsiveness to a large number of adsorbates identified in the literature as green corrosion inhibitors. Nb was chosen largely due to the severe nature of its 'gumminess.' It was also believed that the flow nature of Nb would exhibit a more pronounced response to changes in adsorbate concentration. Both metals were annealed and used in as-received condition. The SS304 and Nb were obtained from McMaster-Carr Supply Co. and Admat Inc., respectively. Tables 1-4 provide the supplier-provided chemical and mechanical properties of each. Grain structure of each is shown in **Fig. 3.1**.

Table 3.1. Composition of Type 304 Stainless Steel

Cr	Ni	Mn	Cu	Si	Mo	Co	W	N	V	Fe
18.220	8.080	1.390	0.470	0.350	0.310	0.185	0.084	0.084	0.070	Balance

Table 3.2. Mechanical Properties of Annealed Type 304 Stainless Steel

Tensile strength (MPa)	605
Yield strength (MPa)	270
Elongation (%)	52.9
Hardness (HB)	170

Table 3.3. Composition of Niobium

Ta	C	O	W	N	Zr	Si	Hf	Mo	Fe	Nb
0.0600	0.0080	0.0071	0.0045	0.0035	<0.0030	0.0020	<0.0020	0.0010	<0.0010	Balance

Table 3.4. Mechanical Properties of Niobium

Tensile strength (MPa)	302
Yield strength (MPa)	230
Elongation (%)	32.5

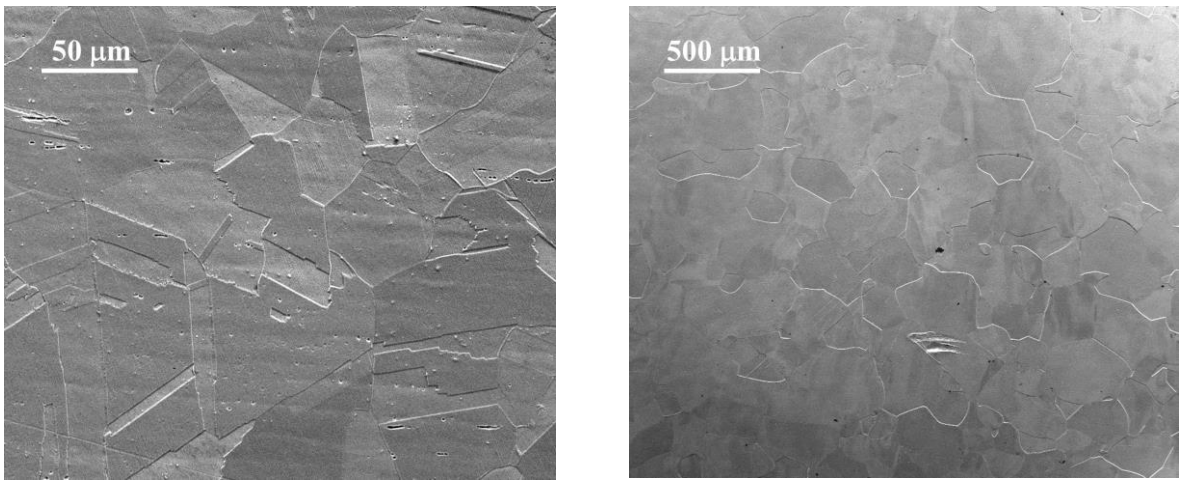

(a) (b)

Figure 3.1. Grain structure of (a) SS304 and (b) Nb.

3.4.2 Adsorbates

Of the several adsorbates identified in the literature showing effectiveness in corrosion inhibition in SS304, seven were randomly chosen for investigation into their efficacy to produce a MC effect in the cutting of SS304: *Thymus vulgaris* (thyme) [61], *Salvia lavandulifolia* (sage) [56], *Coriandrum sativum* (coriander) [59], *Foeniculum vulgare var. dulce* (sweet fennel) [57], *Capsicum annuum L.* (red pepper seed) [58], *Silybum marianum* (milk thistle) [60], and propolis [84]. According to the literature, some of the adsorbates had been extracted and prepared by the researchers from their native, local sources [58,60,84]. Since this was not possible in this study, adsorbates were selected from readily available commercial essential oils and dietary supplements. Although three of the seven adsorbates could not be identically matched to those in the literature, the extracts do belong to the same genus of plant. For completeness, Fourier-transform infrared spectroscopy (FTIR) was used to characterize each of the adsorbates. The spectra of the extracts are provided in Appendix C. None of the extracts were diluted for use. The common procedure for dilution of an essential oil is the use of a carrier oil, such as sweet almond oil. This would have introduced additional impurities – impurities which could unknowingly alter adsorption of the

extract. Although no references in the literature to these adsorbates as corrosion inhibitors were found with respect to Nb, all seven were also tried in the cutting of Nb as well. The lack of research into corrosion inhibitors for Nb is presumably due to Nb already being highly corrosion resistant for a wide variety of environments.

Other adsorbates used in the study were organic dyes, amoxicillin (25 mg/mL), and 2% cows' milk (approximately 3.3 g of protein per 100 g of milk). The dyes were manufactured by the Aldon Corp. The dyes included solutions of carbol fuchsin (0.29% w/v), carbol rose bengal (0.45% w/v), crystal violet (1% w/v), and methylene blue (1% w/v).

3.4.3 Experimental Setup

To investigate the effect these adsorbates have in the cutting of SS304 and Nb, a plane-strain (2D) cutting system model was employed (**Fig. 3.2**). The metal workpiece moves with velocity V_0 relative to a tool with rake angle α set at a depth of cut h_0 (undeformed chip thickness), with V_0 perpendicular to the cutting edge of the tool. Simple shear produces a deformed chip with thickness h_c with velocity V_c. The cutting apparatus consisted of a Tormach PCNC 770 instrumented with a piezoelectric dynamometer (Kistler 9254, natural frequency ~ 2 kHz). To image the cutting event, the metal workpiece was constrained behind a glass plate, preventing material side flow and providing a common focal plane. The workpiece was face milled to ensure workpiece and glass plate coincide and to introduce asperities on the workpiece surface to assist in digital image correlation (DIC). Cutting was observed *in situ* and recorded using a high-speed CMOS camera (Photron FASTCAM Mini WX100) coupled to an optical microscope (InfiniFlex DS 4x Tube). The cutting region is illuminated by a 120-W halogen lamp. The frame rate used was 500 fps. The imaging system provided a spatial resolution of 1.13 μm per pixel and recording area as large as 1536 × 1536 pixels. The resulting images were post-processed using DIC, enabling the quantitative analysis of displacement, velocity, strain rate, and strain fields. A large-area 3D optical profilometer (Zygo NewView 8300) was used to examine the surface quality of the cut surface. Each of the adsorbates were carefully applied to the metal, each dabbed on the surface with a cotton swab as to avoid excess application. Cutting was performed directly after adsorbate application, with the exception of the dyes and cows' milk which were permitted to dry for 10 min and 3 min, respectively.

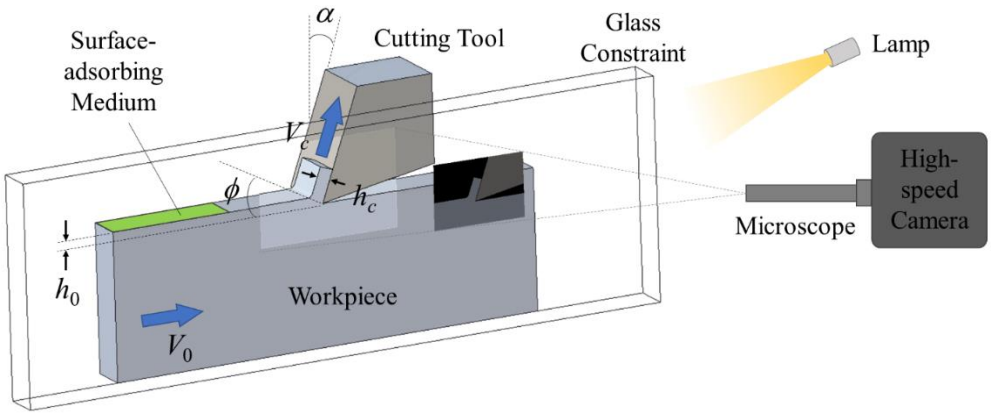

Figure 3.2. Schematic of experimental setup that permits *in situ* observation and high-resolution imaging of plane-strain cutting event. Adsorbed SA media can be applied on latter half of workpiece surface to record both conditions – with and without media – in same cut.

3.5 Results

3.5.1 Natural Extracts

All seven of the natural extracts resulted in a MC effect in SS304. For the testing of each extract, one-third of the workpiece surface was left uncoated, one-third coated with ink, and one-third coated with the extract. The ink serves as a convenient 'standard' based on its use in prior work, permitting comparison and assessment of the relative effectiveness of the extract. A specific force trace (Force/h_0) for one of the extracts is provided as **Fig. 3.3a** for a rake angle α of 20°, cutting speed V_0 of 2 mm/s, and undeformed chip thickness h_0 of 100 μm. All force traces are provided in Appendix D. The MC effect resulted in a force reduction of approximately 35% (from maximum force). All extracts exhibit the same behavior and force magnitudes for these cutting parameters. **Figure 3.3b** provides a summary of the cutting forces with and without application of the various extracts. On comparison, there is little deviation in force magnitudes for the various extracts. Force fluctuations are greatest in the region without media as evidenced by the higher standard deviations. The extracts result in a very steady force. In addition, the force does not deviate from the region with ink to the region with the natural extract.

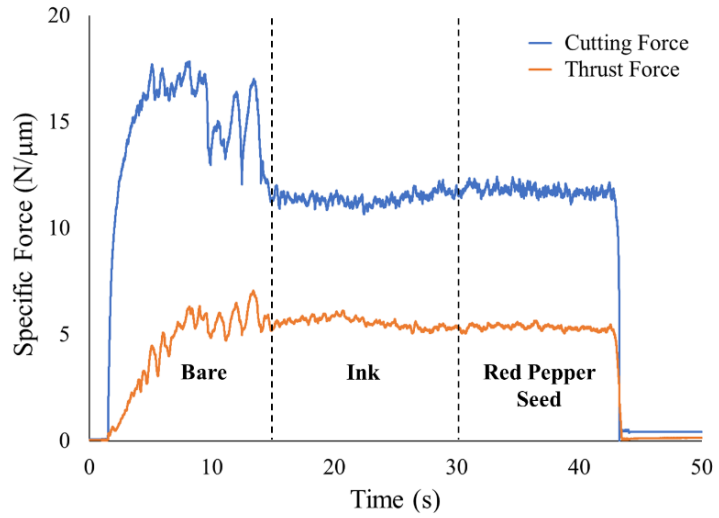

(a)

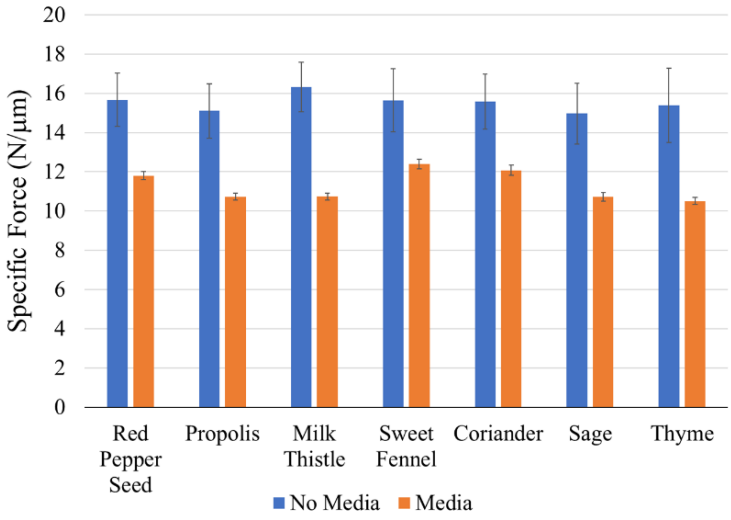

(b)

Figure 3.3. (a) Specific force traces for red pepper seed showing characteristic force reductions associated with the MC effect. One-third of the workpiece was left bare (uncoated), one-third coated with ink (a known SA media that engenders the MC effect) for comparison, and one-third coated with the natural extract. (b) Summary of specific cutting force magnitudes for the various natural extracts. $\alpha = 20°$, $V_0 = 2$ mm/s, $h_0 = 100$ µm.

Unlike in SS304, none of the seven natural extracts produced a MC effect in Nb. There was no discernable change in force, chip morphology, or workpiece surface quality. A plot containing the force traces for all seven natural extracts is provided as **Fig. 3.4**. The only drop in force observed is due to the natural behavior of folding in Nb; once a pile of folds becomes

sufficiently large, it will fracture and the pile-up event will continue. **Fig. 3.5** is a close-up view of the resulting Nb chip when cutting with sweet fennel, showing this sequence of pile-up and fracture.

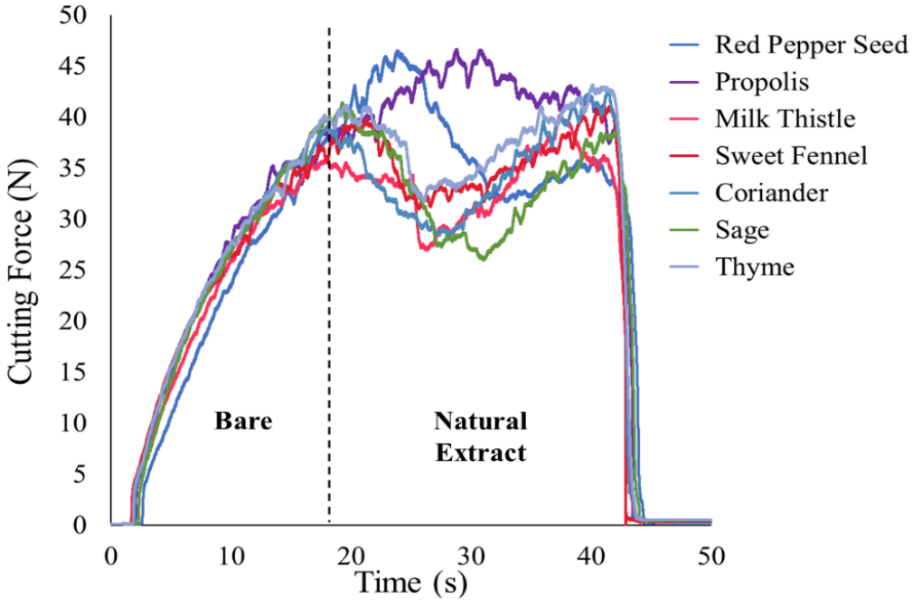

Figure 3.4. Specific cutting force traces for Nb with half the surface left bare (uncoated) and the other half coated with a natural extract. No significant reduction in force occurs for any of the natural extracts. Force undulation is characteristic of Nb. $\alpha = 10°$, $h_0 = 50$ μm, $V_0 = 2$ mm/s.

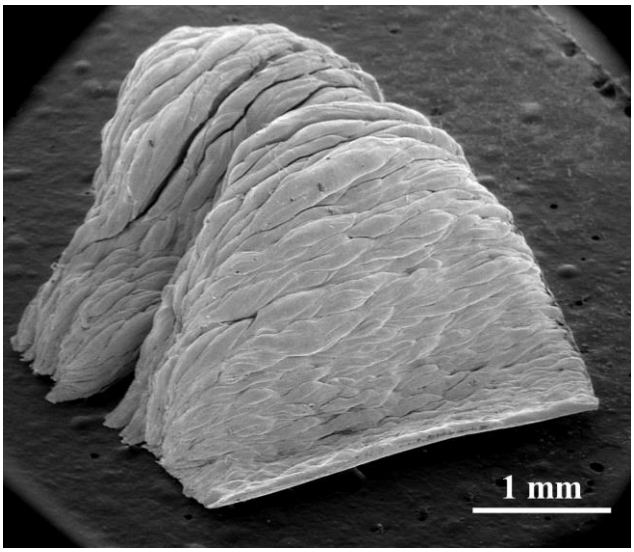

Figure 3.5. Resulting chip from the cutting of Nb, half-bare (uncoated) and half coated with sweet fennel. Pile-up of folds is characteristic for Nb. Fracture will intermittently disrupt pile-up event.

3.5.2 Dyes

All four dye solutions caused a MC effect in SS304. The same testing condition was used as for the natural extracts, one-third of the workpiece surface was left uncoated, one-third coated with ink, and one-third coated with the dye. The force traces are provided in **Figs. 3.6a,b**. As in the case of the natural extracts, the MC effect resulted in an approximate 35% force reduction.

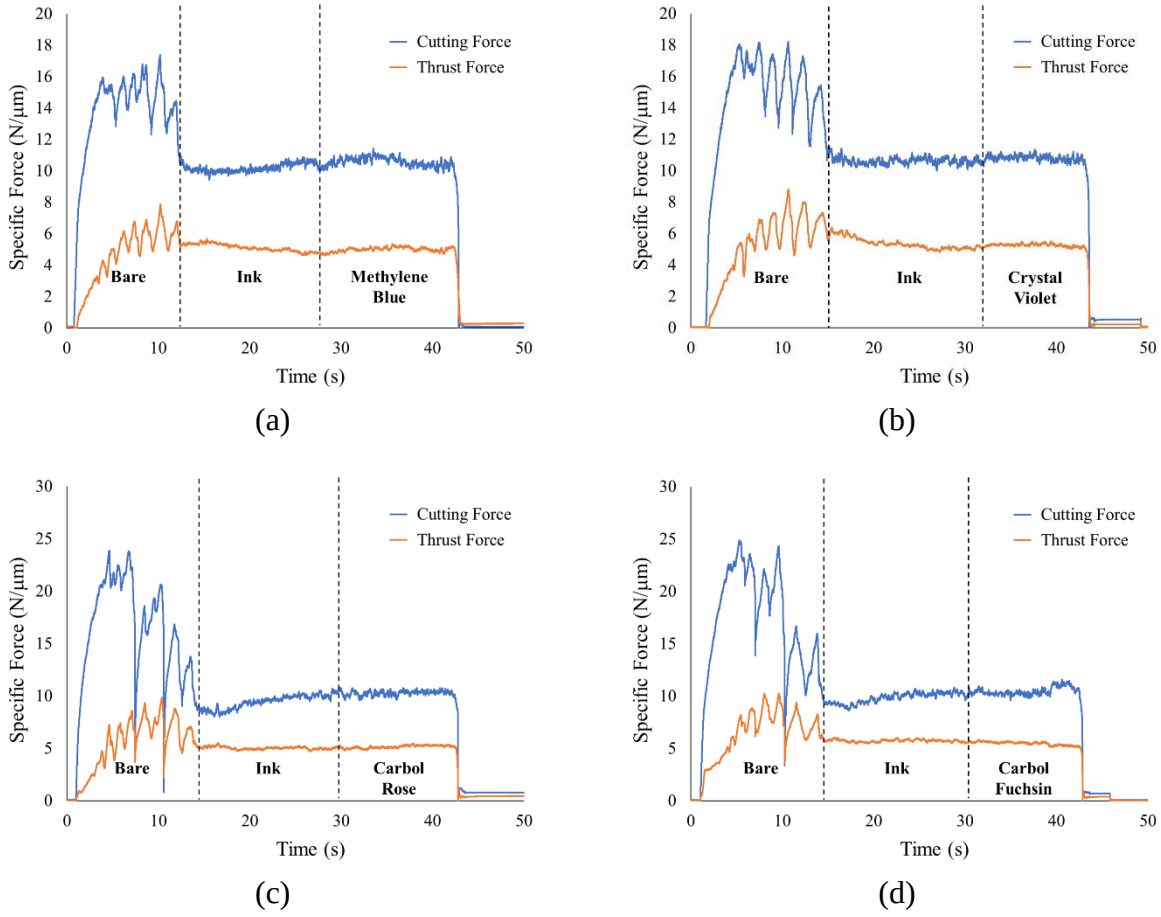

Figure 3.6. Specific force traces for various aqueous dye solutions showing characteristic force reductions associated with the MC effect. One-third of the workpiece was left bare (uncoated), one-third coated with ink (a known SA media that engenders the MC effect) for comparison, and one-third coated with the dye. α = 20°, h_0 = 100 μm, V_0 = 2 mm/s.

Upon application of the dyes to the Nb, each dye was permitted to remain on the surface for 10 minutes prior to cutting. Of the four dyes, only methylene blue yielded a MC effect in Nb. Force traces are provided in **Fig. 3.7**. For methylene blue, a force reduction of approximately 60%

was realized for a rake angle α of 10°, undeformed chip thickness h_0 of 50 μm, and cutting speed V_0 of 2 mm/s.

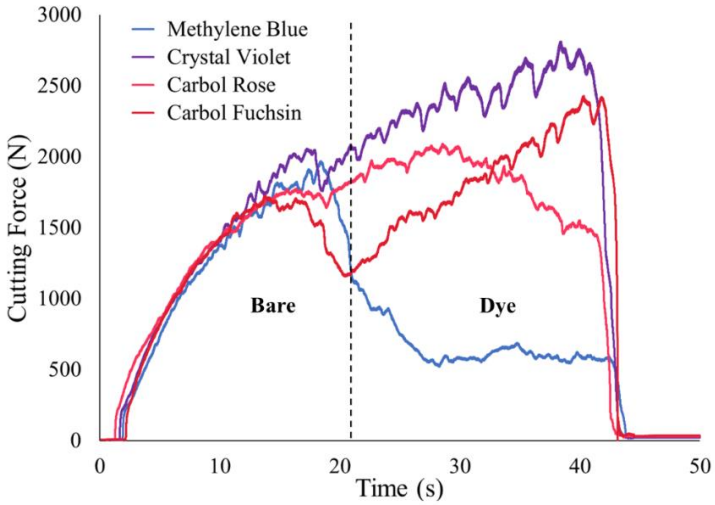

Figure 3.7. Cutting force traces for various aqueous dye solutions applied to Nb. Only the methylene blue dye resulted in the characteristic force reduction associated with the MC effect. α = 10°, h_0 = 50 μm, V_0 = 2 mm/s.

3.5.3 Amoxicillin

Amoxicillin gave rise to a MC effect in both SS304 and Nb. Although the literature review revealed the use of antibacterial drugs on SS304 for corrosion inhibition [69,85], no use of it in conjunction with Nb was found. The amoxicillin resulted in a force reduction of approximately 35% for SS304 and 60% for Nb (**Figs. 3.8a,b**).

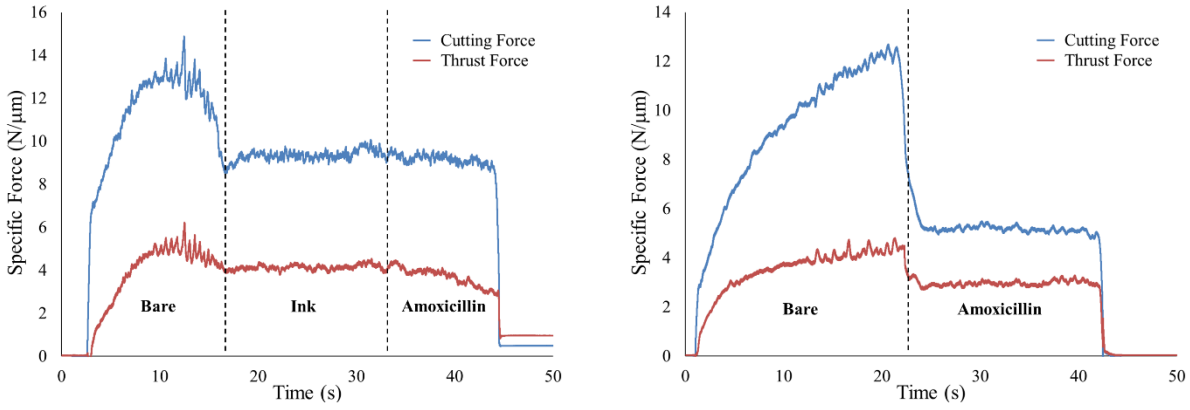

(a) (b)

Figure 3.8. Specific force traces for the cutting of (a) SS304 and (b) Nb with amoxicillin. α = 20°, h_0 = 100 μm, V_0 = 2 mm/s.

3.5.4 Cows' Milk

Cow's milk generated a MC effect in both SS304 and Nb. Upon application of the milk, the resulting film was permitted to dry for approximately 3 minutes prior to cutting the metal. Again, force reductions were the same as previously used media, providing 35% and 60% declines for SS304 and Nb, respectively (**Figs. 3.9a,b**).

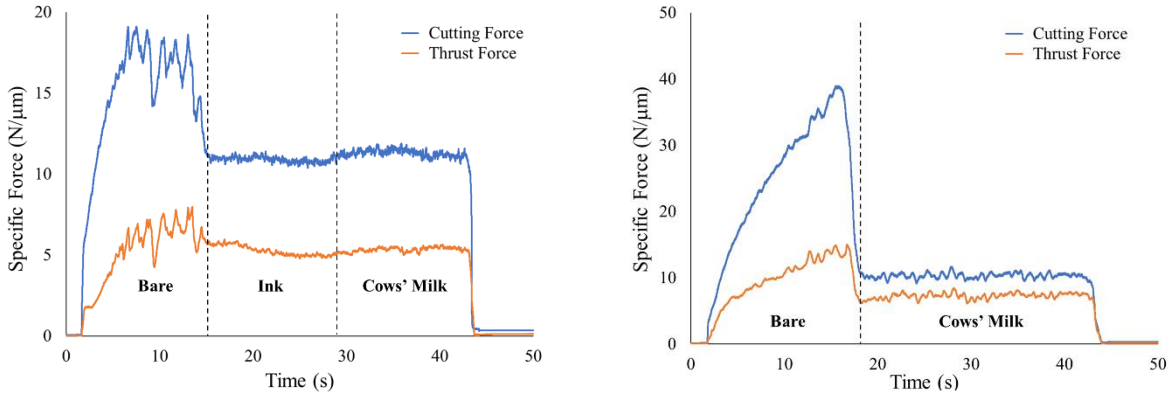

(a) (b)

Figure 3.9. Specific force traces for the cutting of (a) SS304 (α = 20°, h_0 = 100 μm, V_0 = 2 mm/s) and (b) Nb with cows' milk (α = 10°, h_0 = 50 μm, V_0 = 2 mm/s).

3.5.5 Chip Morphology

While force traces demonstrate the impact an adsorbate has in transitioning sinuous to segmented flow, it is also beneficial to examine the resulting chip morphology for the two flow modes. **Fig. 3.10a** is a prototypical chip obtained during the cutting of SS304 that shows this transition from sinuous to segmented flow. The most prominent difference in the use with and without media is the reduction in chip thickness. **Fig. 3.10b** is a prototypical chip for Nb. The bare (no media) region of the chip is a pile-up of folds. When the media is encountered, the chip thickness substantially decreases and becomes constant.

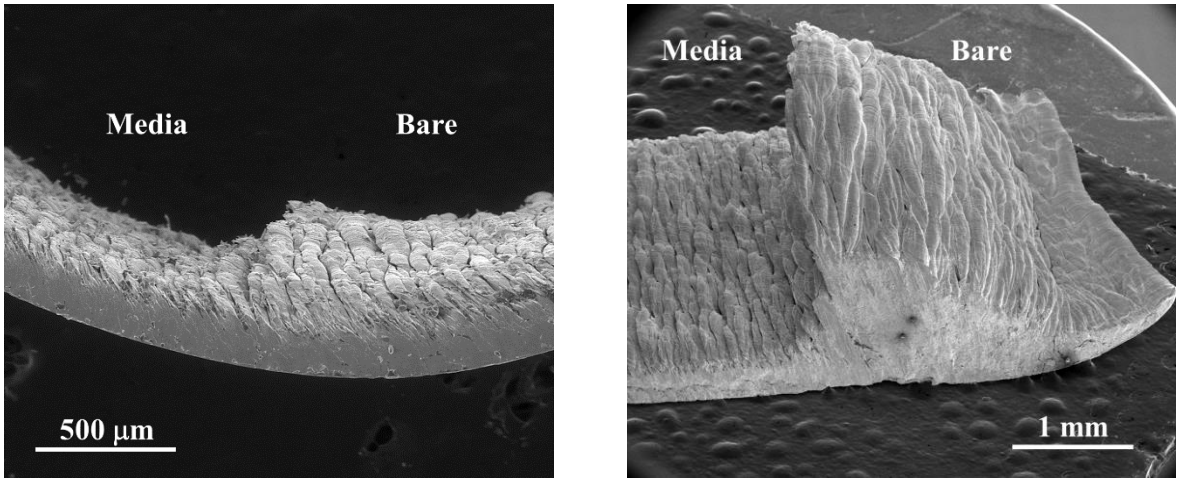

(a) (b)

Figure 3.10. (a) SS304 chip displaying the transition between sinuous and segmented flow characterized by a reduction in chip thickness. (b) Nb chip transitions from a severe fold pile-up to one that is of constant thickness.

3.5.6 Flow Characterization

Using sequences of images recorded through high-speed imaging, direct image correlation (DIC) provides additional insight into the nature of sinuous flow and the MC effect in SS304 and Nb. **Fig. 3.11a** and **3.11b** are images of chip formation in SS304 with overlay of strain fields with streaklines for sinuous and segmented flow, respectively. As previously noted from chip morphology (**Fig. 3.10a**), an approximate 15% reduction in chip thickness occurs. This change in chip thickness is most apparent upon examination of the shear plane (dotted line), as it noticeably extends more forward of the tool in the case of sinuous flow. While the folding exhibited by the streaklines for sinuous flow (**Fig. 3.11a**) is not as severe as has been noted in annealed Cu and Al, there is a definite change when the flow transitions to segmented (**Fig. 3.11b**). The flow becomes more serrated in appearance. This is the characteristic flow of segmentation.

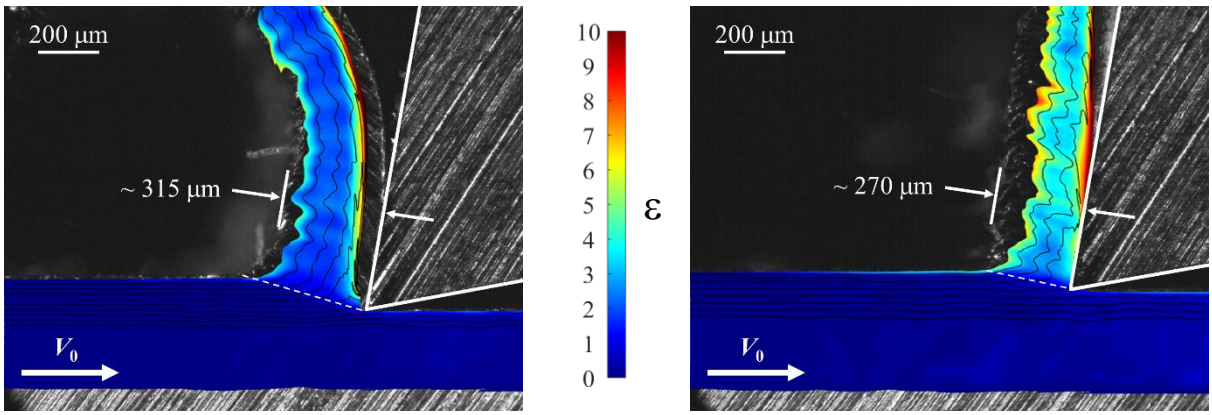

(a) (b)

Figure 3.11. In situ high-speed images of (a) sinuous and (b) segmented flow in SS304 with overlay of strain fields and streaklines. The most notable difference in the two types of flow is the reduction in chip thickness. Streaklines become serrated in appearance. $\alpha = 10°$, $h_0 = 100$ µm, $V_0 = 2$ mm/s.

Figs. 3.12a and **3.12b** are images of chip formation in Nb for sinuous and segmented flow, respectively. In the case of sinuous flow, the streaklines are quite jagged with a high frequency. This is the result of large amplitude folding. In contrast, for segmented flow (**Fig. 3.12b**), the flow is more periodic and the frequency is significantly less. The periodicity matches the segmentation along the free surface of the chip. For both SS304 and Nb, DIC reveals that sinuous flow often results in material stagnation (dead metal zone) near the tool tip, as evidenced by flow diversion from along the rake face.

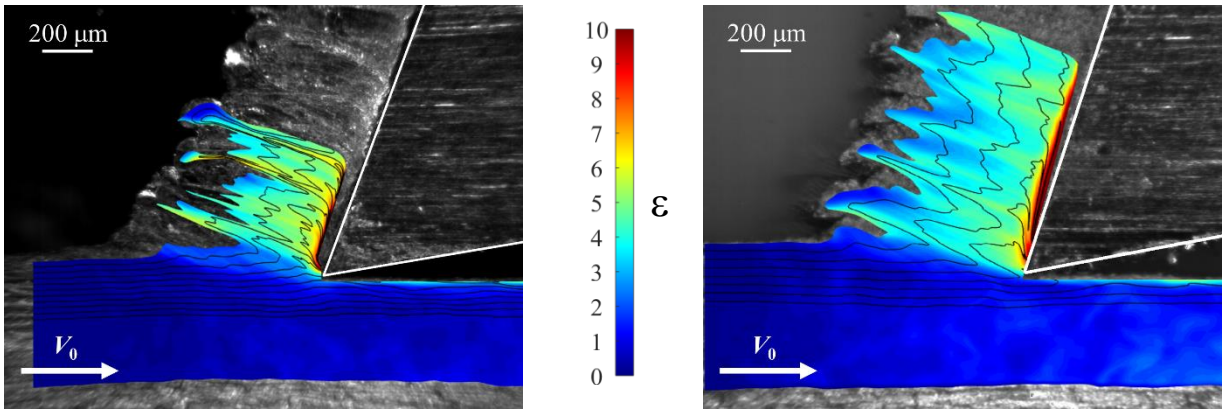

(a) (b)

Figure 3.12. *In situ* high-speed images of (a) sinuous and (b) segmented flow in Nb with overlay of strain fields and streaklines. Comparing sinuous to segmented flow, individual streakline frequency decreases and becomes more periodic. $\alpha = 20°$, $h_0 = 100$ µm, $V_0 = 3$ mm/s.

3.5.7 Surface Quality

In addition to a reduction in force and change in chip morphology, the application of SA media is accompanied by improved quality of the cut surface of the workpiece. **Fig. 3.13** is the prototypical surface quality of SS304 when cut without and with SA media, respectively (α = 20°, h_0 =100 μm, V_0 = 2 mm/s). For the case without SA media, the average mean height *Sa* is 10.84 μm for the sampled surface. Cutting with SA media results in a markedly improved surface quality, having a *Sa* six times smaller, 1.68 μm. For the case without SA media, surface undulations are apparent.

Similarly, a dramatic improvement in surface quality occurs in the case of Nb when using SA media. **Fig. 3.14** is the prototypical surface quality of Nb showing the transition when cutting with media (α = 20°, h_0 =100 μm, V_0 = 2 mm/s). The average mean height *Sa* is 19.98 μm and 3.72 μm with and without media, respectively – a five-fold improvement in surface quality. Significant material pullout occurs in the area without media.

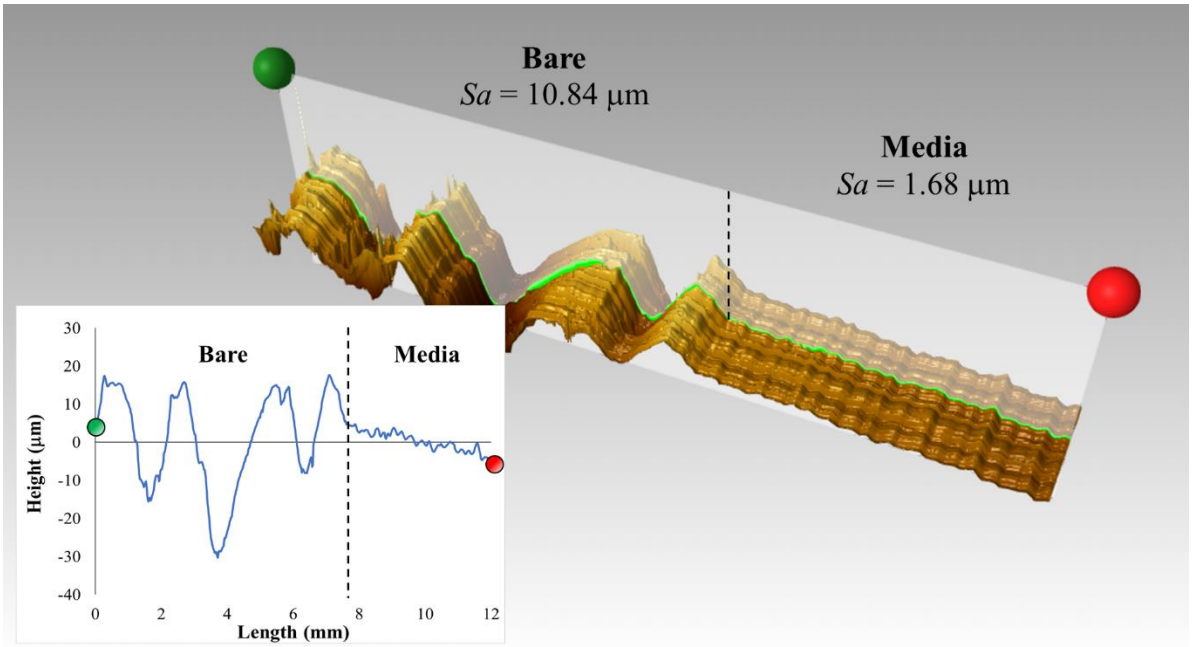

Figure 3.13. Surface topography and profile for SS304 cut without and with SA media. The surface of SS304 transitions from large surface undulations (without media) to one with little fluctuation (with media) – a six-fold improvement in surface roughness. α = 20°, h_0 =100 μm, V_0 = 2 mm/s.

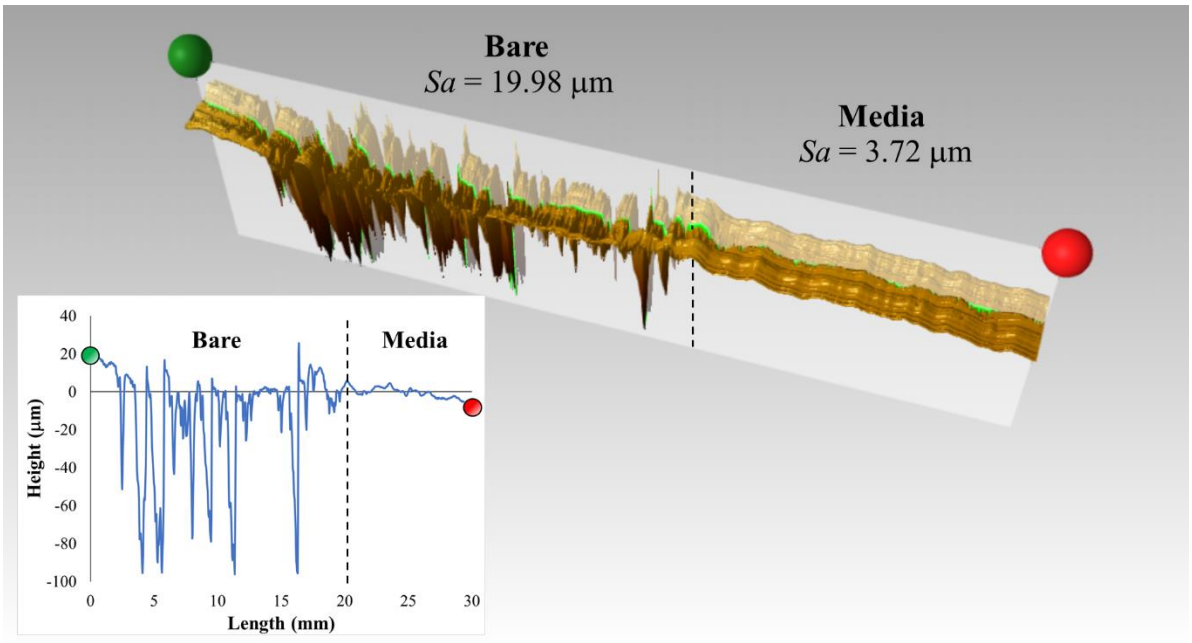

Figure 3.14. Surface topography and profile for Nb cut without and with SA media. The surface of Nb transitions from deep valleys, indicative of material pull-out (without media), to one with no severe cracks or tears (with media) – a five-fold improvement in surface roughness. α = 20°, h_0 =100 μm, V_0 = 2 mm/s.

3.5.8 Effect of Adsorbate Concentration

In this experiment, aqueous solutions of methylene blue with weight/volume concentrations between 0.01 and 1.0% were applied along the entire length of the Nb workpiece surface. The methylene blue solution was permitted to reside on the surface for 10 minutes prior to cutting. The same series of tests performed using a dwell time of 30 minutes yielded the same outcomes. **Fig. 3.15** are the resulting cutting force traces for different concentrations during the cutting of Nb for α = 10° at V_0 = 2 mm/s for an undeformed chip thickness h_0 = 50 μm. As concentration increases, cutting force decreases. At a concentration of 0.01%, the force trace matches the case when no media has been applied. The shape of the force traces changes as concentration increases – concavity switches from downward to upward. The slope of the traces become increasingly shallow until the forces level off at 1.0%.

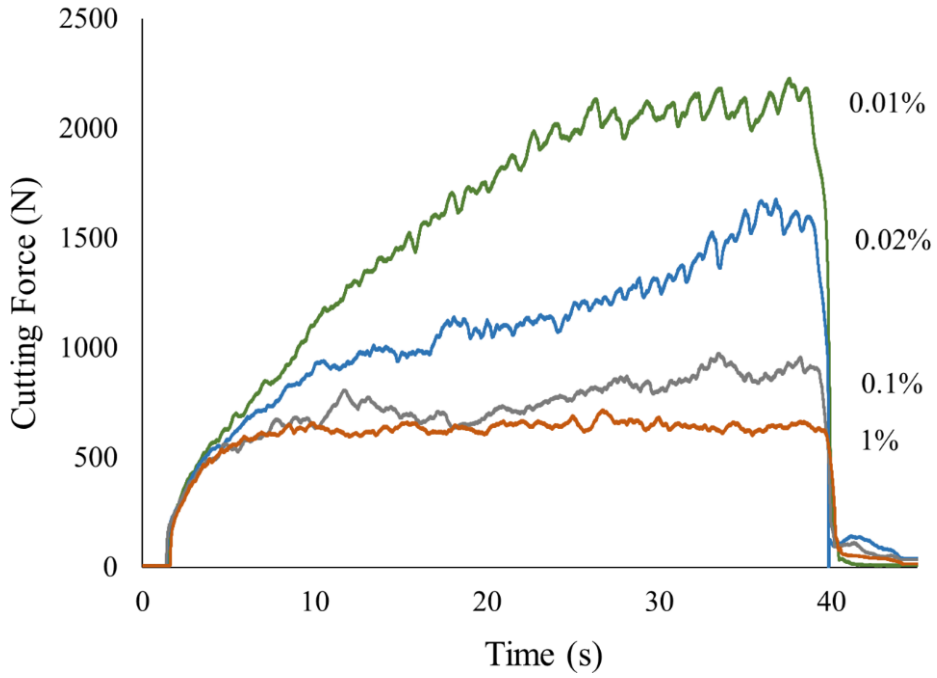

Figure 3.15. Force traces obtained for the cutting of Nb with application of methylene blue dye in concentrations of 0.01, 0.02, 0.1, and 1%. As concentration increases, the force decreases until it levels off at a concentration of 1%. $\alpha = 10°$, $h_0 = 50$ μm, $V_0 = 2$ mm/s.

Chip morphology provides additional insight into the effect of adsorbate concentration on the MC effect. For a methylene blue concentration of 0.01%, chip morphology is consistent with having applied no adsorbate at all (**Fig. 3.16a**). The chip is simply a pile-up of overlapping folds, just like the morphology previously shown in **Fig. 10b**. For a concentration of 0.02%, the pile-up event is not nearly as aggressive – slowly building during the cut, resulting in a longer chip (**Fig. 3.16b**). For a concentration of 0.1%, the initial portion of the chip is relatively constant in thickness with an occasional fold being larger than neighboring folds. Toward the latter half of the chip, a pile-up event occurs (**Fig. 3.16c**). For a concentration of 1%, the thickness of the chip is constant and pile-up events are absent (**Fig. 3.16d**).

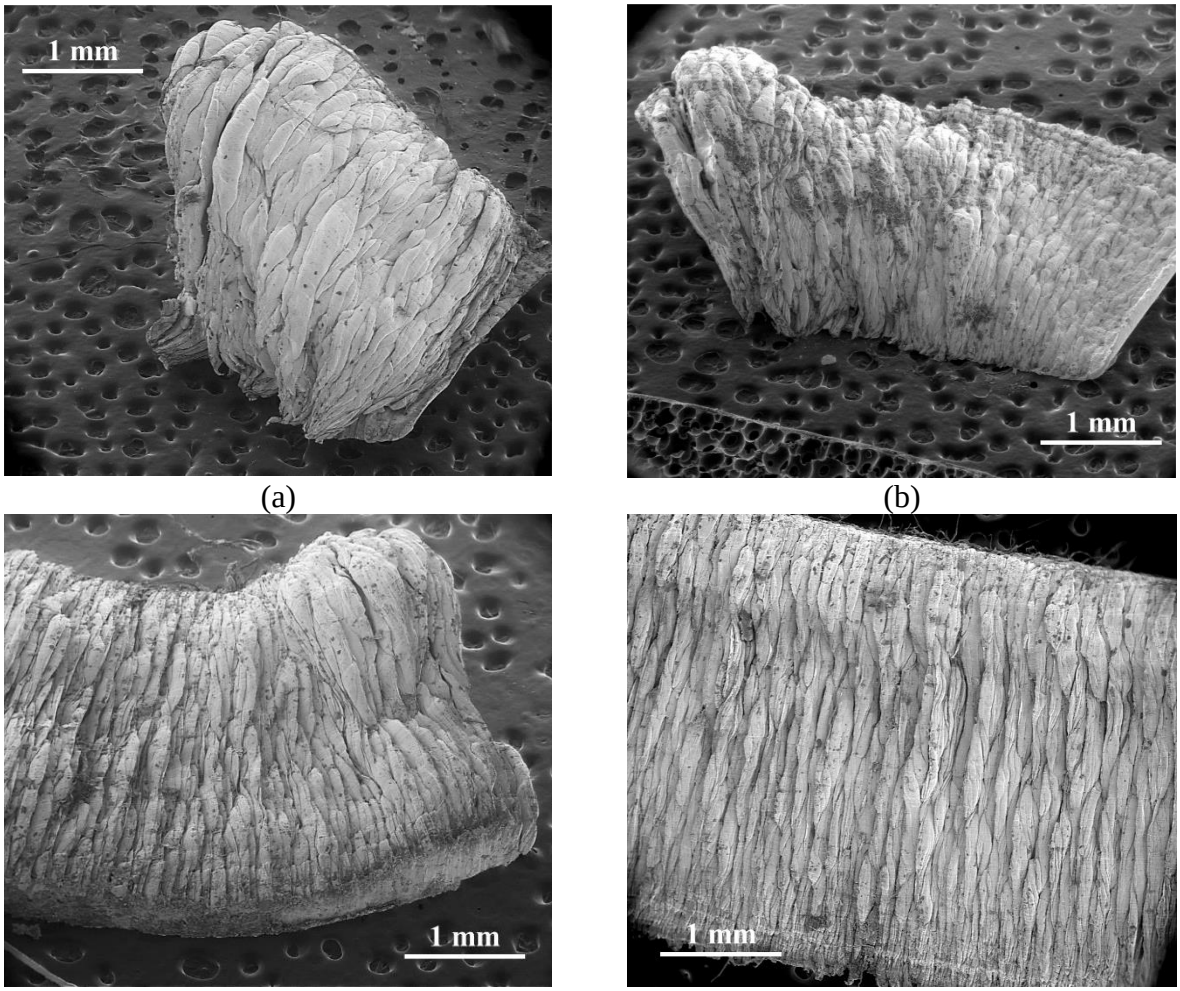

(a) (b)

(c) (d)

Figure 3.16. (a) Chip from cutting of Nb with 0.01% methylene blue dye concentration. Chip is large pile-up of folds. (b) Chip from cutting with 0.02% dye concentration. A slower progression of fold pile-up is apparent. (c) Chip for cutting with 0.1% dye concentration. Chip is largely void of pile-up events until toward the end of the cut. (d) Chip for cutting with 1% dye concentration. Chip thickness is constant, with pile-up events absent.

3.5.9 Effect of Oxide Layer Thickness

The corrosion resistance of SS304 and Nb is derived from their native oxide coatings. It is the oxide coating to which the adsorbate interacts. Therefore, it is appropriate to probe the effect of oxide layer thickness on the MC effect. Increasing the thickness of the oxide layer is known to improve adsorption, often attributed to the oxide being amorphous and thereby increasing its surface energy [86,87]. While the relationship between adsorption and oxide layer thickness is understood, the impact of oxide layer thickness on the MC effect is not. For a range of voltages, anodic oxidation was employed to increase the oxide thickness on several polished Nb samples by

using an aqueous electrolytic solution of TSP-PF (an environmentally friendly detergent) and distilled water at a concentration of 5 g/L. Stainless steel foil served as the cathode. Ellipsometry was used to determine the oxide layer thickness for several of the Nb samples. Upon plotting thickness against voltage, a linear relationship yielded an anodizing ratio of 2.5 nm/V (**Fig. 3.17**).

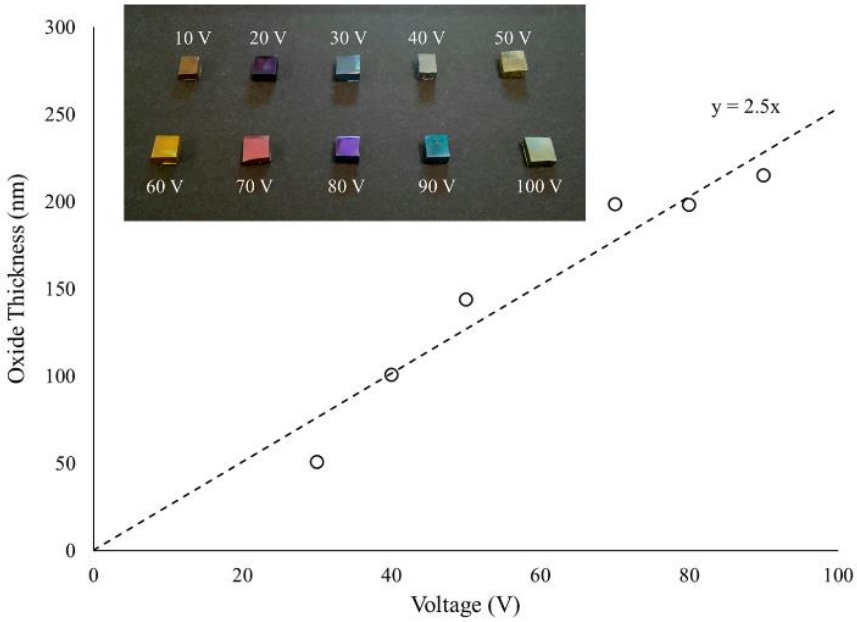

Figure 3.17. Relationship between voltage and oxide thickness of Nb anodized in solution (5 g/L) of TSP-PF detergent and distilled water. Oxide layer thickness obtained through ellipsometry.

Several experiments were performed on a Nb workpiece under different conditions of oxidation. The first series of experiments were conducted to determine the effect of oxide layer thickness on the general behavior of Nb when cut in the presence of no lubricant or SA media. The workpiece was anodized for a range of voltages from 10 to 100 V. **Fig. 3.18** contains two cutting force traces ($\alpha = 20°$, $h_0 = 100$ μm, $V_0 = 2$ mm/s), one for an anodization at 50 V (~ 125 nm oxide thickness) and the other with just the native oxide layer (~ 5 nm in thickness [88]). Both force traces exhibit the steady climbing force that occurs during fold pile-up. However, as previously mentioned, pile-up events will fracture and initiate new pile-up events, resulting in an undulating force. The workpiece with the thicker oxide coating displayed a different behavior; instead of an interruption in the pile-up event, the pile-up remains continuous with the chip slowly becoming

thicker. This attribute is reflected in the force trace as a linear rise. For the same cutting parameters, all oxide coatings by anodization resulted in identical behavior.

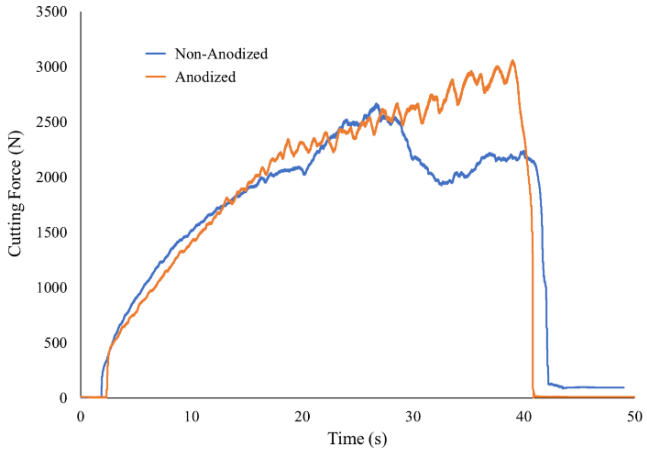

Figure 3.18. Comparison of cutting force for Nb with native oxide coating and approximate 125-nm oxide coating. The force undulates in the case of the native oxide coating, while the thicker oxide layer results in a steady increase. $\alpha = 20°$, $h_0 = 100$ μm, $V_0 = 2$ mm/s.

To determine the effect of oxide layer thickness on the MC effect, the workpiece was anodized at 100 V (~ 250 nm oxide thickness) and the latter half of the work piece was coated with cows' milk. **Fig. 3.19** is the resulting cutting and thrust force traces ($\alpha = 20°$, $h_0 = 100$ μm, $V_0 = 2$ mm/s). The same characteristic force reduction occurs for the thick oxide coating as previously noted for the native oxide coating.

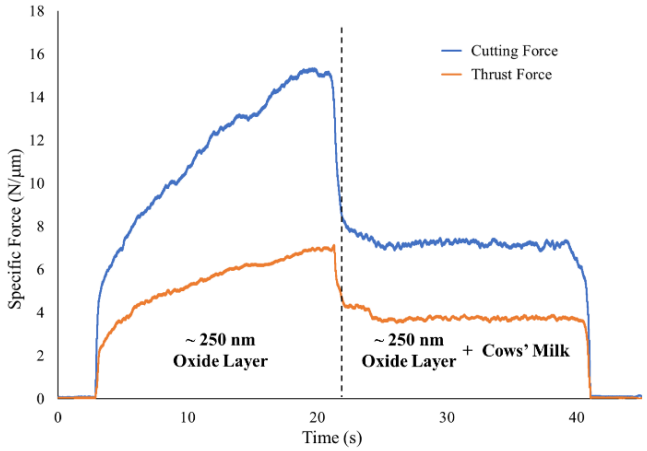

Figure 3.19. Specific force traces for cutting of Nb with an approximate 250-nm oxide coating with and without SA media. The characteristic force reduction that accompanies the MC effect is present and on the same order as previously noted for Nb with its native oxide coating. $\alpha = 20°$, $h_0 = 100$ μm, $V_0 = 2$ mm/s.

Lastly, to ascertain if the force reduction via the MC effect is equivalent for the native oxide layer and a thicker oxide layer, half the workpiece was anodized at 70V (~ 175 nm oxide thickness) and the remainder was left as the native oxide layer. Milk was applied over the entire surface. **Fig. 3.20** is the resulting cutting and force traces (α = 20°, h_0 = 100 μm, V_0 = 2 mm/s). The magnitudes of the forces (~ 7 N/μm) are constant throughout the cut, same as observed in **Fig. 3.19** when cutting with cows' milk with a ~ 250-nm oxide layer. The oxide layer thickness has no effect on the degree of force reduction resulting from the MC effect.

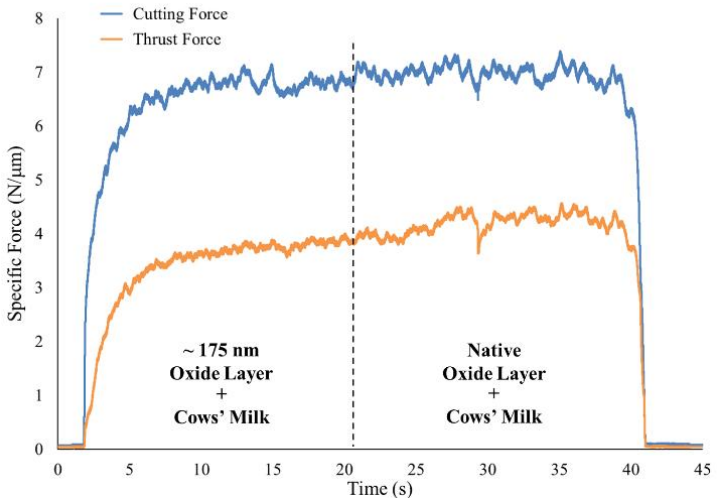

Figure 3.20. Comparison of specific forces for cutting of Nb with cows' milk with half the workpiece with native oxide coating and the other half with approximate 175-nm oxide coating. The force remains steady throughout the cut, exhibiting no changes in force between the two oxide thickness conditions. α = 20°, h_0 = 100 μm, V_0 = 2 mm/s.

3.6 Discussion

Since the adsorbates identified through the literature exhibited a mechanochemical effect during cutting for their respective adsorbate-metal pairings, it is concluded that adsorption is essential to the MC effect. This assertion is further supported by the experiments concerning changes in concentration of methylene blue solution in the cutting of Nb. Reducing the concentration of adsorbate limits the MC effect. Additionally, since media was used that exhibit both physical and/or chemical adsorption (i.e., *Salvia lavandulifolia* [56], *Silybum marianum* [60]) and proved effective in engendering the MC effect, adsorption type does not appear to be of importance to the effect. Furthermore, while the natural extracts produced the MC effect in SS304, they had no apparent effect in Nb. This highlights the nature of adsorption. Compatibility must

exist between adsorbate and adsorbent. In addition, the high corrosion resistance of Nb suggests fewer adsorbates are available – corrosion inhibitors compete for the same active sites as corrosive agents.

As corrosion inhibitors, certain natural extracts have higher inhibition efficiencies than other extracts. However, in the case of generating a MC effect, such a distinction is not apparent; there is no difference in force reduction for different extracts. This supports the hypothesis that a ductile-to-brittle transition is responsible for the observed behavior. The high-stress concentrating notches created through folding result in fracture events in the presence of an adsorbate. Furthermore, the dyes, amoxicillin, and cows' milk had no greater or less of an effect than the extracts, which provides additional support for this premise. However, the experiment in varying the concentration of methylene blue dye does suggest that adsorption must be 'sufficient' to consistently trigger the MC effect. Otherwise, the ductile-to-brittle transition either does not occur or occurs only partially. A partial MC effect may be explained by the fold-generated notches having a range of different stress concentrations; some notches require little additional stress to initiate a crack, while others may necessitate considerably more. Attaining a given stress threshold for a notch may additionally be influenced by adsorbate affinity for a given region of higher surface energy and/or intermolecular cohesion between adsorbate molecules.

With many of the plant extracts being oils, it is pertinent to ask whether the reduction in force attributed to the MC effect is simply due to lubrication. However, there are two indicators that refute the force reduction being a lubrication effect. First, on comparison of those regions marked with ink to those with the applied extract, there is no change in the ratio of thrust force to cutting force. Since the ink is permitted to dry prior to cutting, it cannot flow into the tool-chip interface and remains on the free surface, unable to provide lubrication at the tool contact. Although the extracts do not dry, the equitable force reductions to those of the ink suggest that they are behaving in the same manner. Second, liberal application of the extracts, permitting intrusion into the tool-chip interface, will in fact result in a greater reduction in thrust force – indicative of a lubrication effect. **Fig. 3.21** is a comparison of red pepper seed oil (a) with careful application and (b) with liberal application. As anticipated, a greater reduction in thrust force is readily noticeable in the case with liberal application; the change in cutting force is less significant.

While academically important to isolate the MC effect from a lubrication effect, in application, an adsorbate that offers lubrication in addition to the MC effect is more desirable over one that does not. One that provides additional corrosion inhibition is even better.

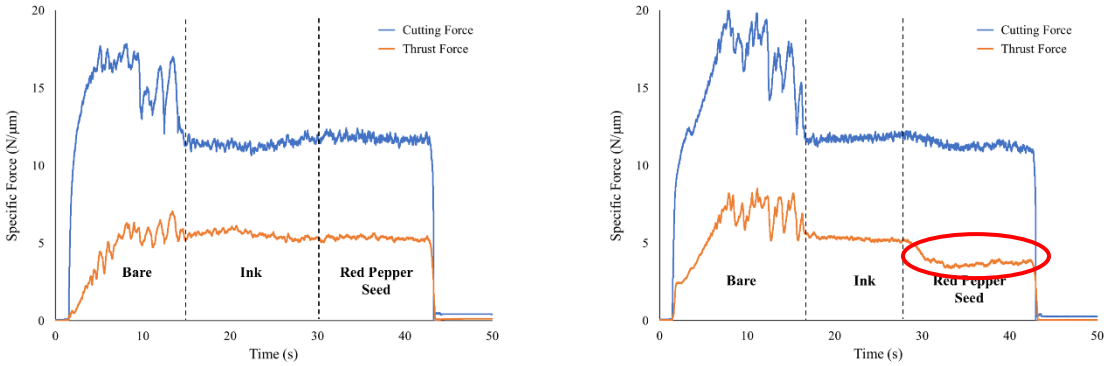

Figure 3.21. Comparison between specific forces for cutting of SS304 with (a) careful application of red pepper seed oil and (b) liberal application of the oil. A drop in the thrust force is noted when the oil if applied liberally, suggesting a lubrication effect in addition to the MC effect. $\alpha = 20°$, $h_0 = 100$ μm, $V_0 = 2$ mm/s.

Although adsorption appears to be key for both corrosion inhibition and the MC effect, it should not be misconstrued that an adsorbate that serves as an effective SA media in cutting will be an effective corrosion inhibitor. The requisite conditions for a corrosion inhibitor are greater than those imposed for the MC effect; namely, the interaction of the inhibitor with the corrosive agent must be considered. However, the cutting of a 'gummy' metal as a first step in identifying potential corrosion inhibitors may have some merit nonetheless, as a cutting experiment is comparatively easier to setup and uses no caustic/corrosive chemicals as does an electrochemical cell. Application of a media in the cutting of a 'gummy' metal can reveal whether the media adsorbs and even provide a relative rate of adsorption, as some media must be present on the surface for a certain time period before the MC effect occurs, e.g., methylene blue dye.

One important distinction exists between the media used in this study (i.e., natural extracts, dyes, etc.) and the media used in previous work concerning the MC effect in the cutting of 'gummy' metals – all are liquid in form. Unlike media used for adhesion and marking, these natural media can more easily be applied during a machining operation. Many could potentially be either added to an appropriate cutting fluid or be used as the cutting fluid. In certain regions of the world,

disposal of native biowaste from vegetation processing can be problematic. An additional use for excess plant material would be welcomed in such regions.

Experiments with increasing oxide layer thickness in Nb reveal that it has no influence on the MC effect. The ductile-to-brittle transition still occurs – with sinuous flow becoming segmented flow – and force reductions remain the same regardless of oxide layer thickness. While increasing the oxide layer thickness might lead one to believe that a reduction in adsorption-induced surface stress might be experienced at the metal-oxide interface, the anodic oxide layer is relatively porous, typically increasing surface energy and hence adsorption.

An environmental factor often varied in corrosion inhibition studies to determine its effect is temperature. Further research is needed to elucidate the impact of temperature on adsorbate-metal interaction during chip formation and the MC effect. It has significant importance in terms of application, particularly regarding cutting/coolant fluid formulation and high-speed machining. Presumably, those adsorbates that enjoy higher boiling points would remain more effective over a wider range of temperatures. Also, based on the literature on green corrosion inhibitors, adsorbates that chemically adsorb should prove superior at higher temperatures to those that only physically adsorb.

3.7 Conclusions

This study demonstrates a wide variety of media is available to combat the challenge in cutting ‘gummy’ metals. Furthermore, many are eco-friendly, liquid in form, lubricious, and corrosion inhibiting – all extremely desirable for a cutting fluid. The effectiveness of SA media in generating a MC effect is derived from their adsorption strength. Since concentration affects adsorption, it was shown that concentration can also impact the efficacy of the MC effect. Further study is needed to determine the extent to which temperature plays a role.

4. EXPLORING THE MECHANOCHEMICAL EFFECT ON 'GUMMY' METALS AT HIGH CUTTING SPEEDS

(This chapter has been prepared for consideration for publication. Co-authors: Mojib Saei, Anirudh Udupa and Srinivasan Chandrasekar.)

4.1 Abstract

Soft and/or highly strain-hardening metals often exhibit poor machinability, plagued by thick chip formation, high cutting forces, and residual defects on the workpiece surface, e.g., cracks, tears, pullouts. The behavior of these metals during cutting has earned them the reputation of being 'gummy.' Their 'gummy' nature is the result of sinuous flow – an unsteady, highly redundant mode of plastic deformation. *In situ* imaging and digital image correlation have revealed sinuous flow begins as a plastic instability on the workpiece surface just ahead of the advancing tool. What begins as a buckling event quickly develops into a fold as the metal traverses the cutting shear zone. The process of surface buckling and fold formation repeats, creating a highly strained chip consisting of a collection of folds. While sinuous flow adversely affects machinability, it has been discovered that it can be effectively ameliorated through the use of a mechanochemical effect – change in the deformation behavior of a material due to the presence of a chemical medium, more specifically one that adsorbs. The unfavorable sinuous flow mode transitions to one that is energetically more favorable – segmented flow – through a ductile-to-brittle transition. Until now, research into sinuous flow and the mechanochemical effect has been restricted to low-speed linear cutting (< 1 m/s) so as to examine the underlying mechanics in the absence of thermal effects. In this study, we show that sinuous flow extends into higher cutting speeds (1-5 m/s) as well, and the proper selection of a surface-adsorbing medium can greatly increase machinability, resulting in lower cutting forces and improved workpiece surface finish.

4.2 Introduction

A 1916 article in *Popular Science Monthly* recounts the tale of discovering the effectiveness of milk as a cutting fluid while attempting to drill small diameter holes in Cu [89]. In the article, a man visits a writer's shop to have a series of No. 80 (0.0135-inch) holes drilled into a 1/8-inch walled Cu tube. While the task appears straight-forward, it proved to be anything

but. As drilling began, the drill bit quickly "snapped off like so much glass." Several cutting fluids were tried – different oils, soap water, and other known lubricants – all ending in the same result. After breaking eleven drill bits and with no hole yet in the tube, milk was tried with the last remaining drill bit. With much surprise, the use of milk readily permitted the drilling of all the holes. While the author makes the claim that the milk contains just the right proportions of oil and water to make it both an effective lubricant and cooling agent, recent research suggests that the efficacy of milk as a cutting fluid may lie in its ability to engender a mechanochemical effect and suppress sinuous flow during deformation of the Cu.

4.3 Background

Copper belongs to a category of metals often described as being 'gummy' during machining [90]. Other soft and/or high strain-hardening metals with this distinction include Al, Ta, Nb, Ni alloys, and stainless steels. Their 'gummy' behavior is characterized by thick chip formation, large cutting forces, and residual defects on the cut surface, e.g., cracks and tears [10,14]. This 'gummy' behavior results from an unsteady, highly redundant mode of plastic deformation termed sinuous flow [10,12,91]. *In situ* observation of the cutting of 'gummy' metals has shown how sinuous flow develops and progresses. It starts as a plastic buckling instability on the workpiece surface, just ahead of the tool and forming chip. Starting as a bump, the bump grows in amplitude and begins to rotate away from the advancing tool; as it enters the shear zone, the bump elongates and becomes a fold. After passing through the shear zone, the fold becomes part of the forming chip and moves up the tool rake face [12]. **Fig. 4.1** is a high-speed image of the cutting of Ni 200 with an overlay of the strain field and flow streaklines obtained through digital image correlation (DIC). The zigzag appearance of the streaklines – resulting from the folding – is characteristic of sinuous flow.

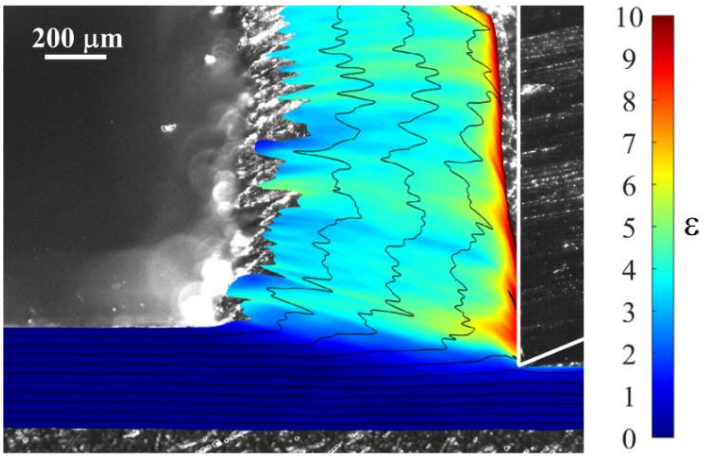

Figure 4.1. Deformation fields in cutting of nickel (α = 0°, h_0 = 100 μm, V_0 = 5 mm/s) from high-speed *in situ* imaging and DIC analysis. Flow is characterized by zigzag streaklines.

Recent work has revealed that sinuous flow can be dramatically inhibited or suppressed through a mechanochemical (MC) effect – change in the deformation behavior of a material due to the presence of a chemical medium [38]. The application of an appropriate surface-adsorbing (SA) medium can create a ductile-to-brittle transition during chip formation, transforming sinuous flow into segmented flow. This more desirable flow mode reduces cutting forces, lowers strains within the chip, and improves quality of the cut surface [10,92]. **Fig. 4.2** is a high-speed image showing this transition from sinuous to segmented flow with overlay of strain and streaklines. Strain and deformed chip thickness are reduced upon the ductile-to-brittle transition. **Fig. 4.3** are typical force traces displaying the reduction in forces that accompany the transition from sinuous to segmented flow.

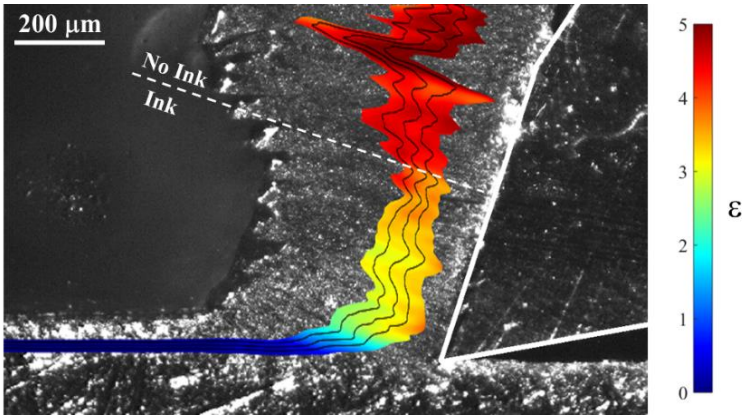

Figure 4.2. Transition of linear cutting of Ni 200 from non-ink to ink. The transition is marked by a nearly 35% reduction in chip thickness. Strain within the chip is reduced and streaklines become gentle. α = 20°, h_0 = 100 μm, V_0 = 5 mm/s.

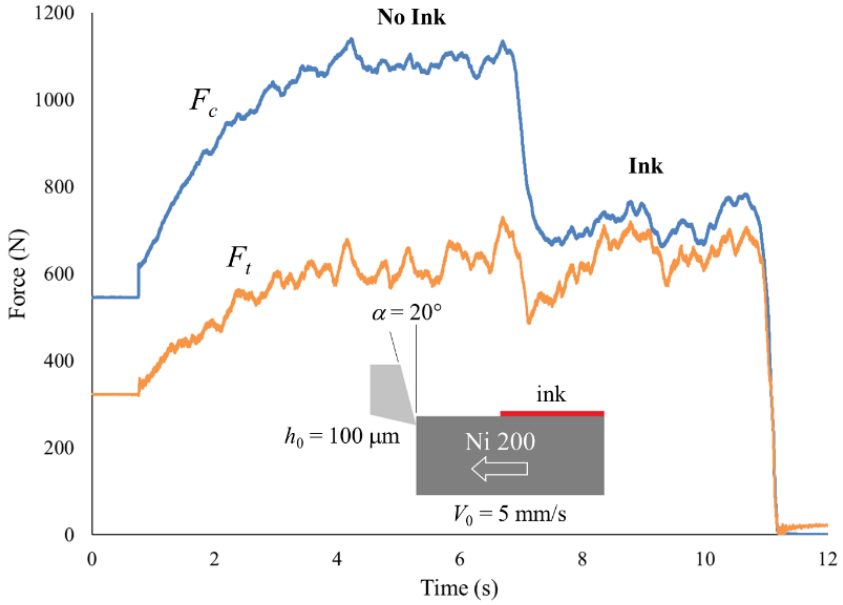

Figure 4.3. Measured cutting and thrust forces when linear cutting Ni 200 with a 20° tool. The latter half of the sample is coated with Sharpie permanent marker ink. A 35% drop in cutting force occurs at transition between bare and coated surface. h_0 = 100 µm, V_0 = 5 mm/s.

A variety of different media have been tested on 'gummy' metals to determine efficacy in suppressing sinuous flow. Originally, many of the experiments into mechanochemically-assisted machining used readily available media for coating and adhesion, e.g., inks and glues [92]. More recently, SA media has been expanded to include self-assembled monolayers (SAMs), green corrosion inhibitors (e.g., natural plant extracts), organic dyes, antibacterial drugs, and cows' milk. Regardless of the media used, the commonality among all is that strong adsorption appears key in creating the MC effect.

Until now, studies into mechanochemically-assisted machining have been performed at low cutting speeds (< 1 m/s) and one type of machining operation – linear cutting. While low cutting speeds have illuminated understanding into sinuous flow as a phenomenon through facilitating *in situ* imaging and eliminating thermal effects, it fails to address practical application in a production environment – where higher cutting speeds and significant heat generation are reality. Therefore, the objective of this study was to explore the cutting of 'gummy' metals with application of SA media at higher cutting speeds. Turning operations on copper, nickel, niobium,

and stainless steel reveal that, by using an appropriate SA media, the deleterious effects of sinuous flow can be ameliorated even at higher speeds.

4.4 Materials and Methods

4.4.1 Metals

To examine the impact of high cutting speeds on sinuous flow and the MC effect, four metals were chosen, all known to exhibit sinuous flow and respond to SA media. The metals selected were Cu 101, Ni 200, Nb, and Type 304 Stainless Steel (SS304). All were in rod form. The diameters of the Cu, Ni, Nb, and SS304 rods were 25.4, 25.4, 38.1, and 101.6 mm, respectively. The Cu, Ni, and SS304 rods were procured from McMaster-Carr Supply Co. with the Nb obtained from Admat Inc. Tables 1-8 provide the composition and known mechanical properties of the metals. The compositions of the Cu and Ni 200 were obtained via energy dispersive x-ray (EDX) spectroscopy, while those of Nb and SS304 are supplier-provided.

Table 4.1. Composition of Copper 101

Fe	Ni	S	Pb	Ag	Cu
0.19	0.08	0.02	0.02	0.01	99.68

Table 4.2. Mechanical Properties of Copper 101

Temper	H04 (hard)
Hardness (HRF)	65

Table 4.3. Composition of Nickel 200

Si	Cu	Mn	Fe	S	Ni
0.36	0.35	0.23	0.30	0.04	98.72

Table 4.4. Mechanical Properties of Nickel 200

Yield strength (MPa)	414
Temper	Hardened

Table 4.5. Composition of Niobium

Ta	C	O	W	N	Zr	Si	Hf	Mo	Fe	Nb
0.0480	0.0070	0.0061	0.0030	0.0039	<0.0005	0.0020	<0.0020	0.0010	<0.0015	Balance

Table 4.6. Mechanical Properties of Niobium

Tensile strength (MPa)	210
Yield strength (MPa)	145
Elongation (%)	30

Table 4.7. Composition of Type 304 Stainless Steel

Cr	Ni	Mn	Cu	Si	Mo	Co	N	W	V	Fe
18.140	8.110	1.640	0.450	0.430	0.330	0.237	0.083	0.080	0.060	Balance

Table 4.8. Mechanical Properties of Annealed Type 304 Stainless Steel

Tensile strength (MPa)	585
Yield strength (MPa)	263
Elongation (%)	58.5
Hardness (HB)	160

4.4.2 Cutting Apparatus

To accomplish higher speeds in machining, turning was performed on a Haas TL-2 CNC lathe. The cutting tool was mounted atop a force dynamometer (Kistler 9257B, natural frequency ~ 2 kHz), permitting measurement of the force in all three Cartesian directions. The forces of interest were the tangential force (F_t) and the radial force (F_r), or the cutting and thrust forces, respectively. A tool with rake angle 0° was fed radially into the workpiece (plunge cutting) at a rate of 100 μm/rev. Surface speeds used predominantly ranged from 1.3 to 5.3 m/s. Width of cut was 6.4 mm. When cutting with SA media, it was applied on the opposite side of the workpiece as the tool. A schematic of the setup is provided as **Fig. 4.4**. In addition to force measurements, 3D optical profilometry (Zygo NewView 8300) was used to characterize quality of the resulting cut surface for the case with and without media at different turning speeds. Chip morphology was examined through optical microscopy.

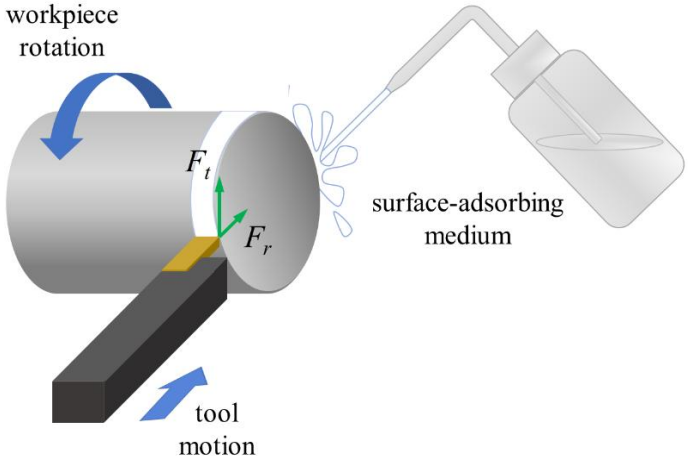

Figure 4.4. Experimental setup permitting the application of SA media at high cutting speeds in the turning of various ‘gummy’ metals.

4.4.3 Surface-Adsorbing Media

Ink as SA Media

One media that has consistently engendered the MC effect at low cutting speeds across ‘gummy’ metals is ink, specifically Sharpie permanent marker ink [92]. It has many desirable qualities: readily available, non-toxic [93], inexpensive, precision application, and good coverage [94,95]. More information concerning the properties of permanent marker ink is located in Appendix B. In many ways, ink has become a standard by which to compare the effects of other media. Naturally, it was the first medium attempted at higher cutting speeds. It was specifically tried during the turning of Cu and SS304; it did not result in a MC effect, as evidenced by no reduction in force, change in chip morphology, or visible improvement in surface quality. During the turning operations, a discernable odor emanated, presumably due to the burning away of the Sharpie permanent marker ink. Based on its chemical composition [93], standard Sharpie marker ink is heat resistant up to approximately 100°C. Industrial strength Sharpie permanent marker ink was also tried, stated on the label to be heat resistant up to 260°C. Again, it failed to produce a MC effect when used at higher cutting speeds.

Since Dykem metal marking ink has also been shown to create the MC effect at low cutting speeds [92], it too was tried at higher cutting speeds and failed to result in a MC effect. Per the manufacturer, Dykem has a boiling range of 77 – 125°C [96]. Like Sharpie, Dykem has a high

temperature ink as well, heat resistant to 1093°C. Since this version of Dykem had never been tried with low speed cutting, an experiment was performed using Nb as the workpiece metal. Even at a low cutting speed, the high temperature Dykem failed to generate a MC effect. Therefore, it was not attempted at higher cutting speeds.

Cows' Milk as SA Media

Due to the unsuccessful attempts in using ink as SA media in cutting at higher speeds, the use of cows' milk was explored due to an interesting property of protein adsorption. While physical adsorption is generally poor at elevated temperature, protein adsorption is unique in that it improves as temperature increases, particularly for the protein β-lactoglobulin (β-lg). Improved adsorption is due to conformational changes in the proteins (denaturation); at higher temperature, β-lg unfolds and exposes a core containing reactive sulfhydrl groups. This acts to strengthen adsorption to the metal and allows the protein to react and aggregate with similar or other disulfide-bond-containing proteins (e.g., casein, α-lg) [83].

While 2% cows' milk had previously been used at low cutting speeds and successfully generated a MC effect in Nb and SS304, consistently steady forces and uniform chip morphology were realized only after the milk film was permitted to dry for approximately 3 minutes. Since this requirement is not possible for higher speed cutting, a milk with a greater protein content was chosen to improve the adsorption rate. While 2% cows' milk contains approximately 3.3 g of protein per 100 g, the high-protein milk (Core Power Elite by Fairlife) contained 42 g of protein per 100 g. The high-protein milk was noticeably 'sticky' to the touch even at room temperature.

4.5 Results

4.5.1 Turning

Chip Morphology

Traditional optical microscopy was used to examine the morphology of the resulting chips obtained through turning. A caliper was used to determine an average thickness for each chip. **Figs. 4.5-4.8** provide a pictorial summary of chip morphology along with average deformed

thickness for each of the metals and their respective cutting conditions. Two major trends emerge. First, Cu, Ni, and Nb decrease in chip thickness as surface speed increases, with only SS304 remaining virtually the same. Second, chip thickness decreases upon cutting with cows' milk for all the metals, with the greatest decrease occurring at the lowest speeds. Again, the exception to this is SS304, experiencing the same decrease in chip thickness for all speeds.

For Cu, many of the chips display a periodic pile-up nature (**Fig. 4.5**). For the case of dry cutting at 1.3 m/s, there is a repeating pattern of a large folding event followed by three smaller folding events; this pattern occurs along the entire length of the chip. This oscillation of chip thickness between thick and thin is likely due to the strain state of the surface. In the first revolution of cutting, sinuous flow results in a thick chip and highly strain hardens the surface. This effectively pre-strains the surface for the next revolution of cutting. The prevailing flow mode thus becomes more laminar as opposed to sinuous, returning the surface to a near-annealed state [97]. When cutting with cows' milk, the thickness of the segmented chip decreases by 33%. For the cases of dry cutting at surface speeds of 2.7 and 5.3 m/s, much smaller scale folding events are present with much less periodicity. When cutting with cows' milk, segmentation is apparent. Chip thickness decreases by 24% and 17% for 2.7 and 5.3 m/s, respectively.

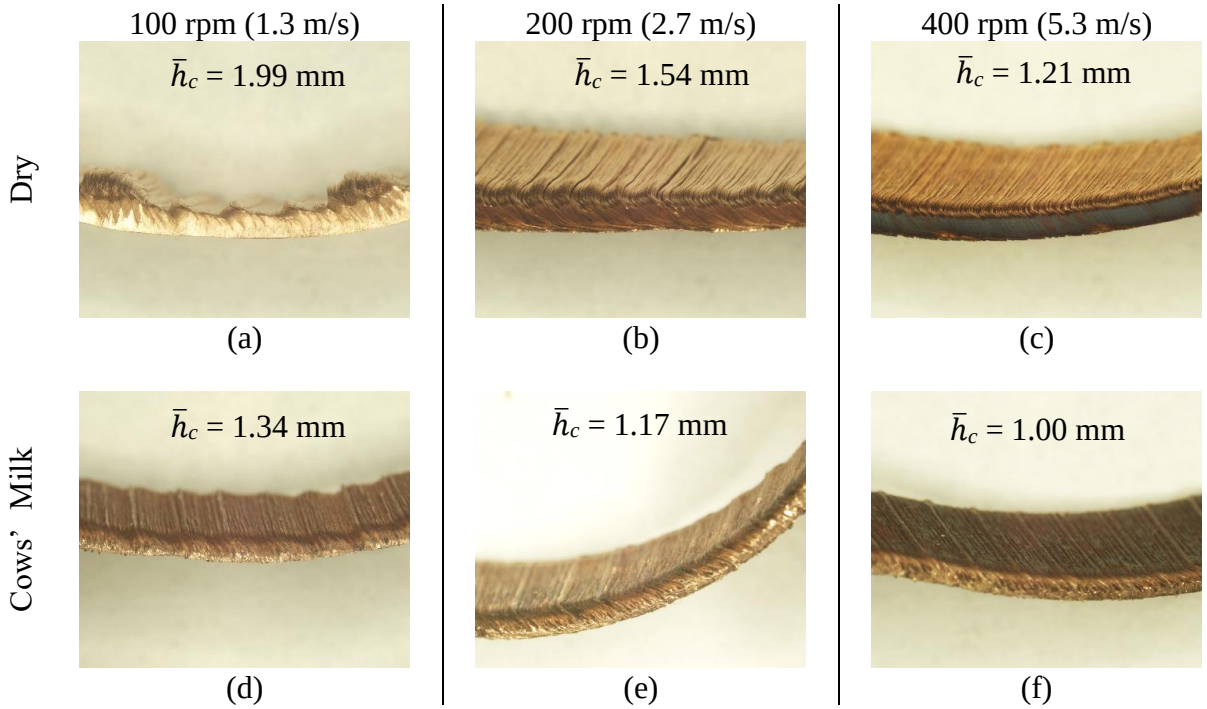

Figure 4.5. Cu chips produced from turning at surface speeds (a),(d) 1.3 m/s, (b),(e) 2.7 m/s, and (c),(f) 5.3 m/s, without and with the use of cows' milk.

Ni exhibits much the same behavior as noted in Cu (**Fig. 4.6**). For cutting dry at 1.3 m/s, a similar repeating pattern of a large-scale folding event is followed by two smaller folding events. Cutting with cows' milk eliminated the folding events and replaced it with segmentation. A 35% reduction in chip thickness occurred. For dry cutting at 2.7 m/s, the chip consisted of successive folds. Segmentation occurs upon cutting with cows' milk, resulting in a chip 28% thinner. At 5.3 m/s, cutting with milk produced a chip 30% smaller in thickness. At 10.6 m/s, dry cutting resulted in a chip with a regular folding pattern. The segmented chip from cutting with milk is 19% reduced in thickness.

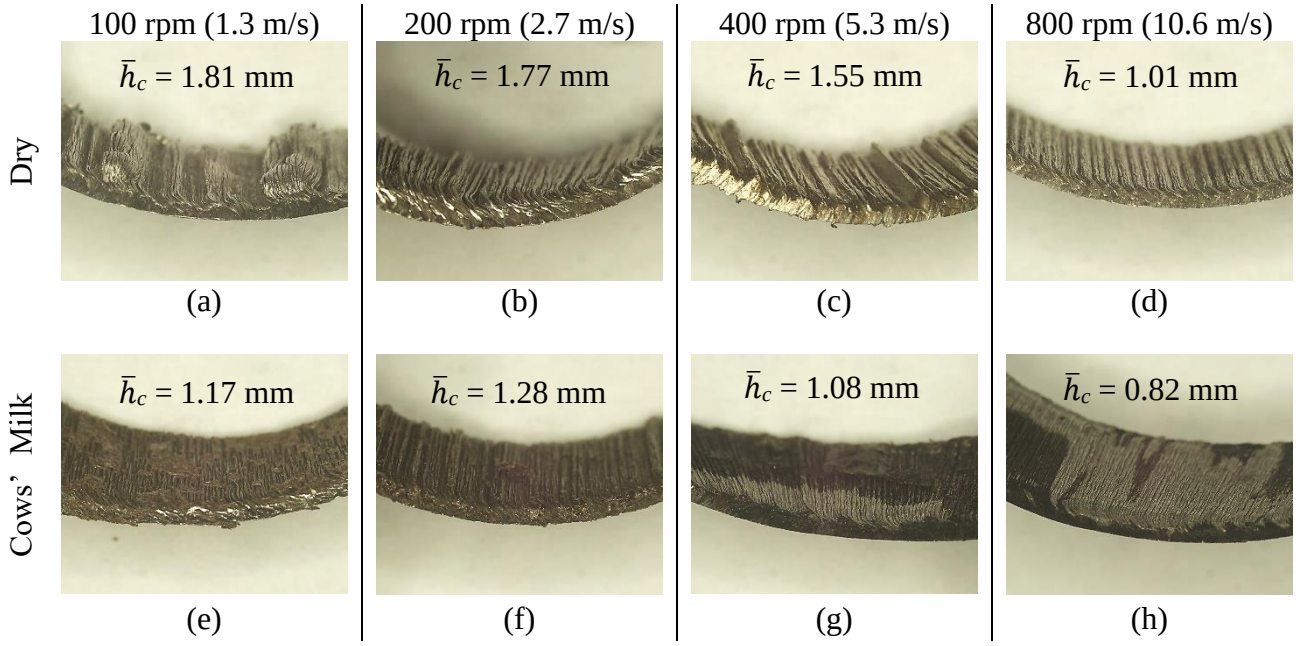

Figure 4.6. Ni chips produced from turning at surface speeds (a),(e) 1.3 m/s, (b),(f) 2.7 m/s, (c),(g) 5.3 m/s, and (d),(h) 10.6 m/s, without and with the use of cows' milk.

An additional cutting condition was added when turning Nb; water was used as a cutting medium to determine if cooling would impact the operation. The chip morphology of Nb is quite different than either Cu or Ni (**Fig. 4.7**). For dry cutting and cutting with water at 2.0 m/s, the chips are a collection of piled-up folds, many varying in height and location across the width of the chip. Upon cutting with cows' milk, segmentation effectively prevents these folding events from occurring, yielding a chip 49% thinner. At double the cutting speed (4.0 m/s), the folding events are not as severe and extend across the entire width of the chip for cutting dry and with water.

Again, cows' milk results in a segmented chip, one that is 31% less in thickness than the chip produced by dry cutting.

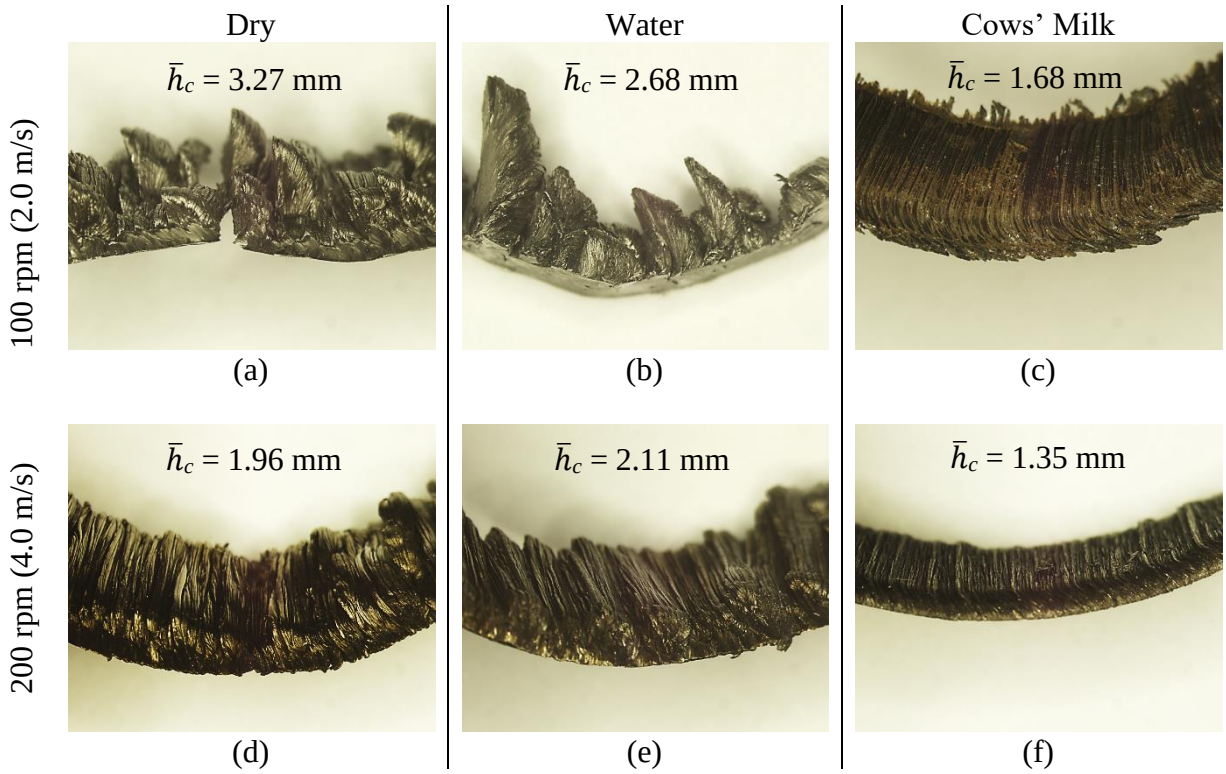

Figure 4.7. Nb chips produced from turning at surface speeds (a)-(c) 2.0 m/s and (d)-(f) 4.0 m/s – cutting dry, with water, and with cows' milk.

The least change in chip morphology is noted for SS304 (**Fig. 4.8**). While the chip becomes slightly thinner when cutting with milk (~ 17% reduction), there is no significant change in the free surface texture of the chip. Chip thickness remains approximately the same across the different cutting speeds when cutting dry and cutting with milk.

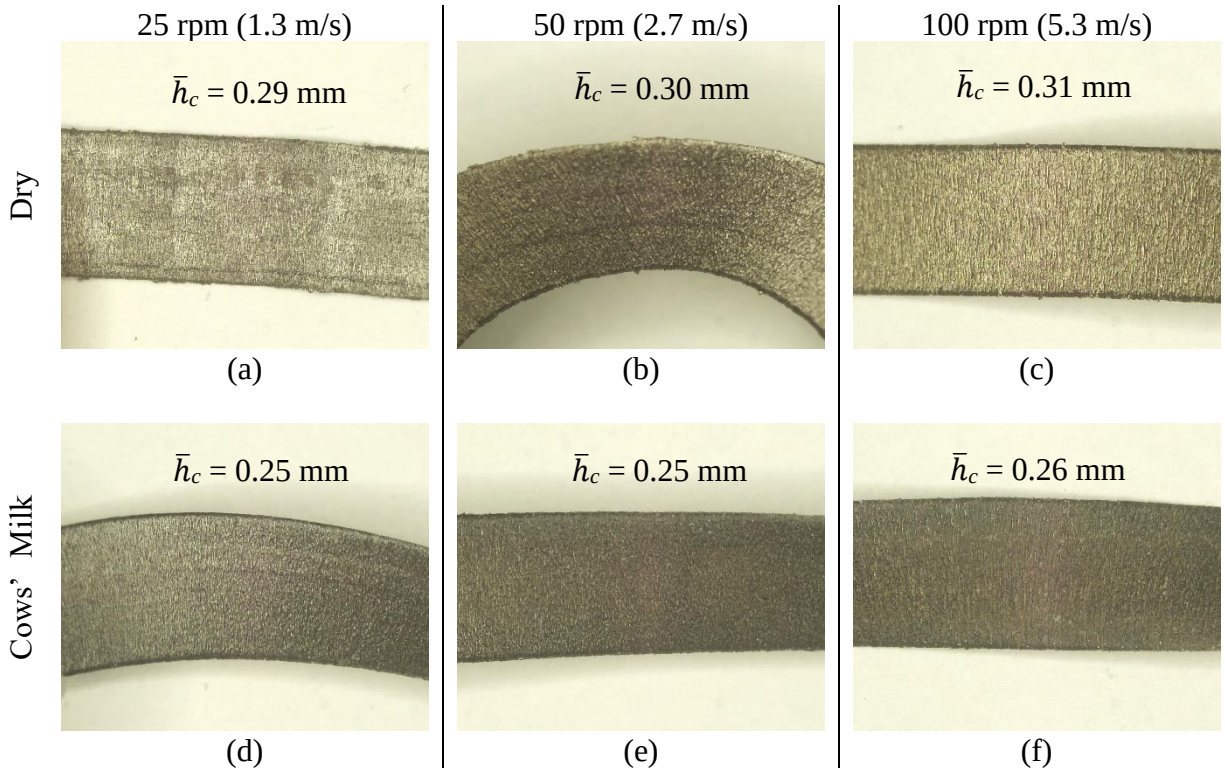

Figure 4.8. SS304 chips produced from turning at surface speeds (a),(d) 1.3 m/s, (b),(e) 2.7 m/s, and (c),(f) 5.3 m/s, without and with the use of cows' milk.

Surface Quality

3D optical profilometry (Zygo NewView 8300) was used to characterize the resulting surface quality of the cut workpieces. The only exception was the SS304 workpiece, as its diameter was too large to fit within the profilometer imaging space. As a result, an image of the workpiece is provided for visual comparison between cutting conditions. Measurements (each 1.68 mm × 1.68 mm) were taken every 45° along the circumference of each workpiece, for a total of eight measurements for each cutting condition. This sampling represents only 22.6 mm^2 of the total surface for the rods – 3.7% and 2.5% for the 25.4-mm and 38.1-mm rods, respectively. **Figs. 4.9-4.11** summarize the results for surface roughness in terms of arithmetical mean height (*Sa*). **Fig. 4.12** is an image of the SS304 workpiece.

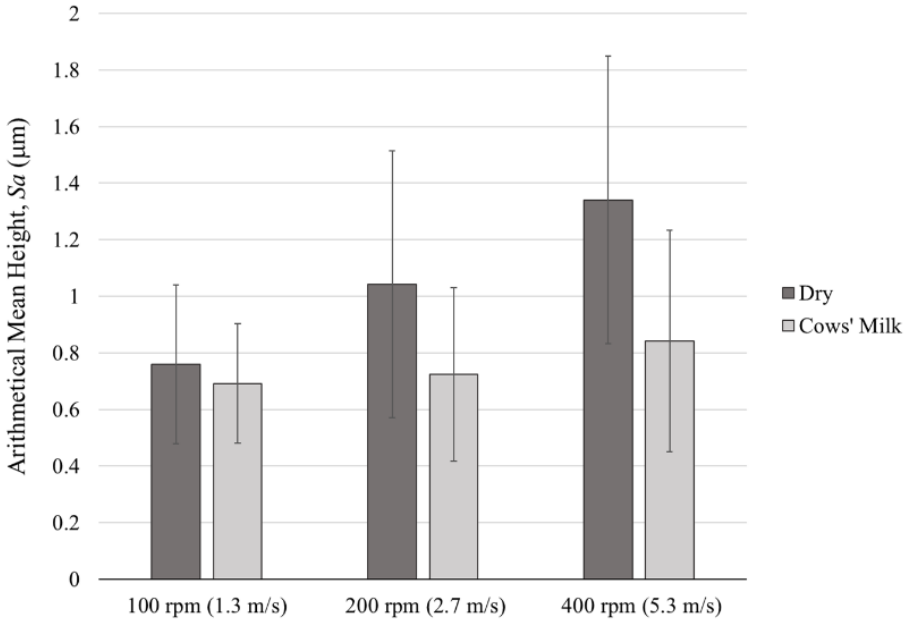

Figure 4.9. Surface roughness of Cu workpiece in terms of arithmetical mean height (*Sa*) for surface speeds of 1.3, 2.7, and 5.3 m/s when cutting dry and with cows' milk.

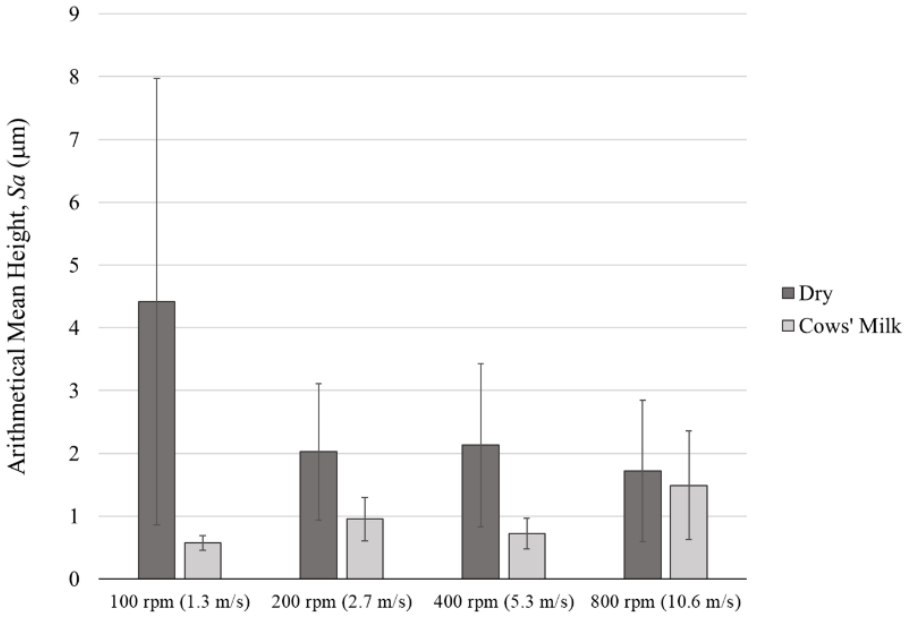

Figure 4.10. Surface roughness of Ni workpiece in terms of arithmetical mean height (*Sa*) for surface speeds of 1.3, 2.7, 5.3, and 10.6 m/s when cutting dry and with cows' milk.

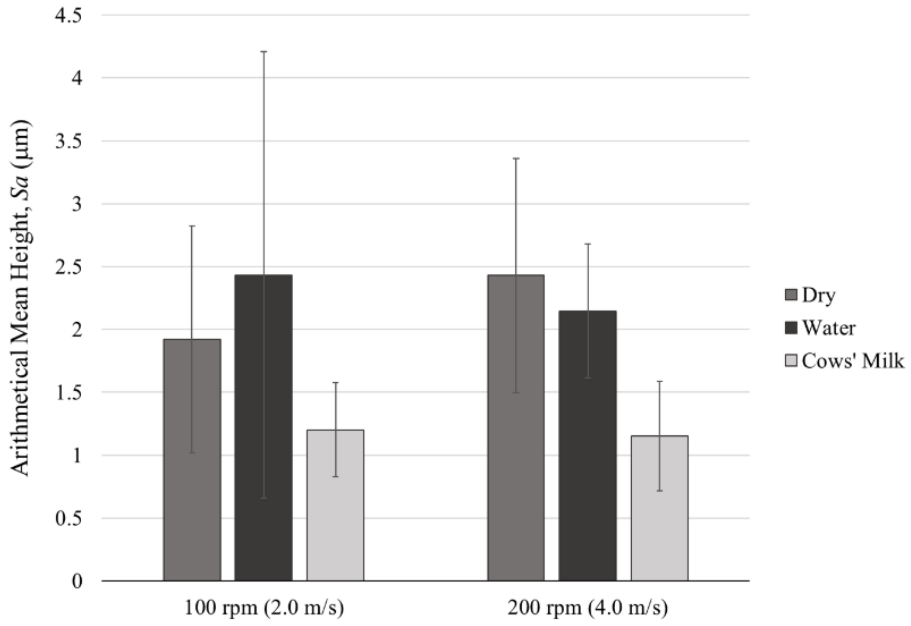

Figure 4.11. Surface roughness of Nb workpiece in terms of arithmetical mean height (*Sa*) for surface speeds of 2.0 and 4.0 m/s when cutting dry, with water, and with cows' milk.

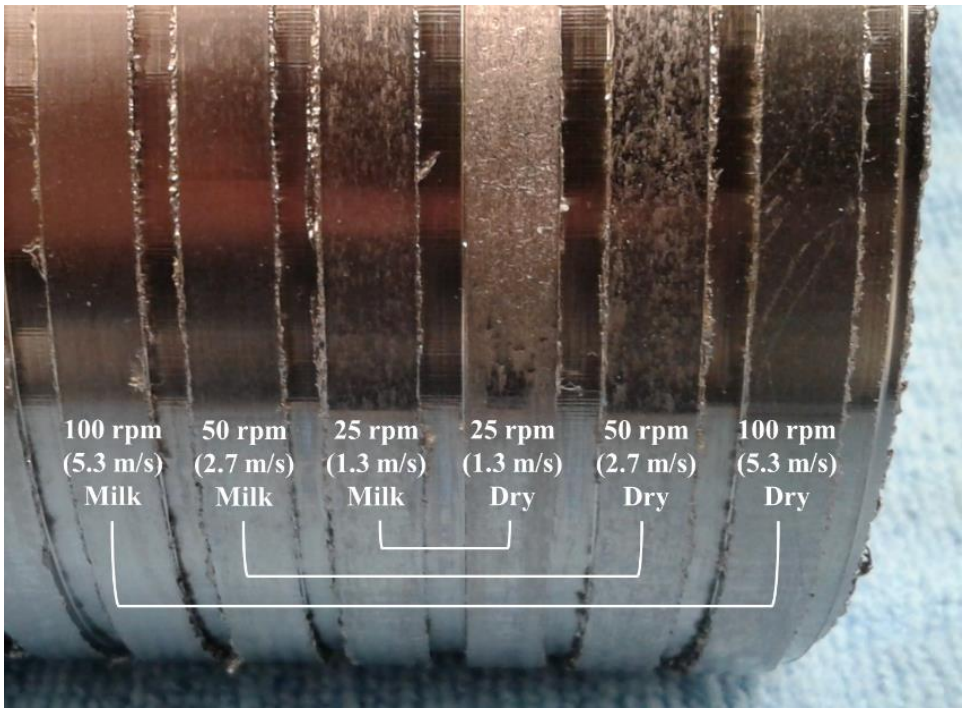

Figure 4.12. Surface finish of SS304 workpiece for surface speeds of 1.3, 2.7, and 5.3 m/s when cutting dry and with cows' milk. For all cutting speeds, scratches and pitting are more prevalent when cutting dry than when cutting with cows' milk.

For all metals, surface quality improves when cutting with cows' milk, as evidenced by lower average *Sa* values than when cutting dry. The standard deviation in *Sa* is also less when cutting with milk. The larger standard deviation in *Sa* when cutting dry can be attributed to regions of material pull-out. As examples, **Figs. 4.13a,b** are profilometer generated images for Ni and Nb showing the appearance of this material pull-out. When cutting with cows' milk, the average surface roughness is nearly the same regardless of cutting speed. Interestingly, all roughness values – regardless if cut dry, with water, or with milk – fall within what is considered average performance for turning [98].

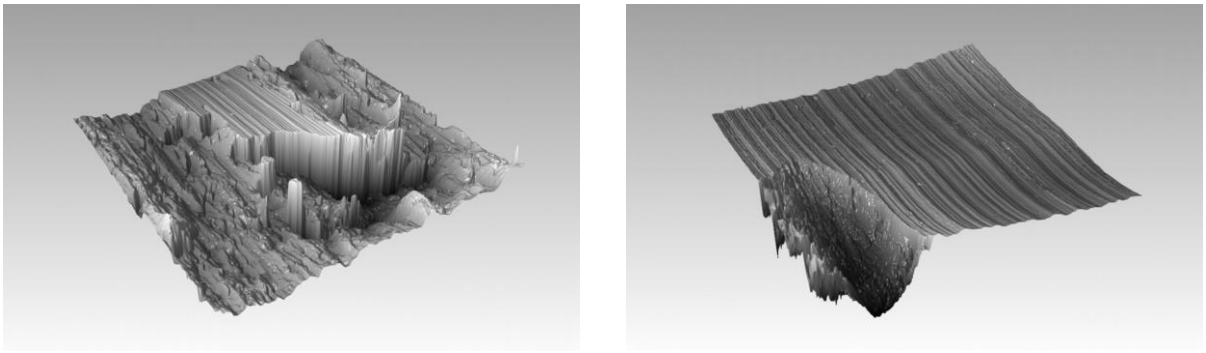

(a) (b)

Figure 4.13. Profilometer generated surfaces (1.68 mm × 1.68 mm) of (a) Ni and (b) Nb. Surfaces show both regions of active-cutting, as evidenced by tool marks, and material pull-out.

Forces

In low-speed linear cutting, one of the distinguishing characteristics of the MC effect is a reduction in force. However, it was unknown whether force reduction is present in high-speed cutting. **Fig. 4.14** are typical thrust (radial) and cutting (tangential) force traces for turning. The forces steadily ramp up and then reach a steady state. It should be noted that the forces have a degree of oscillation (i.e., chatter), fluctuating between a maximum and minimum.

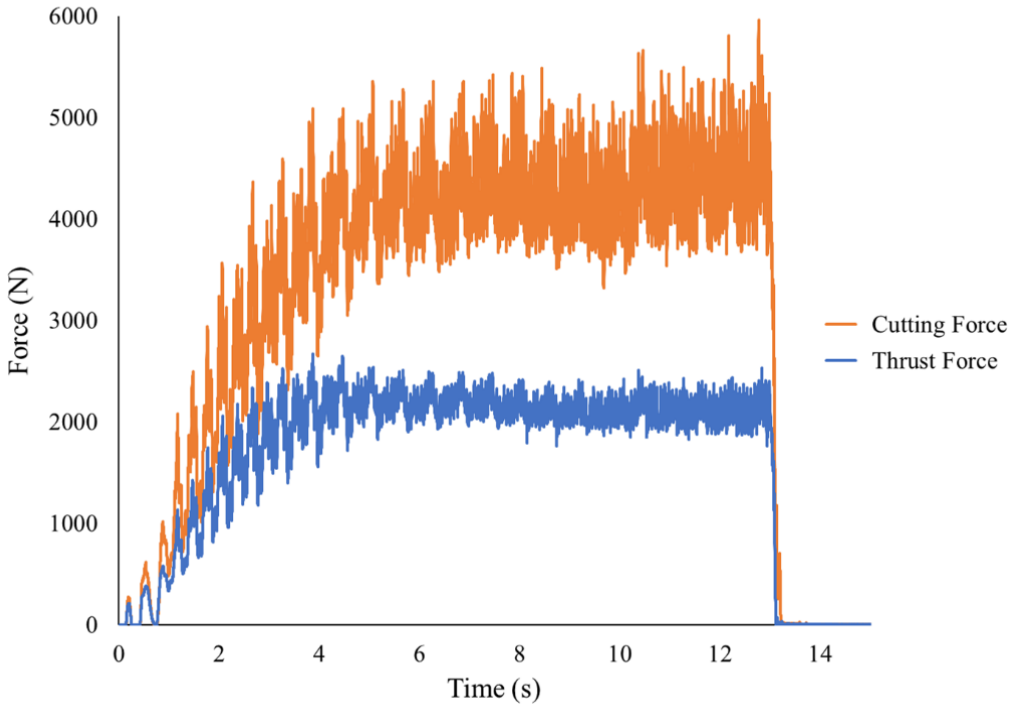

Figure 4.14. Prototypical force traces for turning. There is an initial ramp-up in force followed by a steady-state condition.

Fig. 4.15 summarizes the force results – average force measurements with standard deviation error bars for the steady state region of the force trace – for the turning of Cu for the surface speeds of 1.3, 2.7, and 5.3 m/s. The standard deviation represents the fluctuation in the force. A statistically significant force reduction occurred upon cutting with cows' milk. For the surface speeds of 1.3 and 2.7 m/s, the average cutting force was reduced by 25%. For 5.3 m/s, the force reduction was only 14%. Also, the standard deviations (i.e., force fluctuations) are less when cutting with cows' milk.

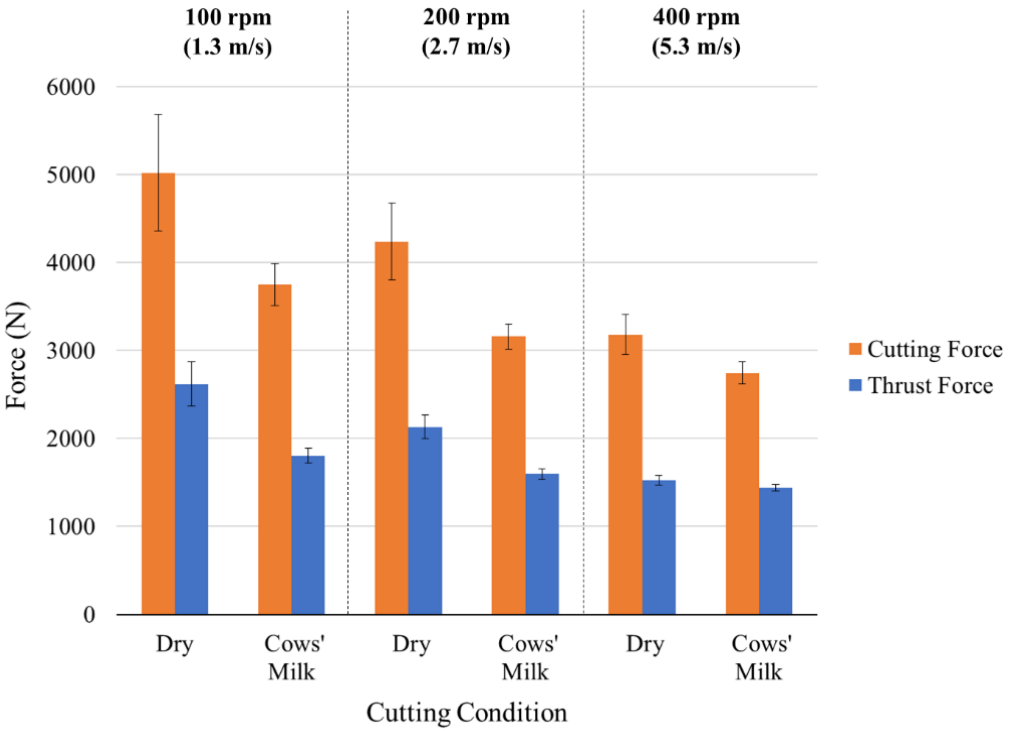

Figure 4.15. Average force values obtained during the turning of Cu for surface speeds 1.3, 2.7, and 5.3 m/s for a radial feed of 100 μm/rev when cutting dry and with cows' milk. Force reductions occur for all cutting conditions when cutting with milk as opposed to cutting dry.

Unlike Cu, force reduction when cutting with cows' milk was not as dramatic (**Fig. 4.16**) for the surface speeds of 1.3, 2.7, 5.3, and 10.6 m/s, although the average force when cutting with cows' milk is less with the exception of the 10.6 m/s surface speed. As observed in Cu, the force fluctuations were also less.

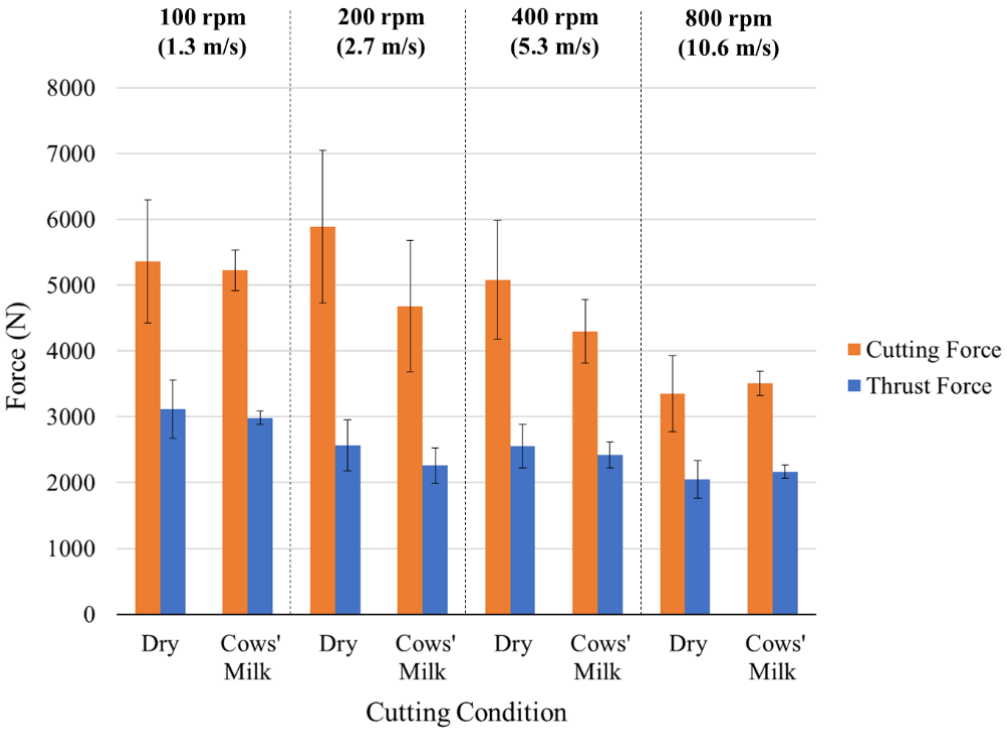

Figure 4.16. Average force values obtained during the turning of Ni for surface speeds 1.3, 2.7, 5.3 m/s, and 10.6 m/s for a radial feed of 100 μm/rev when cutting dry and with cows' milk. Reductions in average force are noted for 2.7 and 5.3 m/s when cutting with milk as opposed to cutting dry. Force fluctuations are less when cutting with milk for all surface speeds.

Like Ni, Nb does not exhibit a significant reduction in force when cutting with cows' milk (**Fig. 4.17**) for surface speeds of 2.0 and 4.0 m/s, although the average force when cutting with cows' milk is less. Once again, the force fluctuations were less. Not only was the cutting performed dry and with cows' milk, but water was also tried to determine if the milk was simply acting as a coolant. The average force magnitudes and standard deviations when cutting with water are very similar to those when cutting dry.

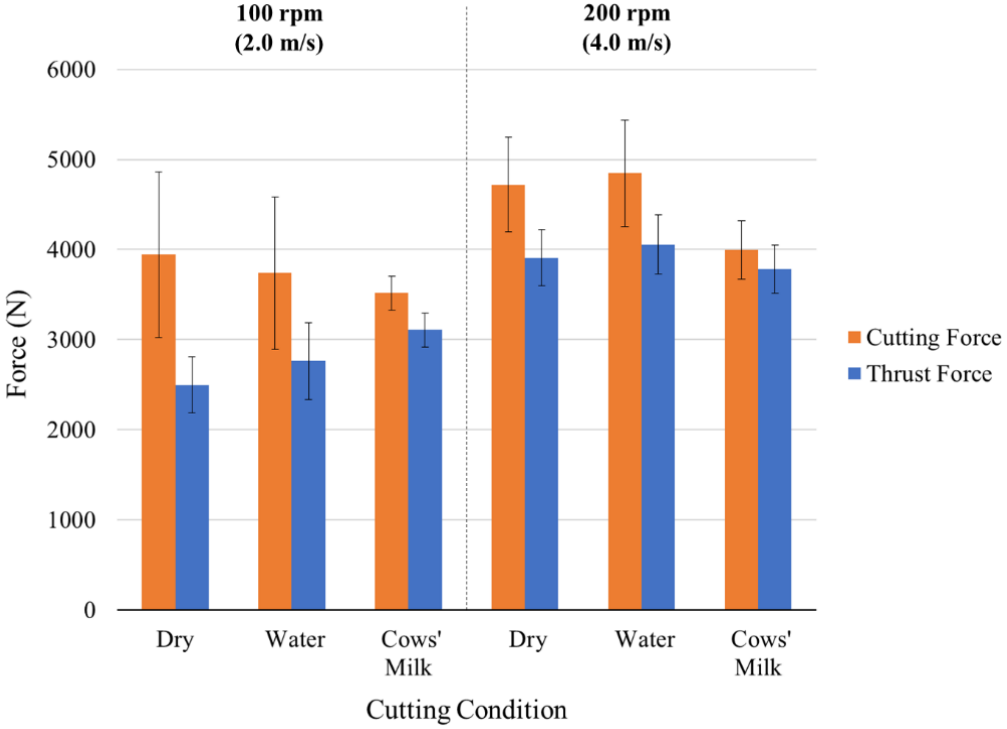

Figure 4.17. Average force values obtained during the turning of Nb for surface speeds 2.0 and 4.0 m/s for a radial feed of 100 μm/rev when cutting dry, with water, and with cows' milk. Reductions in average force are noted for both speeds when cutting with milk as opposed to cutting dry. Force fluctuations are less when cutting with milk for all surface speeds.

For SS304 (**Fig. 4.18**), there is no statistically significant force reduction associated with cutting with cows' milk as opposed to cutting dry for surface speeds of 1.3, 2.7, and 5.3 m/s. Unlike in the other tested metals, force fluctuations do not differ substantially in the case of cutting with cows' milk. It should also be noted that thrust and cutting forces are considerably lower in SS304 than the other metals.

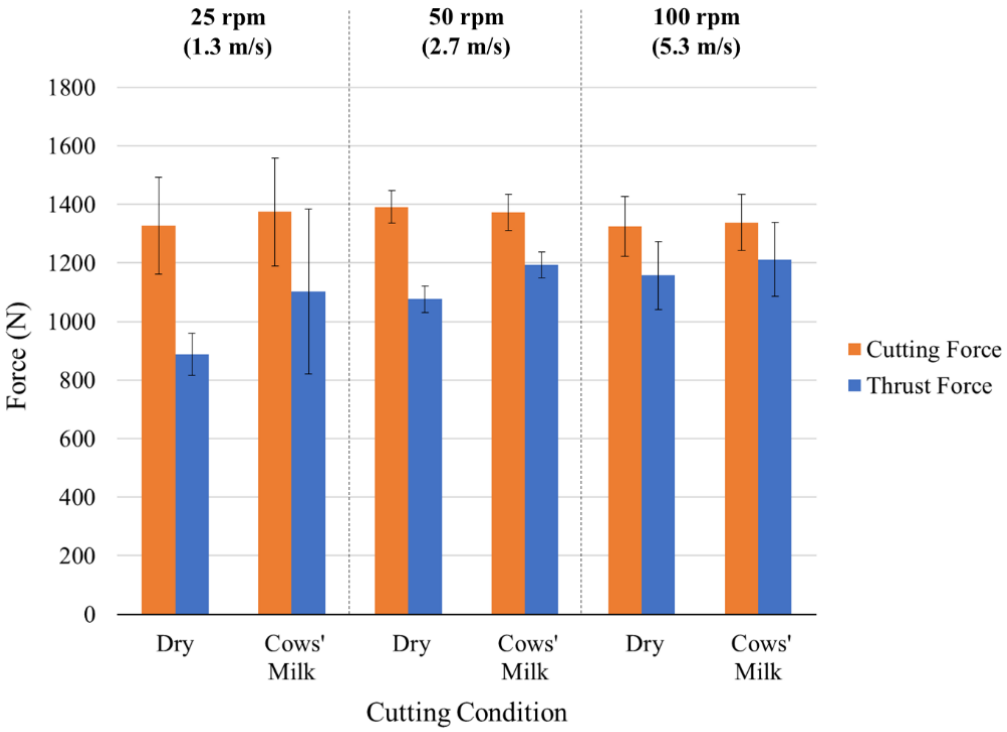

Figure 4.18. Average force values obtained during the turning of SS304 for surface speeds 1.3, 2.7, and 5.3 m/s for a radial feed of 100 μm/rev when cutting dry and with cows' milk. Forces are virtually the same across all cutting conditions.

4.5.2 Drilling

Revisiting the century-old account related at the beginning of this article, a couple of simple experiments were performed to probe the efficacy of milk as a cutting fluid while drilling Cu. A benchtop drill press with manual feed was converted to automatic feed using a pulley system with a Durston powered rolling mill as the drive component. The rolling mill permitted precision feed rate control of the drill. Twist-type drill bits used were titanium nitride coated high speed steel with 1/16-inch and 1/8-inch diameters with tip angle of 118°. The workpiece used was 1/4-inch thick commercially pure Cu 101 plate. The workpiece was affixed atop a four-component dynamometer (Kistler 9272), enabling measurement of torque and three orthogonal components of force. The experimental setup is shown in **Fig. 4.19**. The rotational speed was 760 rpm with a feed rate of approximately 0.003 inches per revolution. Three cutting conditions were tested: dry (no lubricant), Mobil 1 as lubricant, and cows' milk.

Figure 4.19. Experimental setup for the drilling of Cu. A benchtop drill press was modified to provide a controllable, constant feed rate. Cu workpiece mounted atop a piezoelectric dynamometer to measure thrust force and torque.

The resulting traces for thrust force and torque are provided in **Figs. 4.20a,b** for the 1/16-inch drill bit and **Figs. 4.21a,b** for the 1/8-inch drill bit. The use of cows' milk results in significantly lower thrust force and torque values, approximately 30% and 40% less for the 1/16-inch bit and 50% and 60% less for the 1/8-inch bit. When using cows' milk, the force (and torque) traces are relatively constant – a characteristic that has been noted in low-speed linear cutting. When using Mobil 1, the results are somewhat more mixed. For the 1/16-inch bit, the thrust force and torque abruptly increase halfway through the drilling; this suggests lubrication between chip and tool has decreased. The thrust force and torque are initially lower than when using cows' milk and then becomes nearly equal to or higher. For the 1/8-inch bit, Mobil 1 results in a thrust force and torque midway in magnitude between when cutting dry and with cows' milk. It should be noted that the drill dwell time is also less when cutting with cows' milk as a result of less resistance. Dwell time when using Mobil 1 is only less with the use of the 1/8-inch bit. In addition, when cutting with cows' milk and Mobil 1, chips were longer in length and more flexible when bent than when cutting dry (no lubrication), indicating less strain hardening.

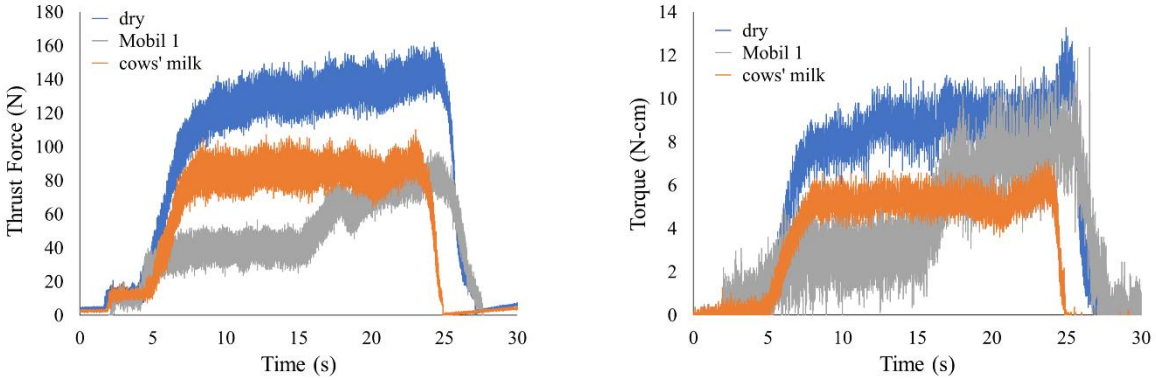

(a) (b)

Figure 4.20. (a) Thrust force and (b) torque traces for drilling of 1/8-inch Cu sheet with 1/16-inch diameter drill bit. When cutting with cows' milk, there is a 30% reduction in thrust force and 40% reduction in torque when compared to cutting dry. The traces are steady when using cows' milk, as opposed to when cutting dry or when using Mobil 1.

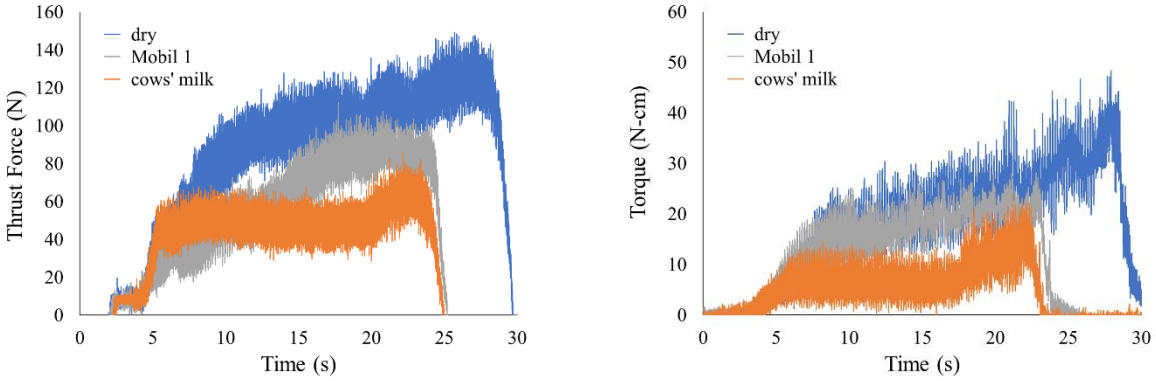

(a) (b)

Figure 4.21. (a) Thrust force and (b) torque traces for drilling of 1/8-inch Cu sheet with 1/8-inch diameter drill bit. When cutting with cows' milk, there is a 50% reduction in thrust force and 60% reduction in torque when compared to cutting dry. The traces are steady when using cows' milk, as opposed to when cutting dry or when using Mobil 1.

4.6 Discussion

Turning experiments with Cu, Ni, Nb and SS304 confirm that sinuous flow is observed at higher cutting speeds and can effectively be ameliorated via a MC effect using an appropriate SA medium. Chip morphology, surface roughness, and force measurements support this assertion – together providing a consistent narrative as to the nature of chip formation in 'gummy' metals at higher cutting speeds with and without use of SA media during cutting. In general, the same

characteristic features present during low-speed linear cutting are expressed at higher cutting speeds. When cutting with cows' milk, a change in chip morphology was observed along with a corresponding reduction in chip thickness. For Cu, Ni and Nb, chips dramatically transitioned from irregular, with notable pile-up events (sinuous), to uniform in appearance (segmented). Surface roughness (average *Sa*) also improved when cutting with cows' milk for all metals. While only a dramatic decrease in force was noted in the cutting of Cu, a decrease in average force was exhibited by Ni and Nb when cutting with cows' milk and a reduction in force fluctuation.

Using cows' milk in the cutting of Cu, Ni, Nb and SS304 resulted in markedly better surface roughness. Improved surface quality via a MC effect should not be understated. In addition to providing a part with better wear characteristics, studies on Cu, Ni and stainless steels have established a significant influence of surface roughness on corrosion resistance. An increase in surface roughness increases pitting susceptibility and the corrosion rate of these metals [99–101].

Experiments with drilling Cu reveal that cows' milk does serve as an effective cutting fluid when drilling – resulting in lower thrust force and torque than when cutting dry (no lubricant) and more consistent force and torque than when cutting with Mobil 1. The consistent, constant force and torque are suggestive of a MC effect. Additional work needs to be performed to determine if the cows' milk is in fact creating a MC effect when drilling.

By using SA media to engender a MC effect, it improves the machinability of 'gummy' metals by increasing the range of available cutting parameters that yield acceptable surface quality, most notably giving access to lower cutting speeds. Cutting at lower speeds decreases thermal effects, reducing microstructural changes at the workpiece surface and translating into longer tool life. In addition, SA media reduces force fluctuations, which can also help to extend tool life. The longer a tool can be in-service, the greater the productivity and ultimately profitability.

Higher cutting speeds yield higher temperatures and must be taken into consideration when using SA media, as demonstrated by the ineffectiveness of Sharpie and Dykem inks. Due to the nature of protein adsorption, cows' milk remains effectual even at elevated temperatures. Formulation of a synthetic cutting fluid for the purpose of generating a MC effect would need to ensure the active adsorption agent remains strongly adsorbed at high temperatures.

4.7 Conclusions

While the ‘gummy’ metals of Cu, Ni, Nb and SS304 were found to exhibit sinuous flow at cutting speeds between 1 and 5 m/s, the use of the SA medium of cows’ milk effectively gave rise to a MC effect, creating a ductile-to-brittle transition – transitioning sinuous flow to segmented flow. Just as observed in lower cutting speeds (< 1 m/s), chip thickness decreased, quality of the workpiece surface improved, and reductions in average force occurred (except for SS304). While cows’ milk proved successful in engendering a MC effect at high cutting speeds, the application of ink – effective at low cutting speeds – was unsuccessful. This implies adsorption characteristics at elevated temperature must be a consideration when choosing SA media for high speed cutting.

5. CONCLUSIONS

The objective of this research was to expand the phenomenological study of flow modes in cutting, and utilization of mechanochemical effects, to the critical technology metals and alloys – tantalum, niobium, austenitic stainless steels, and nickel – all well known for their corrosion resistance. Equally importantly, these metals have poor machinability and are characterized by gumminess in cutting. It was hypothesized that the poor machinability and gumminess is due to chip formation occurring by sinuous flow, and that SA media would disrupt the sinuous flow in cutting of these corrosion resistant metals, analogous to the Al and Cu model systems studied in prior work. As posited, the metals Ta, Nb, SS304 and Ni were found to exhibit sinuous flow in large strain deformation – with characteristic large amplitude folding, high cutting forces, and poor cut surface finish. The occurrence of this type of flow, typical of highly strain hardening metals, was established by *in situ* imaging of the deformation, force measurements, and optical profilometry. In the presence of appropriate SA media, the sinuous flow was disrupted and replaced by a segmented flow mode characterized by quasi-periodic fracture and saw-tooth chip morphology. The segmented flow is more characteristic of cutting of semi-brittle metals. The forces were reduced by as much as 75%, and the chip strain by up to 40%, in the presence of the media. Furthermore, the cut surface quality was improved by almost an order of magnitude. The disruption of sinuous flow by segmented flow resembles a ductile-to-brittle transition – a mechanochemical effect due to the SA media.

A strong coupling of the flow mode and media action was found to underly the MC effect. Sinuous flow promotes formation of notch-like features in the deformation region due to the folding. It was hypothesized that the media forms a thin, strongly adsorbed layer on the workpiece surface, this adsorption altering the surface energy and surface stress. Since the notches are natural stress concentrators, a change in these parameters effected by the adsorbed media triggers crack nucleation – hence, a ductile-to-brittle (sinuous-to-segmented) transition. This research offers further support for this hypothesis.

The deformation behavior of Ta, Nb, SS304 and Ni in cutting is not unlike that of Al and Cu. Although the rate and severity of fold nucleation in Ta and Nb, is notably more severe than in Al and Cu, the underlying mechanics remains qualitatively the same – giving rise to the requisite notch formation necessary for the occurrence of the ductile-to-brittle transition in the presence of

a strongly adsorbed media. Likewise, although not as prominent, folding is present in SS304 and Ni as well. Therefore, the hypothesis element that sinuous flow – hence, folding – must be present for the MC effect is supported, as is the coupling between poor machinability and sinuous flow.

Another element of the hypothesis of the MC effect is that the applied media must strongly adsorb to the workpiece surface, so as to sufficiently alter surface energy and surface stress to trigger cracks at the deformation-induced notches. Prior studies with Al and Cu used media (e.g., permanent inks, glues) whose design and function are strong adherence to a wide variety of surfaces. By using other types of media (i.e., natural extracts, dyes, amoxicillin and cows' milk) – not considered for marking and joining – the importance of adsorption is demonstrated clearly in the present study. These natural adsorbates also highlight the selectivity of adsorption – the adsorbate-metal pairing must be compatible to ensure strong adsorption. While all the natural extracts and dyes that were selected adsorbed well to SS304, confirmed independently through the literature, they do not readily adsorb to Nb; this is consistent with lack of occurrence of an MC effect with Nb. The importance of adsorption was further highlighted by varying the concentration of adsorbate. As adsorbate concentration is decreased, the mechanochemical effect displays less efficacy – as evidenced by an increase in cutting force and chip thickness compared to the higher concentrations. In addition, temperature rises at higher cutting speeds support the conclusion that strong adsorption is necessary for the occurrence of the MC effect. The failure of physically-adsorbed inks to generate a MC effect at higher speeds (hence, higher temperatures) again points to the necessity of adsorption for the MC effect to manifest; once the inks desorb, the MC effect stops.

While some mechanochemical phenomena can be directly attributed to corrosion, e.g., environment-assisted cracking, the use of corrosion-resistant metals effectively eliminates corrosion as a factor with regards to the observed MC effect while cutting with the present SA media. While the present experiments did not resolve the relative roles of surface energy and surface stress in determining the MC effect, the observations broadly point to a local change in surface stress as the most plausible route by which the ductile-to-brittle transition occurs.

While much of the research into sinuous flow and the MC effect to date has been performed at low speeds, this study also convincingly validates those results at higher cutting speeds (> 1 m/s) and bridges the gap between laboratory and production floor. SA media selection for these speeds requires some additional considerations regarding adsorption rate and thermal stability, but it has

been demonstrated that media (e.g., cows' milk) exist that effectively suppress sinuous flow at industrial cutting speeds. The common approach to dealing with gummy metals has been to increase tool rake angle and cutting speed – much to the detriment of tool life. The MC effect offers a powerful new route by which less positive rake angles and lower cutting speeds may be used to obtain equivalent or even better surface finish while lowering cutting forces, reducing thermal effects and extending tool life.

In summary, this study furthers our understanding of sinuous flow, especially its widespread occurrence with highly strain hardening metals (tantalum, niobium, austenitic stainless steels, and nickel), and the key role of adsorption in creating the MC effect. All these metals and alloys were found to exhibit high cutting forces, thick chip formation, and poor finish on the cut surface as revealed through *in situ* imaging, digital image correlation, force dynamometry, and optical profilometry. Compared to Cu and Al, Ta and Nb displayed greater severity in folding, while SS304 and Ni showed less folding. Regardless, the underlying mechanics of fold nucleation and formation remained the same – implying no other flow mode beyond sinuous is responsible for the 'gummy' response of metals and alloys. By using various natural organic media, that are well-known as corrosion inhibitors, we have established that media adsorption on the metal surface is requisite to the MC effect. Furthermore, since these metals are corrosion resistant, it is demonstrated that adsorption – not a corrosive action – is what is responsible for the MC effect. Lastly, turning experiments confirm sinuous flow occurs at higher cutting speeds, but with proper selection of media, it can still be suppressed. The efficacy of natural organic media in suppressing sinuous flow shows a promising solution to cutting gummy metals in an industrial setting as these media are readily available and eco-friendly.

6. FUTURE WORK

While the basic elements of the hypothesis for the mechanochemical effect have been largely supported, there remain some areas that would greatly benefit through further investigation. Areas of research include: (1) chip formation and flow mode at higher cutting speeds, (2) identification of a single protein that can effectively engender the MC effect, and (3) quantification of adsorbate-induced surface stress.

First, although experiments at higher cutting speeds have revealed that chip formation appears quite similar to that at lower cutting speeds, it would be advantageous to have an experimental setup capable of imaging at higher speeds. The current linear cutting apparatus lacks the necessary rigidity to cut these corrosion-resistant, highly strain-hardening metals at speeds greater than 5 mm/s. Imaging while turning is also problematic due to the inherent kinematics of the operation and space constraints. A more rigid linear cutting apparatus would reveal any coupling between speed and plastic deformation in the shear zone and illuminate thermal effects more fully. Attempts were made to artificially increase the temperature via conductive heating during low-speed linear cutting, but those efforts were largely unsuccessful in obtaining sufficiently high temperatures (> 100°C). A more robust setup would permit the creation and *in situ* monitoring of heat generation during cutting. Therefore, media action may more fully be understood.

Second, as revealed through this research, cows' milk proved to be an effective SA medium across multiple metals and alloys for cutting speeds < 5 m/s. While abundant, inexpensive, and easily applied, the main downside to using milk as a medium is that it does sour and could promote bacterial growth in machines if not properly cleaned, potentially becoming harmful to machine operators. Instead of using milk, a single protein could prove just as effective and possibly eliminate the negative attribute. Many of the proteins within milk, such as β-lactoglobulin and bovine serum albumin, are already available separate from milk and should be explored further as SA media or as additives to traditional cutting fluids. An exciting and emerging field is the development of synthetic proteins – non-naturally occurring proteins designed to serve specific functions. Although likely years away, such a synthetic protein could improve adsorption characteristics and be immune to fermentation.

Lastly, recent work within our research group with self-assembled monolayers (SAMs) strongly suggest that the mechanochemical effect is driven by adsorbate-induced surface stress, as opposed to adsorbate-induced surface energy. A SAM molecule comprises of a head group that strongly bonds to the metal surface, a hydrocarbon chain, and a terminal group. The head and terminal groups determine the adsorbate-metal interface energy and adsorbate free surface energy, respectively, while the hydrocarbon chain length controls the induced surface stress. By holding the head and terminal groups constant for five SAMs of varying chain length, it was shown that the interface and adsorbate free energies did not change. While the two SAMs with the shortest chain lengths failed to result in a MC effect, the remaining three of longer chain length did so, as revealed by reductions in cutting force. Direct measure of adsorbate-induced surface stress would provide further evidence. Measurement of surface stress may be accomplished by using microcantilever [102] and/or x-ray diffraction (XRD) techniques [103]. For a given metal or alloy and an adsorbate that can partially expresses the MC effect (either through varying concentration or chain length), stress measurement may also permit the determination of a lower threshold value for which the ductile-to-brittle transition occurs.

APPENDIX A. DIGITAL IMAGE CORRELATION (DIC)

Digital image correlation (DIC) – also known as particle image velocimetry (PIV) – is a nonintrusive flow analysis and visualization technique often employed in fluid mechanics to map displacement and velocity fields of fluid flow. In this study, DIC is used to characterize the deformation field associated with chip formation in the plane strain cutting of metals and alloys. In general, the first step in using DIC is the introduction of tracer particles, e.g., dye particles, oil particles, etc., into the flow in a process known as seeding. A light source is used to illuminate groups of tracer particles within a given interrogation area. The particles are tracked via digital high-speed imaging of the flow to obtain a sequence of images of the event. Statistical methods (cross-correlation) are then used to determine local displacement vectors for the tracer particles from one image frame to the next. The local flow velocity is then calculated using the frame rate and the calibration of the imaging system [104].

Since metals are optically opaque and solid, using DIC to characterize flow in metals has its limitations. Unlike transparent fluids, only a single focal plane exists which can be imaged. Luckily, only the deformation field in plane strain cutting is of concern. Instead of introducing tracer particles into the flow, the role of tracer particles is fulfilled by asperities, or roughness features present (or deliberately introduced) on the metal surface [105–107]. The asperities scatter light significantly different from surrounding regions on the metal surface. Although asperities often lack the shape and size uniformity of real particles, the statistical nature of DIC is forgiving. The asperities closely follow the flow due to being actual surface features of the metal. The aforementioned characteristics of these asperities have been well-documented in prior work in our group. The asperities in the present study result from the roughness texture created during sample preparation through face milling and/or polishing.

The deformation parameters of strain, strain rate, and their principal directions, can be obtained from the measured velocity and displacement data. Based on small strain definition, the tensor components of strain increment during each time are obtained through differentiation of the corresponding displacement vector [108]:

$$d\varepsilon_{xx} = \partial u/\partial x, \quad d\varepsilon_{yy} = \partial v/\partial y, \quad d\gamma = 2d\varepsilon_{xy} = \partial v/\partial x + \partial u/\partial y \qquad \text{(Eq. A.1)}$$

and the strain rate components at each point as

$$\dot{\varepsilon_{xx}} = \partial\dot{u}/\partial x, \quad \dot{\varepsilon_{yy}} = \partial\dot{v}/\partial y, \quad \dot{\gamma} = 2\dot{\varepsilon}_{xy} = \partial\dot{v}/\partial x + \partial\dot{u}/\partial y \qquad \text{(Eq. A.2)}$$

where u and v are components of the displacement vector in the x and y directions, respectively. ε_{xx} and ε_{yy} are the longitudinal strains and γ is the shear strain.

The incremental strain and strain rate tensors at a point can then be written in matrix form as

$$\begin{bmatrix} \frac{\partial u}{\partial x} & \frac{1}{2}\left(\frac{\partial u}{\partial y} + \frac{\partial v}{\partial x}\right) \\ \frac{1}{2}\left(\frac{\partial u}{\partial y} + \frac{\partial v}{\partial x}\right) & \frac{\partial v}{\partial y} \end{bmatrix} \text{ and } \begin{bmatrix} \frac{\partial \dot{u}}{\partial x} & \frac{1}{2}\left(\frac{\partial \dot{u}}{\partial y} + \frac{\partial \dot{v}}{\partial x}\right) \\ \frac{1}{2}\left(\frac{\partial \dot{u}}{\partial y} + \frac{\partial \dot{v}}{\partial x}\right) & \frac{\partial \dot{v}}{\partial y} \end{bmatrix} \qquad \text{(Eq. A.3), (Eq. A.4)}$$

from which their principal values and directions can be obtained. The direction of maximum shear strain rate, also the direction of maximum shear stress, is useful for constructing slip line field models of deformation. This direction is oriented at 45° to the principal strain rate directions.

To estimate the total plastic strain imposed along a deformation path, the strain increments must be 'summed up' in a suitable manner. In general, the accumulated strain tensor components at a point cannot be obtained by 'summation' as the principal direction of the incremental tensor components will vary with location along the deformation path. However, in plastic deformation, the strain increment components are related to the effective incremental strain, assuming a von Mises yield criterion for the metal, as [109]:

$$d\bar{\varepsilon} = \sqrt{\frac{4}{9}\left(\frac{1}{2}\left[\left(d\varepsilon_{xx} - d\varepsilon_{yy}\right)^2 + {d\varepsilon_{xx}}^2 + {d\varepsilon_{yy}}^2\right] + \frac{3}{4}d\gamma^2\right)} \qquad \text{(Eq. A.5)}$$

and effective strain rate as

$$\dot{\bar{\varepsilon}} = \sqrt{\frac{4}{9}\left(\frac{1}{2}\left[\left(\dot{\varepsilon}_{xx} - \dot{\varepsilon}_{yy}\right)^2 + {\dot{\varepsilon}_{xx}}^2 + {\dot{\varepsilon}_{yy}}^2\right] + \frac{3}{4}\dot{\gamma}^2\right)}. \qquad \text{(Eq. A.6)}$$

The effective strain and strain rate, both incremental and total, are scalar quantities which can be summed or integrated in the usual way without reference to any tensor analysis. The effective strain and strain rate, along with their past states, also determine the key mechanical properties (e.g., strength, hardness, workability) of the metal after the deformation.

The total effective strain value at a point can thus be estimated by summation of the individual effective strain increments along the deformation path up and until the point, or by integration of the effective strain rate along this path. The combination of effective strain and strain rate are commonly used to determine the level of plastic deformation that a material undergoes in deformation processing and help access the evolution of microstructure during the deformation. This approach is used in the present study to analyze deformation and deformation histories. Furthermore, they are used to construct various flow lines (e.g., streaklines, streamlines) to depict the flow phenomena. There are four basic line patterns used in flow visualization: streamlines, streaklines, pathlines, and timelines. Streamlines and timelines are instantaneous lines, providing only a snapshot of the flow in time. A streamline is a line everywhere tangential to the instantaneous local velocity, showing direction in which a fluid element will travel. A timeline is a collection of neighboring fluid particles (marked at a previous instant in time) that create a line displaced in time as the particles move. Streaklines and pathlines are formed by the passage of time, providing a time-history of the flow. A streakline is a line formed by the loci of all fluid particles that have passed continuously through a fixed point. At some instant in time, the particles are marked and connected with a line. To make streaklines in an actual fluid, smoke or dye is introduced at a given point. Lastly, a pathline is a line traced out by a single fluid particle as it moves. Streamlines, streaklines, and pathlines all coincide when the flow is steady. Streamlines are mathematically easy to generate, while streaklines and pathlines are experimentally more convenient [31].

APPENDIX B. PROPERTIES OF PERMANENT MARKER INK AND INK APPLICATION TO THE SURFACE

It is worthwhile to briefly discuss some of the properties of Sharpie permanent marker ink and its interaction with surfaces. Permanent marker offers several attractive properties as an SA medium. First, the marker is considered relatively benign to the health of the user. In fact, the markers are now exempt from the requirement of a Safety Data Sheet (SDS) per the updated U. S. Occupational Safety and Health Administration (OSHA) Globally Harmonized System of Classification and Labeling of Chemicals (GHS) Hazard Communication Standard which took effect in June 2015 [110]. They also bear The Art and Creative Materials Institute, Inc. (ACMI) Approved Product (AP) Non-Toxic Seal, having been "certified in a toxicological evaluation by a medical expert as containing no materials in sufficient quantity to be toxic or injurious to humans, including children, or to cause acute or chronic health problems" [93,111]. Prior published Material Safety Data Sheets (MSDS) state the markers consist of butanol (71-36-3), propanol (71-23-8), diacetone alcohol (123-42-2), ethanol (64-17-5), pigments, dyes, and additives [93].

In addition to being benign, the low viscosity of the ink gives rise to two other desirable qualities – gap filling and planarization – both representative of the wetting ability of the ink [95]. Gap filling can be attributed to capillary action [94], while planarization results from the behavior of the ink under a gravitational field. Gap filling and planarization help ensure adequate coating of the surface of the workpiece, whose roughness is largely based on the surface preparation operation used. Coating of low and moderate-aspect ratio structures on the workpiece surface with few pores is virtually certain [95].

To gain a greater understanding of the coating thickness that a Sharpie permanent marker provides, a plate of glass was marked (coated) regularly with lines of ink for a total of four lines (**Fig. B.1**)**.** The number of writing strokes was increased with each line, resulting in lines with 1-stroke, 2-strokes, 3-strokes, and 4-strokes of ink. **Fig. B.1** is a profilometry-generated image of the ink lines, along with a profile from a 2D slice across the width of the lines. Average thickness for the ink coatings was approximately 0.1, 0.2, 0.4, and 0.7 μm for the 1-stroke, 2-stroke, 3-stroke, and 4-stroke lines, respectively. Recalling that the spatial resolution of the high-speed imaging system is 1.4 μm per pixel, the ink layer is indiscernible during imaging.

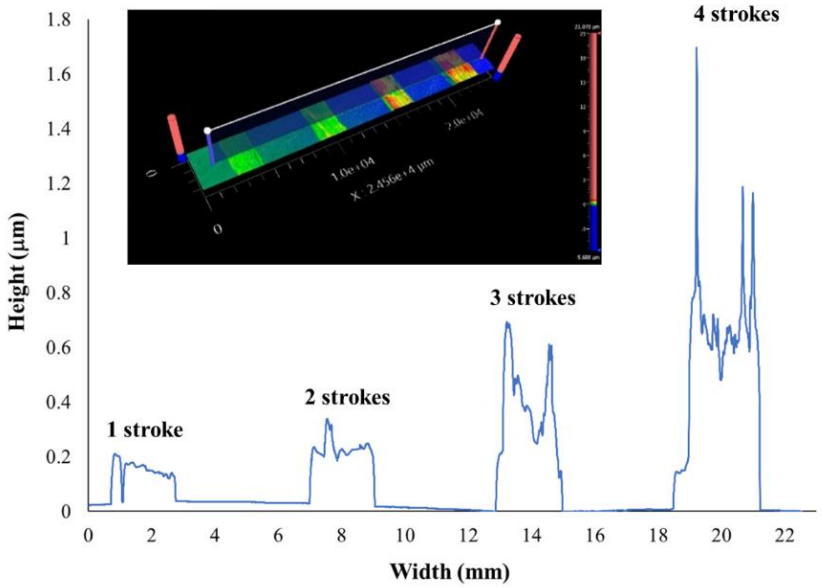

Figure B.1. Optical profilometer image of glass micro-slide surface coated using a Sharpie permanent marker. From left-to-right, the first ink line was created with one writing stroke; thereafter, the number of writing strokes was incrementally increased by one. This imaging was used to measure the ink film thickness. In the cutting experiments, two strokes of the marker pen were used to ink the Ta surface, resulting in a film thickness of ~ 200 nm.

It should be noted that the surface roughness on the workpiece (*Sa* ~ 2 μm) was considerably greater than that of the applied ink layer (~ 200 nm). As an example, **Fig. B.2** is a profilometry-generated image of a Ta surface with arithmetical mean height *Sa* of 0.93 μm and root mean square height *Sq* of 1.17 μm; this surface had four lines of ink applied, each with varying number of strokes. The first line (1-stroke) is not visible at all. The locations of the other three lines are discernible, but not entirely visible. Even for this workpiece surface roughness, approximately half the *Sa* in the experiments, much of the ink is concealed. Based on these considerations, 2-stroke lines (~ 200 nm thick ink films) were used in the experiments to ensure adequate coverage.

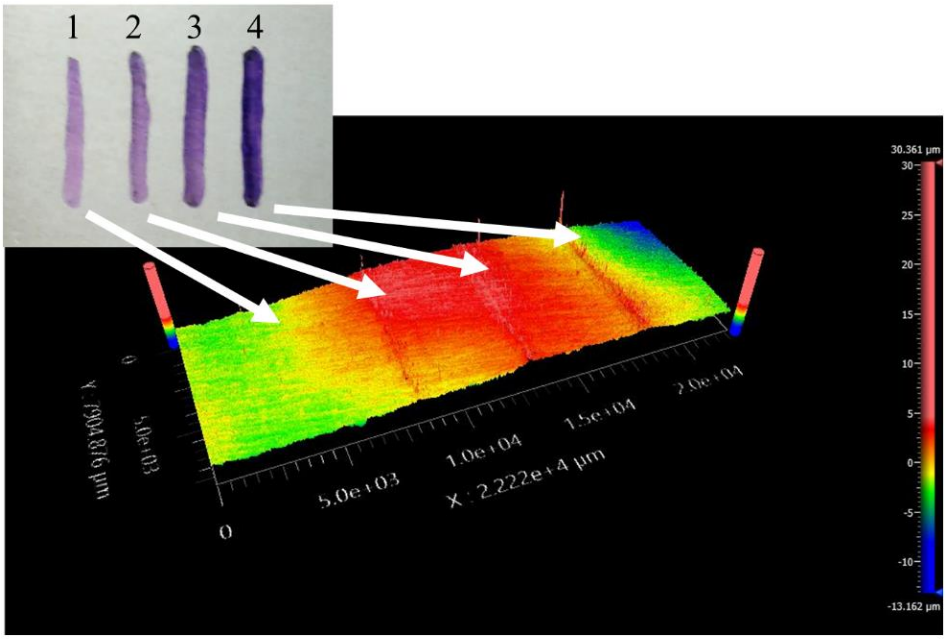

Figure B.2. 3D optical profilometer image of Ta workpiece surface (arithmetic mean height *Sa* of 0.93 µm) to which four lines of Sharpie permanent marker ink have been applied. Number of writing strokes (single stroke, extreme left) is increased incrementally stepwise from left-to-right. The ink film adheres tightly to the surface topography and hence its presence is largely obscured by the background surface roughness.

APPENDIX C. FTIR SPECTRA OF NATURAL EXTRACTS

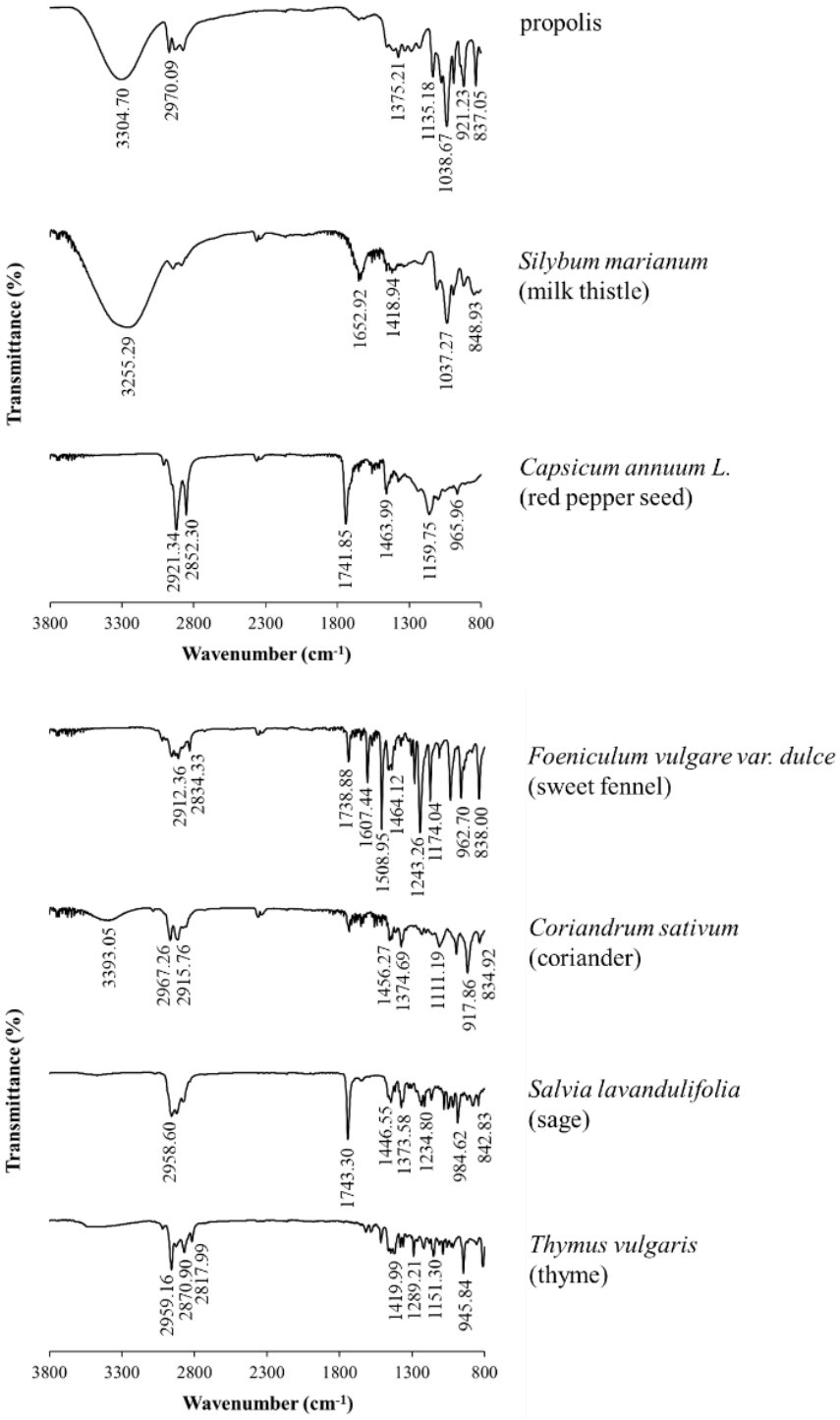

APPENDIX D. NATURAL EXTRACT FORCE TRACES FOR SS304

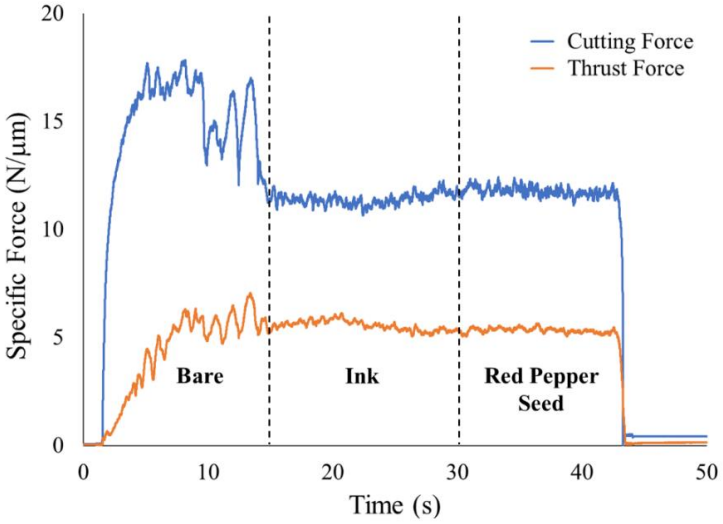

Figure D.1. Specific force traces for red pepper seed showing characteristic force reductions associated with the MC effect. One-third of the workpiece was left bare (uncoated), one-third coated with ink (a known SA media that engenders the MC effect) for comparison, and one-third coated with the natural extract. $\alpha = 20°$, $V_0 = 2$ mm/s, $h_0 = 100$ μm.

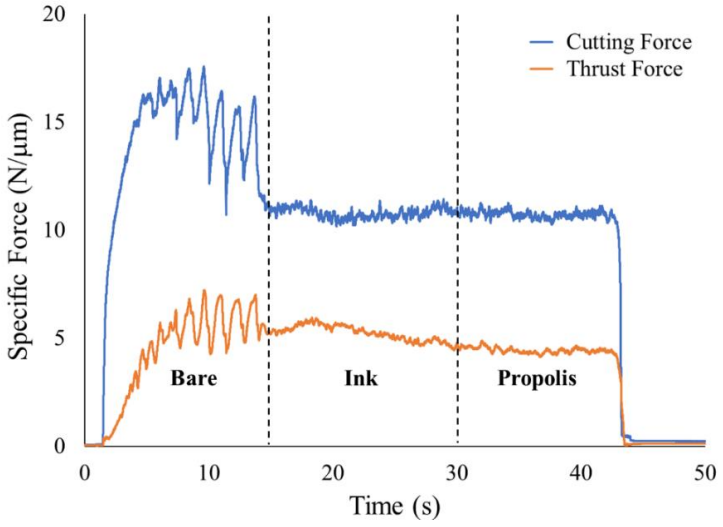

Figure D.2. Specific force traces for propolis showing characteristic force reductions associated with the MC effect. One-third of the workpiece was left bare (uncoated), one-third coated with ink (a known SA media that engenders the MC effect) for comparison, and one-third coated with the natural extract. $\alpha = 20°$, $V_0 = 2$ mm/s, $h_0 = 100$ μm.

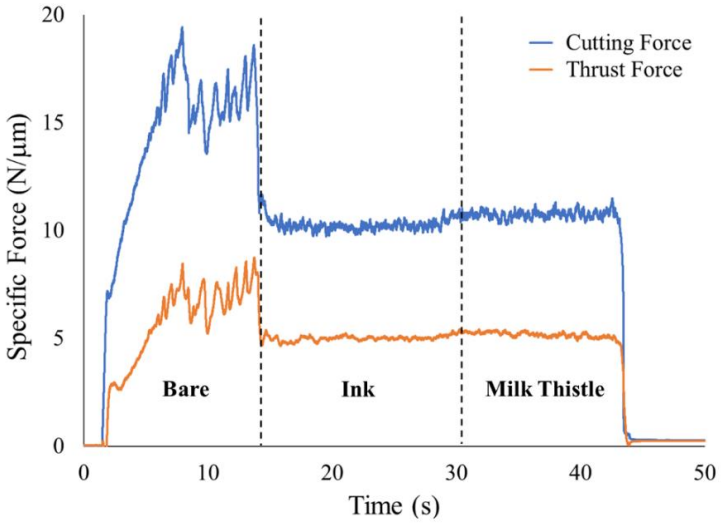

Figure D.3. Specific force traces for milk thistle showing characteristic force reductions associated with the MC effect. One-third of the workpiece was left bare (uncoated), one-third coated with ink (a known SA media that engenders the MC effect) for comparison, and one-third coated with the natural extract. $\alpha = 20°$, $V_0 = 2$ mm/s, $h_0 = 100$ μm.

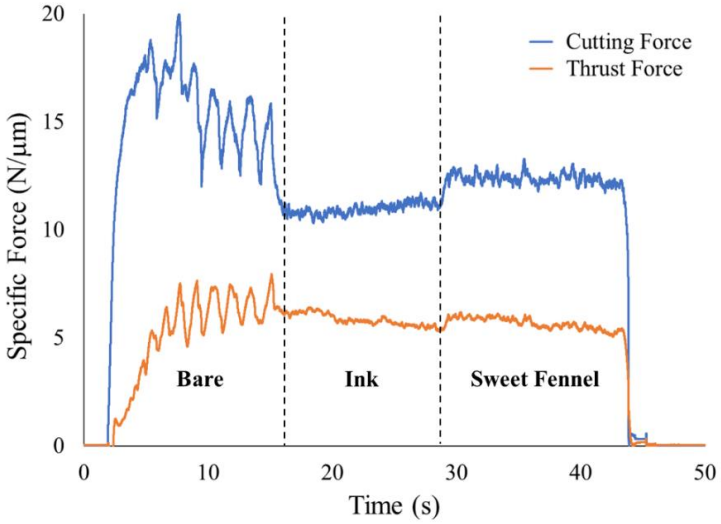

Figure D.4. Specific force traces for sweet fennel showing characteristic force reductions associated with the MC effect. One-third of the workpiece was left bare (uncoated), one-third coated with ink (a known SA media that engenders the MC effect) for comparison, and one-third coated with the natural extract. $\alpha = 20°$, $V_0 = 2$ mm/s, $h_0 = 100$ μm.

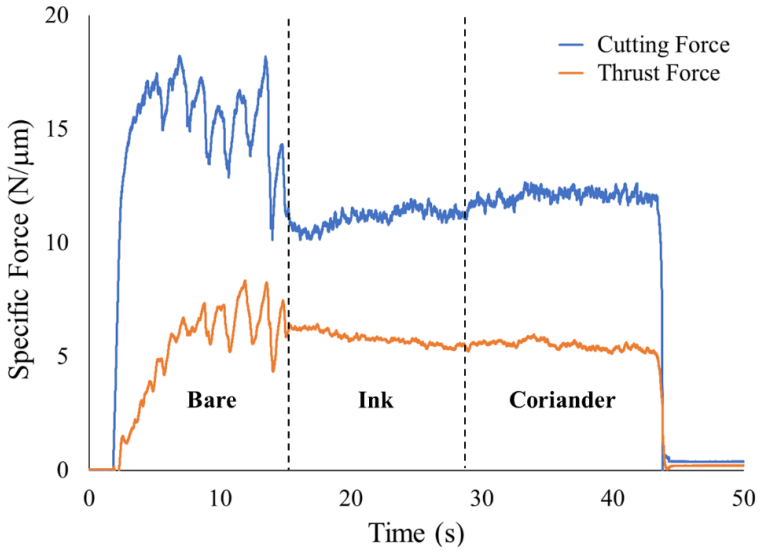

Figure D.5. Specific force traces for coriander showing characteristic force reductions associated with the MC effect. One-third of the workpiece was left bare (uncoated), one-third coated with ink (a known SA media that engenders the MC effect) for comparison, and one-third coated with the natural extract. $\alpha = 20°$, $V_0 = 2$ mm/s, $h_0 = 100$ μm.

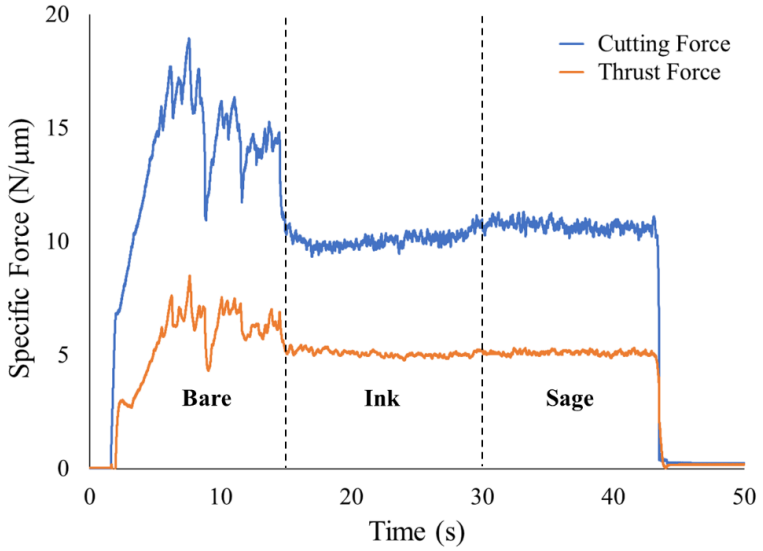

Figure D.6. Specific force traces for sage showing characteristic force reductions associated with the MC effect. One-third of the workpiece was left bare (uncoated), one-third coated with ink (a known SA media that engenders the MC effect) for comparison, and one-third coated with the natural extract. $\alpha = 20°$, $V_0 = 2$ mm/s, $h_0 = 100$ μm.

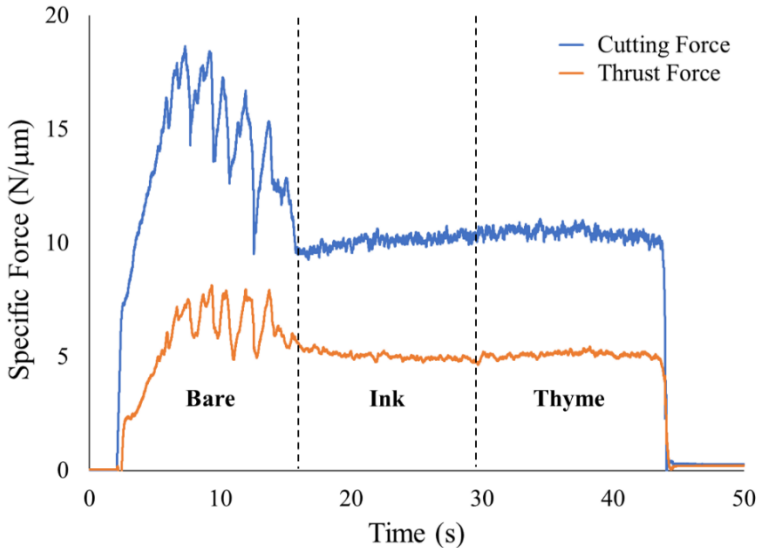

Figure D.7. Specific force traces for thyme showing characteristic force reductions associated with the MC effect. One-third of the workpiece was left bare (uncoated), one-third coated with ink (a known SA media that engenders the MC effect) for comparison, and one-third coated with the natural extract. $\alpha = 20°$, V0 = 2 mm/s, h0 = 100 μm.

REFERENCES

[1] USGS, Draft Critical Mineral List—Summary of Methodology and Background Information—U.S. Geological Survey, (2018) 1–26.

[2] K.J. Schulz, N.M. Piatak, J.F. Papp, Niobium and tantalum, Reston, VA, 2017. https://doi.org/10.3133/pp1802M.

[3] P.A. Schweitzer, Corrosion and corrosion protection handbook, Marcel Dekker, New York, NY, 1989.

[4] S.D. Cramer, B.S. Covino, Corrosion of Tantalum and Tantalum Alloys, ASM Handb. Corros. Mater. 13B (2005) 337–353. https://doi.org/10.31399/asm.hb.v13b.a0003825.

[5] R.C. Sutherlin, R.A. Graham, Corrosion of Niobium and Niobium Alloys, ASM Handb. Corros. Mater. 13B (2005) 325–336. https://doi.org/10.31399/asm.hb.v13b.a0003824.

[6] T. Kaneeda, M. Yamada, L. Anthony, Chip formation mechanism of pure Niobium plates in a superconducting accelerator cavities, Proc. 13th Int. Conf. Eur. Soc. Precis. Eng. Nanotechnology, EUSPEN 2013. 2 (2013) 129–132.

[7] P. Crook, Corrosion of Nickel and Nickel-Base Alloys, ASM Handb. Corros. Mater. 13B (2005) 228–251. https://doi.org/10.31399/asm.hb.v13b.a0003821.

[8] F. Barthelmä, H. Frank, M. Schiffler, A. Bartsch, Hard coatings to improve the machining of nickel based materials, Procedia CIRP. 46 (2016) 294–298. https://doi.org/10.1016/j.procir.2016.04.069.

[9] G. Schneider, Cutting Tool Applications, Chapter 3: Machinability of Metals, Am. Mach. (2009). https://www.americanmachinist.com/cutting-tools/chapter-3-machinability-metals.

[10] H. Yeung, K. Viswanathan, W.D. Compton, S. Chandrasekar, D.A. Weitz, Sinuous flow in metals, Proc. Natl. Acad. Sci. U. S. A. 112 (2015) 9828–9832. https://doi.org/10.1073/pnas.1509165112.

[11] K. Viswanathan, A. Udupa, H. Yeung, D. Sagapuram, J.B. Mann, M. Saei, S. Chandrasekar, On the stability of plastic flow in cutting of metals, CIRP Ann. - Manuf. Technol. 66 (2017) 69–72. https://doi.org/10.1016/j.cirp.2017.04.027.

[12] A. Udupa, K. Viswanathan, Y. Ho, S. Chandrasekar, The cutting of metals via plastic buckling, Proc. R. Soc. A Math. Phys. Eng. Sci. 473 (2017) 20160863. https://doi.org/10.1098/rspa.2016.0863.

[13] H. Yeung, K. Viswanathan, A. Udupa, A. Mahato, S. Chandrasekar, Sinuous flow in cutting of metals, Phys. Rev. Appl. 8 (2017) 1–15. https://doi.org/10.1103/PhysRevApplied.8.054044.

[14] J. Williams, E. Smart, D. Milner, Metallurgy of machining. Pt. 1. Basic considerations and the cutting of pure metals, Metallurgia. 81 (1970) 3–10.

[15] Z.Y. Wang, K.P. Rajurkar, J. Fan, G. Petrescu, Cryogenic machining of tantalum, J. Manuf. Process. 4 (2002) 122–127. https://doi.org/10.1016/S1526-6125(02)70138-2.

[16] Y.V. Deshpande, A.B. Andhare, P.M. Padole, How cryogenic techniques help in machining of nickel alloys? A review, Mach. Sci. Technol. 22 (2018) 543–584. https://doi.org/10.1080/10910344.2017.1382512.

[17] A. Udupa, K. Viswanathan, M. Saei, J.B. Mann, S. Chandrasekar, Material-independent mechanochemical effect in the deformation of highly-strain-hardening metals, Phys. Rev. Appl. 10 (2018) 1. https://doi.org/10.1103/PhysRevApplied.10.014009.

[18] A. Udupa, K. Viswanathan, J.M. Davis, M. Saei, J.B. Mann, S. Chandrasekar, A mechanochemical route to cutting highly strain-hardening metals, Tribol. Lett. 67 (2019) 1–12. https://doi.org/10.1007/s11249-018-1117-8.

[19] A.G. Ekeberg, Of the properties of the earth yttria, compared with those of glucine; of fossils, in which the first of these earths is contained; and of the discovery of a new substance of a metallic nature (tantalium), J. Nat. Philos. Chem. Arts. 3 (1802) 251–255.

[20] S. Venetsky, Tales About Metals, Mir Publishers, 1988.

[21] Homer, The Odyssey, Open Road Media, ProQuest Ebook Central, 2017. http://ebookcentral.proquest.com/lib/purdue/detail.action?docID=4828841.

[22] K. Sakai, K. Shintani, H. Kato, Study on the cutting mechanism of tantalum materials, Proc. JSPE Spring Conf. (2011) 239–240. https://doi.org/10.1016/j.jclepro.2014.10.085.

[23] K. Shintani, K. Sakai, H. Kato, Study on cutting work of tantalum materials, Proc. JSPE Autumn Conf. (2011) 201–202. https://doi.org/10.11522/pscjspe.2011A.0.201.0.

[24] K. Shintani, K. Wakabayashi, Y. Higuchi, H. Sumiya, Study on cutting of tantalum materials with nano-polycrystalline diamond tool, Proc. JSPE Autumn Conf. (2012) 199–200. https://doi.org/10.11522/pscjspe.2012A.0.199.0.

[25] W.S. de Rosset, Explosively bonded gun tube liner development (ARL-CR-0771), U. S. Army Research Laboratory, Aberdeen Proving Ground, MD, 2015.

[26] Defense Metals Information Center, Machining of superalloys and refractory metals (DMIC Memorandum 134), Battelle Memorial Institute, Columbus, OH, 1961.

[27] L.J. Lazarus, Topical report: Tantalum – 2.5% tungsten machinability testing (KCP-613-8615), Honeywell Fed. Manuf. Technol. (2009).

[28] W.R. Barton, Columbium and tantalum: A materials survey (Information Circular 8120), U. S. Dept. of Interior, Bureau of Mines, Washington, DC, 1962.

[29] A. Udupa, T. Sugihara, K. Viswanathan, S. Chandrasekar, Altering the Stability of Surface Plastic Flow via Mechanochemical Effects, Phys. Rev. Appl. 11 (2019) 1. https://doi.org/10.1103/PhysRevApplied.11.014021.

[30] R.J. Adrian, Particle Image Velocimetry, Cambridge University Press, Cambridge, 2011.

[31] F.M. White, Fluid Mechanics, 4th ed., WCB/McGraw-Hill, Boston, Mass., 1999.

[32] Mitsubishi Materials Corp., Technical Information, (2020). http://www.mitsubishicarbide.net/contents/mhg/enuk/html/product/technical_information/information/formula4.html (accessed March 31, 2020).

[33] Metal Cutting Technology Technical Guide, Sandvik Coromant, 2010.

[34] M.C. Shaw, Metal Cutting Principles, 2nd ed., Oxford University Press, New York, 2005.

[35] M.E. Merchant, Mechanics of the metal cutting process. I. Orthogonal cutting and a type 2 chip, J. Appl. Phys. 16 (1945) 267–275. https://doi.org/10.1063/1.1707586.

[36] R. Roscoe, The plastic deformation of cadmium single-crystals, London, Edinburgh Dublin Philos. Mag. J. Sci. 21 (1936) 399.

[37] A.F. Joffe, The Physics of Crystals, McGraw-Hill Book Co., Inc., New York, 1928.

[38] P.A. Rehbinder, E.D. Shchukin, Surface phenomena in solids during deformation and fracture processes, Prog. Surf. Sci. 3 (1972). https://doi.org/10.1016/0079-6816(72)90011-1.

[39] D.H. Bangham, The Gibbs adsorption equation and adsorption on solids, Trans. Faraday Soc. 33 (1937) 805–811. https://doi.org/10.1039/TF9373300805.

[40] R.M. Latanision, A.R.C. Westwood, Surface- and environment- sensitive mechanical behavior, Adv. Corros. Sci. Technol. (1970) 51–145. https://doi.org/10.1007/978-1-4615-8252-6_2.

[41] A.R.C. Westwood, R.K. Viswanadham, J.A.S. Green, Environment-sensitive mechanical behavior of oxides and oxide-coated metals, Thin Solid Films. 39 (1976) 69–78.

https://doi.org/10.1016/0040-6090(76)90624-6.

[42] F. Pusavec, A. Deshpande, S. Yang, R. M'Saoubi, J. Kopac, O.W. Dillon, I.S. Jawahir, Sustainable machining of high temperature Nickel alloy - Inconel 718: Part 2 - Chip breakability and optimization, J. Clean. Prod. 87 (2015) 941–952. https://doi.org/10.1016/j.jclepro.2014.10.085.

[43] M. Saei, A. Udupa, K. Viswanathan, T. Sugihara, R. M'Saoubi, S. Chandrasekar, Controlling segmentation in cutting of metals, CIRP Ann. 68 (2019) 41–44. https://doi.org/10.1016/j.cirp.2019.04.073.

[44] A. Chaudhari, Z.Y. Soh, H. Wang, A.S. Kumar, Rehbinder effect in ultraprecision machining of ductile materials, Int. J. Mach. Tools Manuf. 133 (2018) 47–60. https://doi.org/10.1016/j.ijmachtools.2018.05.009.

[45] G.E. Dieter, Mechanical Metallurgy, Chapter 12, 3rd ed., McGraw-Hill India, 2013.

[46] T.H. Courtney, Mechanical Behavior of Materials, Chapter 12, 2nd ed., Waveland Press, 2005.

[47] G. Wu, H. Ji, K. Hansen, T. Thundat, R. Datar, R. Cote, M.F. Hagan, A.K. Chakraborty, A. Majumdar, Origin of nanomechanical cantilever motion generated from biomolecular interactions, Proc. Natl. Acad. Sci. U. S. A. 98 (2001) 1560–1564. https://doi.org/10.1073/pnas.98.4.1560.

[48] P. Yan, Y. Rong, G. Wang, The effect of cutting fluids applied in metal cutting process, Proc. Inst. Mech. Eng. Part B J. Eng. Manuf. 230 (2016) 19–37. https://doi.org/10.1177/0954405415590993.

[49] S. Omanovic, S.G. Roscoe, Electrochemical studies of the adsorption behavior of bovine serum albumin on stainless steel, Langmuir. 15 (1999) 8315–8321. https://doi.org/10.1021/la990474f.

[50] W. Wang, F. Mohammadi, A. Alfantazi, Corrosion behaviour of niobium in phosphate buffered saline solutions with different concentrations of bovine serum albumin, Corros. Sci. 57 (2012) 11–21. https://doi.org/10.1016/j.corsci.2011.12.039.

[51] S. Fukuzaki, U. Hiromi, K. Nagata, Adsorption of protein onto stainless-steel surfaces, J. Ferment. Bioeng. 80 (1995) 6–11.

[52] S. Omanovic, S.G. Roscoe, Interfacial behavior of β-lactoglobulin at a stainless steel surface: An electrochemical impedance spectroscopy study, J. Colloid Interface Sci. 227 (2000)

452–460. https://doi.org/10.1006/jcis.2000.6913.

[53] D. Kesavan, M. Gopiraman, N. Sulochana, Green inhibitors for corrosion of metals : A review correspondence, Chem. Sci. Rev. Lett. 1 (2012) 1–8.

[54] S. Marzorati, L. Verotta, S.P. Trasatti, Green corrosion inhibitors from natural sources and biomass wastes, Molecules. 24 (2019). https://doi.org/10.3390/molecules24010048.

[55] S. Kadapparambil, K. Yadav, M. Ramachandran, N. V. Selvam, Tectona grandis leaf extract as environmental friendly corrosion inhibitor for SS304 stainless steel in hydrochloric acid, J. Sci. Ind. Res. (India). 77 (2018) 349–352.

[56] N. Soltani, N. Tavakkoli, M. Khayatkashani, M.R. Jalali, A. Mosavizade, Green approach to corrosion inhibition of 304 stainless steel in hydrochloric acid solution by the extract of Salvia officinalis leaves, Corros. Sci. 62 (2012) 122–135. https://doi.org/10.1016/j.corsci.2012.05.003.

[57] A.S. Fouda, S.M. Rashwan, H.A. Abo-Mosallam, Fennel seed extract as green corrosion inhibitor for 304 stainless steel in hydrochloric acid solutions, Desalin. Water Treat. 52 (2014) 5175–5186. https://doi.org/10.1080/19443994.2013.806223.

[58] F. Kurniawan, K.A. Madurani, Electrochemical and optical microscopy study of red pepper seed oil corrosion inhibition by self-assembled monolayers (SAM) on 304 SS, Prog. Org. Coatings. 88 (2015) 256–262. https://doi.org/10.1016/j.porgcoat.2015.07.010.

[59] A.E.A.S. Fouda, S.M. Rashwan, H.A. Abo-Mosallam, Aqueous extract of coriander seeds as green corrosion inhibitor for 304 stainless steel in hydrochloric acid solutions, J. Korean Chem. Soc. 58 (2014) 25–32. https://doi.org/10.5012/jkcs.2014.58.1.25.

[60] N. Soltani, N. Tavakkoli, M. Khayat Kashani, A. Mosavizadeh, E.E. Oguzie, M.R. Jalali, Silybum marianum extract as a natural source inhibitor for 304 stainless steel corrosion in 1.0M HCl, J. Ind. Eng. Chem. 20 (2014) 3217–3227. https://doi.org/10.1016/j.jiec.2013.12.002.

[61] A. Ehsani, M.G. Mahjani, M. Hosseini, R. Safari, R. Moshrefi, H. Mohammad Shiri, Evaluation of Thymus vulgaris plant extract as an eco-friendly corrosion inhibitor for stainless steel 304 in acidic solution by means of electrochemical impedance spectroscopy, electrochemical noise analysis and density functional theory, J. Colloid Interface Sci. 490 (2017) 444–451. https://doi.org/10.1016/j.jcis.2016.11.048.

[62] E.E. Oguzie, Influence of halide ions on the inhibitive effect of congo red dye on the

corrosion of mild steel in sulphuric acid solution, Mater. Chem. Phys. 87 (2004) 212–217. https://doi.org/10.1016/j.matchemphys.2004.06.006.

[63] E.E. Oguzie, Corrosion inhibition of mild steel in hydrochloric acid solution by methylene blue dye, Mater. Lett. 59 (2005) 1076–1079. https://doi.org/10.1016/j.matlet.2004.12.009.

[64] E.E. Oguzie, B.N. Okolue, C.E. Ogukwe, C. Unaegbu, Corrosion inhibition and adsorption behaviour of bismark brown dye on aluminium in sodium hydroxide solution, Mater. Lett. 60 (2006) 3376–3378. https://doi.org/10.1016/j.matlet.2006.03.018.

[65] E.E. Oguzie, Inhibiting effect of crystal violet dye on aluminum corrosion in acidic and alkaline media, Chem. Eng. Commun. 196 (2009) 591–601. https://doi.org/10.1080/00986440802483848.

[66] E. Oguzie, C. Akalezi, C. Enenebeaku, Inhibitive effect of methyl green dye on the corrosion of low carbon steel in acidic media, Pigment Resin Technol. 38 (2009) 359–365. https://doi.org/10.1108/03699420911000600.

[67] E.E. Oguzie, C.O. Akalezi, C.K. Enenebeaku, J.N. Aneke, Corrosion inhibition and adsorption behavior of malachite green dye on aluminum corrosion, Chem. Eng. Commun. 198 (2011) 46–60. https://doi.org/10.1080/00986445.2010.493118.

[68] R.K. Pathak, P. Mishra, Drugs as corrosion inhibitors: A review, Int. J. Sci. Res. 5 (2016) 671–677. https://doi.org/10.21275/v5i4.nov162623.

[69] S.B. Uakkaz, R. Zerdoumi, K. Oulmi, D. Mellahi, G.M. Andreadis, Electrochemical study of penicillin-G as a corrosion inhibitor for Fe-19Cr stainless steel in hydrochloric acid, Port. Electrochim. Acta. 35 (2017) 211–224. https://doi.org/10.4152/pea.201704211.

[70] B. Sanyal, Organic compounds as corrosion inhibitors in different environments - A review, Prog. Org. Coatings. 9 (1981) 165–236.

[71] B.E.A. Rani, B.B.J. Basu, Green inhibitors for corrosion protection of metals and alloys: An overview, Int. J. Corros. 2012 (2012). https://doi.org/10.1155/2012/380217.

[72] U.N. Murthy, H.B. Rekha, J.G. Bhavya, Performance of electrochemical oxidation in treating textile dye wastewater by stainless steel anode, Int. J. Environ. Sci. Dev. 2 (2011) 484–487. https://doi.org/10.7763/ijesd.2011.v2.174.

[73] N.P. de Moraes, F.N. Silva, M.L.C.P. da Silva, T.M.B. Campos, G.P. Thim, L.A. Rodrigues, Methylene blue photodegradation employing hexagonal prism-shaped niobium oxide as heterogeneous catalyst: Effect of catalyst dosage, dye concentration, and radiation source,

Mater. Chem. Phys. 214 (2018) 95–106. https://doi.org/10.1016/j.matchemphys.2018.04.063.

[74] A.G.S. Prado, L.B. Bolzon, C.P. Pedroso, A.O. Moura, L.L. Costa, Nb2O5 as efficient and recyclable photocatalyst for indigo carmine degradation, Appl. Catal. B Environ. 82 (2008) 219–224. https://doi.org/10.1016/j.apcatb.2008.01.024.

[75] J. Gandhi, R. Dangi, S. Bhardwaj, Nb2O5 used as photocatalyst for degradation of methylene blue using solar energy, Rasayan J. Chem. 1 (2008) 567–571.

[76] H.P. Felgueiras, J.C. Antunes, M.C.L. Martins, M.A. Barbosa, Peptides and Proteins as Biomaterials for Tissue Regeneration and Repair, Elsevier Inc., 2018. https://doi.org/10.1016/B978-0-08-100803-4.00001-2.

[77] M. Talha, Y. Ma, P. Kumar, Y. Lin, A. Singh, Role of protein adsorption in the bio corrosion of metallic implants – A review, Colloids Surfaces B Biointerfaces. 176 (2019) 494–506. https://doi.org/10.1016/j.colsurfb.2019.01.038.

[78] W. Wang, F. Mohammadi, A. Alfantazi, Corrosion behaviour of niobium in phosphate buffered saline solutions with different concentrations of bovine serum albumin, Corros. Sci. 57 (2012) 11–21. https://doi.org/10.1016/j.corsci.2011.12.039.

[79] J.D. Andrade, V. Hlady, A.P. Wei, Adsorption of complex proteins at interfaces, Pure Appl. Chem. 64 (1992) 1777–1781. https://doi.org/10.1351/pac199264111777.

[80] P.J. Fryer, M.T. Belmar-Beiny, Fouling of heat exchangers in the food industry: A chemical engineering perspective, Trends Food Sci. Technol. (1991) 33–37.

[81] B. Bansal, X.D. Chen, Fouling of heat exchangers by dairy fluids – A review, Proc. 6th Int. Conf. Heat Exch. Fouling Clean. - Challenges Oppor. RP2 (2005) 149–57.

[82] Dairy Processing Handbook, (2020). https://dairyprocessinghandbook.tetrapak.com/chapter/chemistry-milk (accessed March 15, 2020).

[83] D.G. Dalgleish, Denaturation and aggregation of serum proteins and caseins in heated milk, J. Agric. Food Chem. 38 (1990) 1995–1999. https://doi.org/10.1021/jf00101a001.

[84] F. Gapsari, R. Soenoko, A. Suprapto, W. Suprapto, Bee wax propolis extract as eco-friendly corrosion inhibitors for 304SS in sulfuric acid, Int. J. Corros. 2015 (2015) 1–10. https://doi.org/10.1155/2015/567202.

[85] A. Fouda, S. Rashwan, M. Abdelfatah, Corrosion inhibition of stainless steel 304 in

hydrochloric acid solution using clindamycin antibiotic as eco-friendly inhibitor, Zast. Mater. 60 (2019) 3–17. https://doi.org/10.5937/zasmat1901003f.

[86] M.C. Sunny, C.P. Sharma, Changes with Oxide Layer Thickness, (2014) 89–98.

[87] C.P. Sharma, W. Paul, Protein interaction with tantalum: Changes with oxide layer and hydroxyapatite at the interface, J. Biomed. Mater. Res. 26 (1992) 1179–1184. https://doi.org/10.1002/jbm.820260908.

[88] M. Delheusy, X-ray investigation of Nb/O interfaces, (2008) 188. http://www.iaea.org/inis/collection/NCLCollectionStore/_Public/44/048/44048706.pdf.

[89] P. Cover, The Popular science monthly ., Pop. Sci. 42 (2011) 1900–1950.

[90] B. Dureu, Raw and Finished Materials: A Concise Guide to Properties and Applications, Momentum Press, 2011. https://books.google.com/books?id=SlZoCgAAQBAJ.

[91] K. Viswanathan, A. Udupa, H. Yeung, D. Sagapuram, J.B. Mann, M. Saei, S. Chandrasekar, On the stability of plastic flow in cutting of metals, CIRP Ann. - Manuf. Technol. 66 (2017) 69–72. https://doi.org/10.1016/j.cirp.2017.04.027.

[92] A. Udupa, K. Viswanathan, J.M. Davis, M. Saei, J.B. Mann, S. Chandrasekar, A Mechanochemical Route to Cutting Highly Strain-Hardening Metals, Tribol. Lett. 67 (2019) 1–12. https://doi.org/10.1007/s11249-018-1117-8.

[93] Newell Rubbermaid, Material Safety Data Sheet (MSDS #3000), (2012).

[94] J. Kim, M.W. Moon, K.R. Lee, L. Mahadevan, H.Y. Kim, Hydrodynamics of writing with ink, Phys. Rev. Lett. 107 (2011) 2–5. https://doi.org/10.1103/PhysRevLett.107.264501.

[95] Y.C. Park, B.C. Park, S. Romankov, K.J. Park, J.H. Yoo, Y.B. Lee, J.M. Yang, Use of permanent marker to deposit a protection layer against FIB damage in TEM specimen preparation, J. Microsc. 255 (2014) 180–187. https://doi.org/10.1111/jmi.12150.

[96] P. Number, S. Red, Safety data sheet Safety data sheet, 20 (2014) 2–13.

[97] H. Yeung, K. Viswanathan, A. Udupa, A. Mahato, S. Chandrasekar, Sinuous Flow in Cutting of Metals, Phys. Rev. Appl. 8 (2017) 1–15. https://doi.org/10.1103/PhysRevApplied.8.054044.

[98] J.P. Davim, Surface Integrity in Machining, Springer, London, UK, 2010. http://ebookcentral.proquest.com/lib/purdue/detail.action?docID=510613.

[99] J. Gravier, V. Vignal, S. Bissey-Breton, Influence of residual stress, surface roughness and crystallographic texture induced by machining on the corrosion behaviour of copper in salt-

fog atmosphere, Corros. Sci. 61 (2012) 162–170. https://doi.org/10.1016/j.corsci.2012.04.032.

[100] A.S. Toloei, V. Stoilov, D.O. Northwood, The effect of different surface topographies on the corrosion behaviour of nickel, WIT Trans. Eng. Sci. 77 (2013) 193–204. https://doi.org/10.2495/MC130171.

[101] K. Sasaki, G.T. Burstein, The generation of surface roughness during slurry erosion-corrosion and its effect on the pitting potential, Corros. Sci. 38 (1996) 2111–2120. https://doi.org/10.1016/S0010-938X(96)00066-2.

[102] Y. Zhao, Surface stress detection and mechanism study with microcantilever based sensor for biomolecular monolayers, Grad. Theses Diss. (2014) 13690.

[103] P. Prevey, X-ray diffraction residual stress techniques, ASM Int. ASM Handbook. Vol. 10. Mater. Charact. (1986) 380–392.

[104] M. Raffel, C.E. Willert, F. Scarano, C. Kähler, S.T. Wereley, J. Kompenhans, Particle Image Velocimetry: A Practical Guide, 3rd ed., Springer International Publishing, 2018.

[105] S. Lee, J. Hwang, M. Ravi Shankar, S. Chandrasekar, W.D. Compton, Large strain deformation field in machining, Metall. Mater. Trans. A Phys. Metall. Mater. Sci. 37 (2006) 1633–1643. https://doi.org/10.1007/s11661-006-0105-z.

[106] M.R. Shankar, B.C. Rao, S. Lee, S. Chandrasekar, A.H. King, W.D. Compton, Severe plastic deformation (SPD) of titanium at near-ambient temperature, Acta Mater. 54 (2006) 3691–3700. https://doi.org/10.1016/j.actamat.2006.03.056.

[107] T.G. Murthy, J. Madariaga, S. Chandrasekar, Direct mapping of deformation in punch indentation and correlation with slip line fields, J. Mater. Res. 24 (2009) 760–767. https://doi.org/10.1557/jmr.2009.0094.

[108] W.F. Hosford, R.M. Caddell, Metal Forming: Mechanics and Metallurgy, 3rd ed., Cambridge University Press, 2007.

[109] E.G. Thomsen, C.T. Yang, S. Kobayashi, Mechanics of Plastic Deformation in Metal Processing, MacMillan, New York, 1965.

[110] Newell Rubbermaid, Hazard Communication Compliance Declaration, (2015).

[111] ACMI: The Art and Creative Materials Institute, What do the ACMI seals mean?, (2019). https://acmiart.org/index.php/art-material-safety/safety-tips-what-you-need-to-know#3 (accessed March 31, 2020).

VITA

Jason Marion Davis was born July 1976 in Washington, IN, USA. He is a 1994 graduate and valedictorian of Loogootee Jr.-Sr. High School. After high school graduation, Jason attended Vincennes University majoring in pre-engineering. In 1996, he graduated summa cum laude with an Associate of Science degree. Having found the experience rewarding of tutoring students in the mathematics learning lab at Vincennes University, Jason attended Indiana State University to study secondary science education with concentrations in physics and mathematics. He graduated summa cum laude with a Bachelor of Science degree in 1998. Upon graduation, Jason accepted a one-year temporary teaching position and taught physics and algebra at North Miami Jr.-Sr. High School in Denver, IN. Afterwards, Jason returned to Indiana State University and earned a Master of Science degree in physics in 2001. He then attended Purdue University School of Mechanical Engineering, West Lafayette, IN and graduated with a Bachelor of Science degree in 2005. After graduation, Jason took a position as an engineer at Neoteric Hovercraft in Terre Haute, IN, serving as a draftsman and designing hovercraft components and trailers. In 2006, he pursued a new career opportunity with the United States Navy, joining the Small Arms Weapon Systems Division at Naval Surface Warfare Center (NSWC), Crane Division in Crane, IN. That same year Jason married his wife Helen from Shelburn, IN. In 2010, he completed a Master of Science in Engineering Management from Rose-Hulman Institute of Technology in Terre Haute, IN, and Jason and Helen welcomed the birth of their first son Jasper Thomas. They celebrated the birth of their second son Jack Nathaniel in 2011. In 2015, Jason completed a Master of Science in Mechanical Engineering from Purdue University, West Lafayette, IN. That same year, he received the T2/Patent Contributor of the Year Award at NSWC Crane, having obtained and licensed to industry multiple patents in small arms technology. Upon acceptance into the Mathematics, and Research for Transformation (SMART) Scholarship-for-Service Program in 2016, he began his doctoral studies in the School of Industrial Engineering at Purdue University, West Lafayette, IN. Jason continues to be an engineer in the Small Arms Weapon Systems Division at NSWC Crane with a focus on research and development of emerging technologies.